UNIVERSITÀ DI PARMA

UNIVERSITA’ DEGLI STUDI DI PARMA

DOTTORATO DI RICERCA IN

" FISICA"

CICLO XXXVII

Innovative and sustainable solar cells based on abundant elements on the earth's crust

Coordinatore:

Chiar.ma Prof.ssa Raffaella Burioni

Tutore:

Chiar.mo Prof. Roberto Fornari

Chiar.mo Prof. Alessio Bosio

Dottorando: Stefano Pasini

Anni Accademici 2021/2022 – 2023/2024

Acknowledgements

As I reach the end of this long and challenging journey, I wish to express my deepest gratitude to all those who made this achievement possible. A special thanks goes to my supervisors, Professors Alessio Bosio and Roberto Fornari, for their endless patience, valuable advice, and constant encouragement throughout these years. Their dedication to research and passion for teaching have been an infinite source of inspiration for me.

I would also like to thank my colleagues in the research group for the shared moments in the laboratory, the enlightening discussions, and the mutual support during difficult times. I extend my thanks to Stefano Marchionna for carrying out the XRD and SEM measurements at the “Ricerca Sistema Energetico” (RSE) institute, as well as to Ildikò Cora and Zsolt Fogarassy for their collaboration and hospitality during the TEM measurements conducted in Budapest, at the "Hungarian Research Network" (HUN-REN) research center.

To my family, who has always supported me, even in the most challenging moments, goes my deepest gratitude. I also thank my friends, who knew how to make me smile and distract me at the right times.

Finally, I dedicate this thesis to the memory of Nicola Romeo, whose example has always guided me since I first joined the THIFILAB laboratory for my bachelor thesis. I hope to have honored his inspiration and dedication to research.

I conclude these acknowledgments with the hope that the work I have done is just the starting point for new adventures, enriched by everything I have learned and the extraordinary people I have met along the way.

ABSTRACT

Currently, thin-film technology facilitates the production of high-efficiency solar cells at costs that are competitive with traditional Silicon technology. However, the development of these devices has largely overlooked the abundance of constituent elements found in the Earth's crust. For instance, Indium, Gallium, and Tellurium, are considered rare elements, as noted by the European Community. To address this concern, researchers are investigating new compounds made of abundant elements, aiming to create solar cells that are sustainable in the long term. The literature features studies on many innovative materials including WSe_3, $Cu_2ZnSnSe_4$, $SnSe_2$, Sb_2Se_3, and FeS_2, which are being explored as absorber layers in thin-film solar cells.

In particular, antimony selenide (Sb_2Se_3) is emerging as one of the most promising candidate materials for use as an absorber for thin-film solar cells, thanks to its non-toxic nature and the abundance of its constituent elements in the Earth's crust. Sb_2Se_3 exhibits exceptional properties, including an optimal energy gap that theoretically allows a maximum efficiency of 33%, alongside a high absorption coefficient in the visible spectrum. In recent years, significant advancements have been made, leading to a maximum photovoltaic conversion efficiency (PCE) exceeding 10%. However, this is still considerably below its theoretical limit. The limitations in PCE can be attributed to several factors, particularly the high degree of anisotropy exhibited by this material. Key challenges include the difficulty in controlling the growth of Sb_2Se_3 grains along the crystallographic direction necessary for optimal charge transport, the interaction and band-offset with different n-type partners depending on whether the cell architecture is substrate- or superstrate-based, and the challenge of achieving a back-contact that fulfills the requirements for ohmicity.

In this PhD thesis, an effort was made to the primary limiting factors affecting the ability to surpass the photovoltaic efficiency record by examining Sb_2Se_3-based solar cells configured in a superstrate arrangement.

From a crystallographic perspective, the structural characterization of Sb_2Se_3 films revealed that their crystalline quality and preferred orientation are significantly influenced by the choice of window layer, which act as substrate for the Sb_2Se_3 growth. To gain a deeper understanding of the growth mechanism, Sb_2Se_3 thin films were deposited via close-spaced

sublimation (CSS) onto five different window layers: CdS, CdS:F, CdSe, As_2S_3, and ZnCdS. Solar cells based on Sb_2Se_3, fabricated in a superstrate configuration using these various substrates, clearly demonstrate the impact of the preferential orientation of Sb_2Se_3 on photovoltaic performance.

The synthesis of antimony selenide can be accomplished using various low-cost techniques that are easily scalable for industrial applications, such as Chemical Bath Deposition, Close-Spaced Sublimation, Vapor Transport Deposition, Rapid Thermal Evaporation, Ion Vapor Deposition, and Radio-Frequency Magnetron Sputtering. This versatility is largely attributed to the absence of polymorphism and a relatively low melting point (885 K). However, once the substrate is established, the growth of Sb_2Se_3 is significantly influenced by its propensity to form defects and stoichiometric deviations. This thesis includes an in-depth study on the CSS growth of Sb_2Se_3. In particular, it has been demonstrated how the Ar counterpressure introduced into the growth chamber has a substantial impact on the material's stoichiometry and preferred growth orientation.

Another critical factor in surpassing the 10% PCE threshold is the exploration of various materials to achieve an ohmic contact with low resistivity, for use as a back contact. This thesis proposes an innovative compound based on Fe, S, and O elements. Given the extreme abundance of these elements in the Earth's crust and their non-toxicity nature, the synthesis technique used is also straightforward. Specifically, the Fe-S-O thin film is deposited at room temperature using radio-frequency magnetron sputtering. XRD and Raman analyses revealed that the material is composed of two phases: Fe_3O_4 in both orthorhombic and cubic forms, and FeS in the troilite phase. This material establishes an effective ohmic contact on the antimony selenide thin film, yielding a contact resistivity of $0.8\ \Omega\cdot cm^2$, as determined from the current-voltage characteristics of fully assembled Sb_2Se_3-based solar cells. After three months of monitoring the photovoltaic parameters, a negligible average variation was observed. Another important factor, related to the CBO between the n-type window material and antimony selenide, is the phenomenon known as the V_{oc} deficit. Indeed, literature reports indicate that solar cell consistently exhibit an open-circuit voltage significantly lower than the theoretical. In this thesis, a comprehensive analysis of an Sb_2Se_3 solar cell in the typical superstrate configuration was conducted. By investigating of current density-voltage characteristics as functions of temperature and wavelength, along with capacitance-voltage measurements and admittance spectroscopy, we attribute the observed low open-circuit voltage to the presence of a potential barrier within the absorber material particularly near the junction interface.

In conclusion, this thesis presents a comprehensive investigation into the realization and performance optimization of Sb_2Se_3-based solar cells. Emphasizing low-cost and scalable techniques such as Close-Spaced Sublimation and sputtering, we explore the influence of growth conditions, including argon counterpressure, on material stoichiometry and preferred crystallographic orientation. The development of an innovative Fe-S-O compound as a back contact material demonstrates significant promise, achieving an ohmic contact with low resistivity and maintaining stable photovoltaic parameters over time. Furthermore, our analysis reveals the critical role of the conduction band offset and the associated V_{oc} deficit in limiting the open-circuit voltage of Sb_2Se_3 solar cells. By elucidating the underlying mechanisms affecting device performance, this work contributes valuable insights toward enhancing the efficiency of Sb_2Se_3-based solar technologies, paving the way for future advancements in the field.

TABLE OF CONTENTS

CHAPTER 1: STATE-OF-THE-ART OF THIN-FILM PHOTOVOLTAICS 1

1.1 Architecture of solar cell and Sb_2Se_3 deposition techniques 3

1.2 Crystallographic properties and defects 11

1.3 Optical properties 13

1.4 Carrier transport properties 14

CHAPTER 2: SPUTTERING AND CSS DEPOSITION TECHNIQUES 17

2.1 Sputtering system 17

2.1.1 Direct current (D.C.) and radiofrequency (RF) sputtering 20

2.2 Close-Spaced Sublimation system (CSS) 24

CHAPTER 3: THEORY OF THE SOLAR CELL 26

3.1 Homojunctions 26

3.2 Heterojunctions 30

3.3 Solar cell equivalent circuit 33

3.4 Photoelectric and photovoltaic efficiency 37

3.4.1 Photoelectric efficiency 37

3.4.2 Photovoltaic efficiency 39

CHAPTER 4: FABRICATION OF Sb_2Se_3-BASED SOLAR CELLS 42

4.1 Substrate 44

4.2 Transparent conductive oxides (TCO) 45

4.3 Window layers 49

4.4 Antimony selenide 52

4.4.1 Deep levels in antimony selenide 59

4.5 Back-contact 64

4.5.1 Composition and morphology of Fe-S-O layer 65

4.5.2 Electrical measurements 68

CHAPTER 5: IMPACT OF WINDOW LAYER ON STRUCTURAL PERFECTION AND PHYSICAL PROPERTIES OF DEVICES 74

5.1 Antimony selenide electrical properties 77

CHAPTER 6: INTERPRETATION OF THE V_{oc} DEFICIT 86

6.1 The kink effect in the JV curve 91

6.2 Crossover effect in the JV curve 95

CHAPTER 7: FUTURE PERSPECTIVE AND PRELIMINARY RESULTS **100**

CHAPTER 8: CONCLUSIONS **104**

CHAPTER 1

STATE-OF-THE-ART OF THIN-FILM PHOTOVOLTAICS

An increase on renewable energy, in particular on photovoltaic, is needed due to a strong growth in the demand of electricity, scarcity of fossil fuels, increase in their price and increase in CO_2 emissions. Currently, 63.3% of the global energy demand is met by fossil fuels, 26.3% is obtained from renewables and 10.4% from nuclear energy. Among renewables, the most important is hydropower (15.8%), while the solar stops at 2.7% [1]. Theoretical calculations show that 1 kWh of energy produced via photovoltaics would reduce CO_2 emissions into the atmosphere by 1 ton/year compared to the same amount of energy produced from fossil sources [2]. Moreover, the total energy worldwide needed would be satisfied if only 0.1% of the earth's crust were covered by photovoltaic modules with an average efficiency of 10% [2,3]. However, this estimate remains purely theoretical, due to the difficulty of efficiently distributing the energy produced by the electrical grid.

After the discovery of the photovoltaic effect, by Becquerel in 1839, there were strong development on the phenomenon comprehension, up to the physical model developed by Shockley and Queisser, showing the maximum theoretical conversion efficiency that a solar cell can achieve [4]. After that the photovoltaic (PV) technology developed strongly and, today, there are two main generations of inorganic solar cells based on single junction:

- First generation
- Second generation

The first-generation concerns PV modules based on single-junction silicon technology, both monocrystalline (m-Si) and polycrystalline (p-Si). These modules are the leaders of the photovoltaic market, achieving power conversion efficiency (PCE) around 26.1%, for m-Si, and 23.3% for p-Si [5]. The advantage of this type of solar cells lies in the fact that silicon is a not toxic and abundant element on the Earth’s crust. Moreover, the Si-based solar cells present a long-time stability in terms of device durability. Despite these facts, the production costs of Si-based PV device are very high due to the purification costs for the raw material and to the high degree of purity (9N), required to make a properly working device. Typically, to maintain the purity of 9N, silicon lingot are grown using Czochralski method, which is very energy-intensive and time-consuming process [6–9].

The second generation refers to thin film technology, starting from Cu_2S/CdS heterojunction and amorphous silicon [10–15]. Nowadays, the commercialized thin film PV modules based on $Cu(In, Ga)Se_2$ and CdTe technologies, achieve PCE of 23.4% and 22.1% respectively [16]. Despite this, their use has remained rather limited due to the presence of toxic materials (e.g. Cd) and low availability on the earth's crust of some elements (e.g. Te, In and Ga) [17–19].

Indeed, the European Commission reports, strongly emphasize the procurement of materials for photovoltaic purposes. Material can be deemed at risk for reasons [20,21]:

- economic-political: procurement of materials from non-EU countries or already widely used in other industrial sectors;
- scarcity in the Earth's crust;
- environmental sustainability. It concerns the toxicity of the materials and the relationship between the energy cost of extraction and purification of the raw material.

To address these challenges, a new generation of thin film materials is currently under investigation [22], including FeS_2 in pyrite phase, antimony selenide (Sb_2Se_3), antimony sulphide (Sb_2Se_3), the mixed compounds $Sb_2(S, Se)_3$ and $CuSb(S\text{ or }Se)_2$ as detailed in references [23–28].

In particular, antimony and selenium exhibit significantly higher abundance, measuring at 0.201 parts per million (ppm) and 0.130 ppm, respectively. Their annual global production stands at 110,000 tons and 3,000 tons, respectively [29].

Regarding antimony, it is 100% entirely imported from outside the European Union rendering it a material of concern due to its reliance on imports. However, the recycling rate, defined as "the percentage of global demand that can be satisfied through secondary raw materials", is around 28%, decreasing the dependence on critical materials. Thus, antimony selenide can be considered to "approach" sustainability as indicated in [21,22].

About Sb_2Se_3-based solar cells, starting from 2012, they had a rapid development in terms of device efficiency, thanks to its advantageous electro-optical properties, achieving a PCE record of 10.57% [30]. This rapid development shows the great potential of this material for photovoltaic purposes, even if the number of publications per year remains modest, albeit growing (see figure 1).

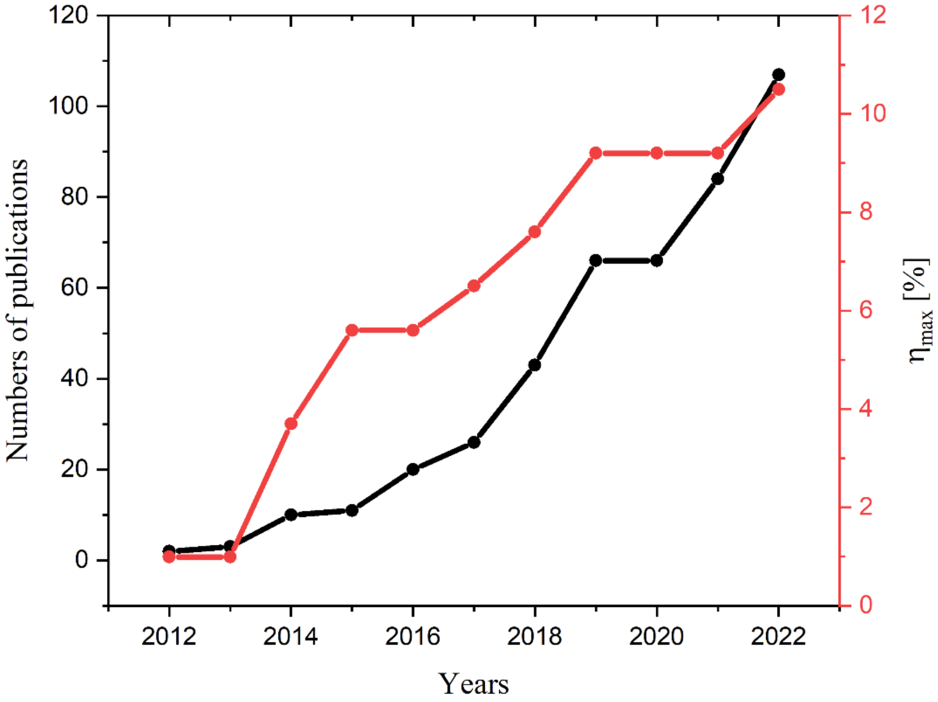

Figure 1. *Number of publications (black bot and line) and the maximum PCE achieved (red dot and line) per year [30–36]. The data related to the number of publications are taken from Clarivate search engine.*

1.1 ARCHITECTURE OF SOLAR CELL AND SB₂SE₃ DEPOSITION TECHNIQUES

The architecture of Sb_2Se_3-based solar cell can be in both substrate and superstrate configuration, as shown in figure 2.

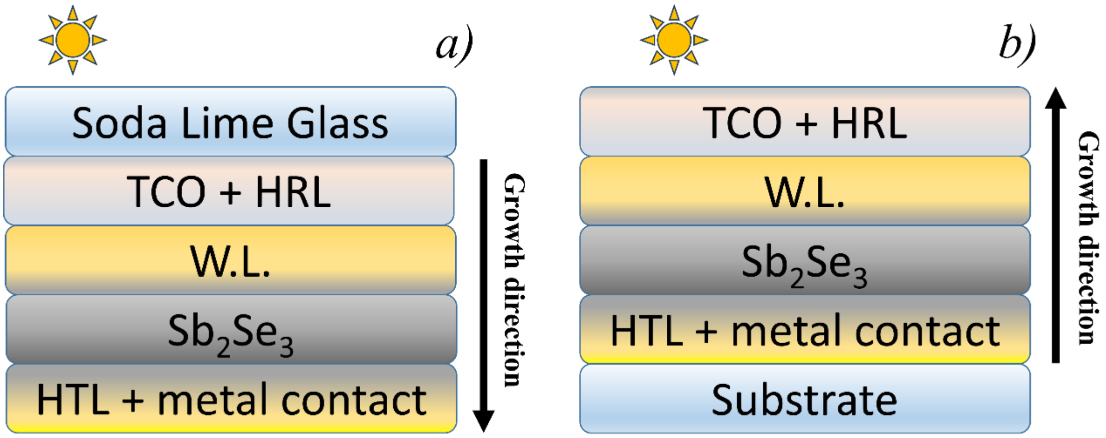

Figure 2. *Sketch of a typical device architecture for a thin film solar cell: a) superstrate and b) substrate configuration.*

In substrate configuration, the first layer to be deposited on the substrate is the back-contact, typically molybdenum (Mo). Like in CIGS-based solar cells, to make an ohmic contact, a highly conductivity p-type layer, like $Mo(S/Se)_2$, is interposed between Mo and Sb_2Se_3 [37,38]. Different ways have been studied to form $MoSe_2$, such as:

- Selenization of Mo layer [35]
- Selenization of the complete Mo/Sb_2Se_3 system [39–41].

After the deposition of the antimony selenide film, the following layer is a n-type window layer (WL) with which Sb_2Se_3 forms the p/n heterojunction. The last layer is the front contact, formed by a high resistivity layer (HRL), typically zinc oxide (ZnO), and a transparent conductive oxide (TCO), like ITO (In_2O_3:Sn), AZO (ZnO:Al) or FTO (SnO_2:F). A HRL is needed to prevent the diffusion of dopant atoms, coming from TCO, inside the p/n heterojunction and to mitigate the risk of short circuit in case of pinholes in the window layer. The substrate configuration advantage is that the substrate could be opaque, like ceramics or flexible metallic and polymeric foils since the light passes through the TCO.

A reverse scenario is observed in the superstrate configuration. In fact, in this configuration the substrate needs to be transparent to the visible portion of the solar spectrum and normally soda-lime glass is used. The first step is the deposition of TCO’s and HRL, followed by the active WL and Sb_2Se_3 layers, which form the heterojunction. The last material, deposited on top of antimony selenide, is the back contact or hole transport layer (HTL). Several HTLs, both organic and inorganic, such as Spiro-OMeTAD [42], P3HT [43], Fe-S-O [44], NiO_x [45] and WO_{3-x} [46] have been tested.

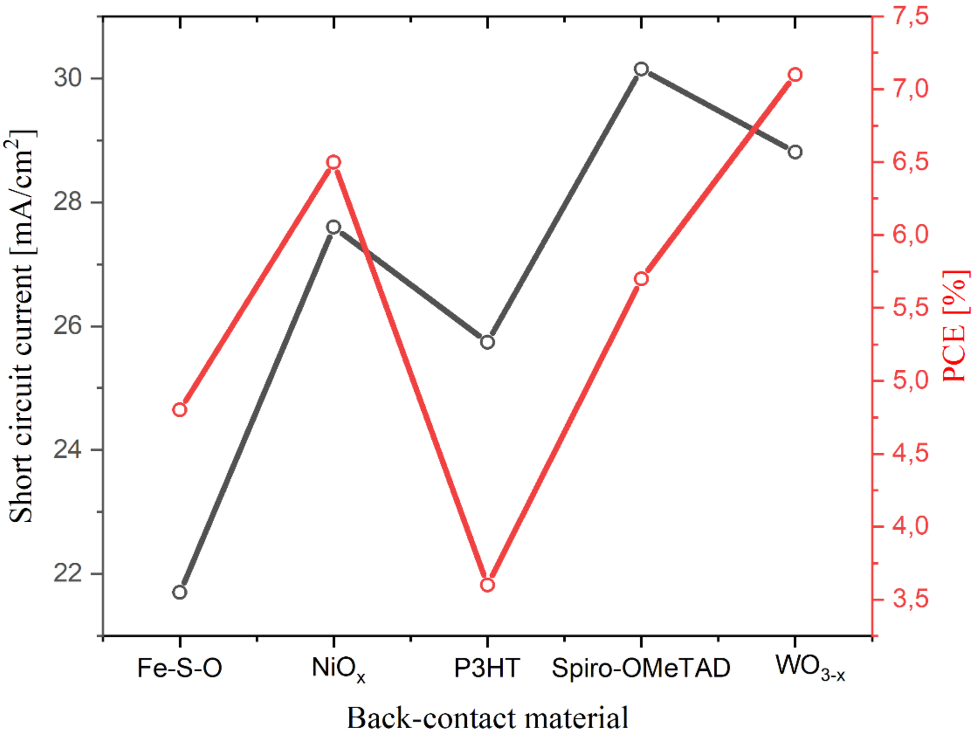

Figure 3. *Behaviour of the short circuit current (black line and dot) and PCE (red line and dot) of the* Sb_2Se_3*-based solar cell in superstrate configuration, using different HTLs.*

In Figure 3, the graph shows the trend of the photocurrent and the PCE as a function of the back-contact material under consideration. Correlating the two parameters, it is evident that for cells in superstrate configuration, the best back-contact is based on WO_{3-x}. However, the photovoltaic parameters, especially J_{sc}, mainly depend on the p/n junction and not only on the ability of a specific material to extract the photogenerated charges. For a more detailed comparison, it would be necessary to take into account the phenomenon of recombination at the junction interface and grain boundary recombination. These two phenomena vary significantly depending on the technique used to grow Sb_2Se_3 and the window layer, so this comparison remains purely qualitative.

Both in substrate and superstrate configuration, the most common WL used is cadmium sulphide (CdS) with which a record PCE of 10.57% was achieved in superstrate configuration [30]. The conduction band offset (CBO) in the CdS/Sb_2Se_3 heterojunction plays a crucial role for the proper functioning of the device. However, for CdS, this aspect remains still unclear [47–49]. Adding a specific quantity of zinc into the CdS crystal lattice, to form the $Cd_xZn_{1-x}S$ compound, it becomes feasible to finely adjust the conduction band alignment with Sb_2Se_3.This adjustment helps to minimize the interface defects as much as possible [50]. Recently, cadmium-free window layers, such as ZnO, $Zn_{1-x}Mg_xO$, SnO_2 and TiO_2, have been tested, and the final devices reach efficiencies of 5.93%, 4.45%, 4.76% and 7.62% respectively [51–54]. In particular, it is reported that the CBO between TiO_2 and Sb_2Se_3 is flat [49,55,56], which represents the best condition for a heterostructure.

The crystalline quality of Sb_2Se_3 strongly influences the photovoltaic parameters of the solar cell. The growth and crystallinity of the material is strongly influenced by the material on which it grows, and on the deposition technique used [57]. To grow high quality Sb_2Se_3, several physical and chemical deposition techniques have been tested:

- Pulsed laser deposition (PLD): Pulsed Laser Deposition (PLD) represents a technique used to deposit thin films. It involves high-energy laser pulses to evaporate or sublimate material from a target surface into a vacuum chamber [58].The vapor is then condensed onto a substrate, forming a few micrometers thick thin film. This technique offers several key advantages: first, it produces a film with the same composition of the surface of the target material. Second, PLD facilitates the deposition of numerous materials under various gas atmospheres and under wide range of gas pressures. By capitalizing on the stoichiometric deposition capability of PLD, along with the ability of conducting deposition at elevated temperatures, superstrate solar cells have been successfully developed. These solar cells, realized with the FTO/SnO_2/CdS/Sb_2Se_3/Au layer stacks, were achieved by depositing both the active layers, CdS and Sb_2Se_3 with this technique. Notably, the Sb_2Se_3 layer was deposited at 500°C, resulting in superstrate solar cells exhibiting a PCE of approximately 4.4% [59]. A closely related deposition technique is Pulsed Electron Deposition (PED), where a high-power electron beam replaces the laser beam in the PLD deposition system. PED is particularly advantageous for depositing films with stoichiometric equivalence to the target material, even at low deposition temperatures, such as 200°C. Utilizing PED, an intriguing bifacial solar cell with a PCE of about 3% was successfully fabricated [60]. Bifacial solar cells were first studied in the 1960s, and unlike traditional single-sided solar cells, they can absorb photons from both the front and back sides to utilize diffused light and light reflected from reflective surfaces such as snow or sand. Therefore, bifacial cells have the potential to increase the power density of the photovoltaic module [61].

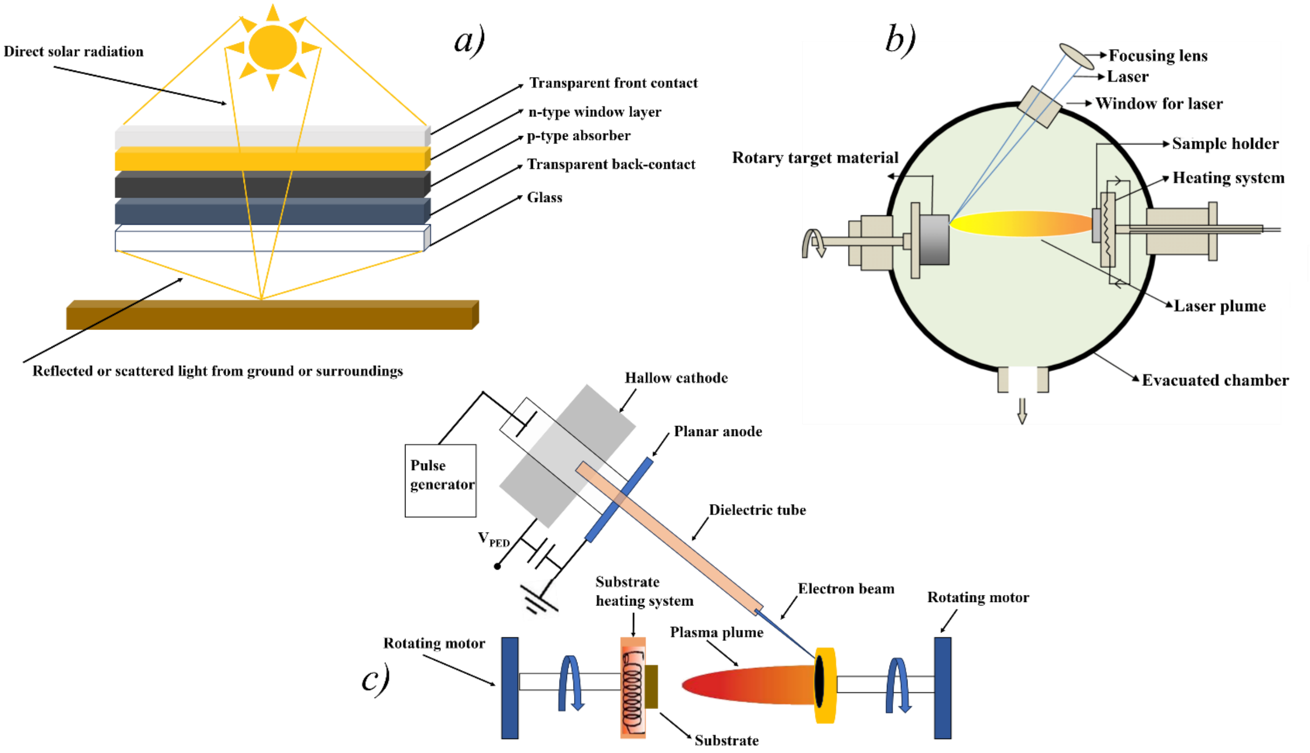

Figure 4. *a) Schematic operation of bifacial solar cells; b) PLD and c) PED working principle.*

- Electron-Beam Gun (EBG): This high-vacuum deposition technique involves a crucible kept cold by a cooling system and whose content is subjected to bombardment by an energetic electron beam, which is controlled by electromagnetic lens. By adjusting the energy and intensity of the electron beam, the deposition rate of the film can be finely regulated. Incorporating a rotating heating substrate holder in the deposition system, this technique ensures excellent thickness and stoichiometric uniformity. The deposition of Sb_2Se_3 occurs by heating the substrate to a maximum temperature (T_s) of 300°C, beyond which the material starts re-evaporating. Films deposited using this technique at temperatures below $T_s = 300°C$ exhibit Sb-rich stoichiometries, although the bombardment with energetic electrons helps maintaining the initial Sb_2Se_3 stoichiometry. Therefore, thermal treatments in a Se-controlled atmosphere are essential for EBG-deposited Sb_2Se_3 films. With this approach, Sb_2Se_3-based solar cells fabricated in a substrate configuration (SLG/Mo/Sb_2Se_3/CdS/ZnO) demonstrate a power conversion efficiency (PCE) just over 4% [62].
- Thermal evaporation (TE): By containing the evaporation or sublimation material within a crucible, directly heated through the Joule effect or indirectly with IR lamps, it becomes possible to adjust the deposition rate by controlling the heating

temperature of the container. This method, akin to EBG high-vacuum deposition, yields Sb_2Se_3 thin films with the desired morphology and crystalline structure. Given that the deposition occurs under high-vacuum conditions, the temperature of the depositing Sb_2Se_3 film must not exceed 300°C, similar to the EBG scenario. The crucible, kept at a high temperature, requires avoiding any direct chemical interaction with the material inside. For this purpose, alumina, graphite, quartz, or refractory metals such as tungsten, molybdenum, and tantalum are normally utilized as crucible materials. Employing the TE technique, solar cells have been fabricated in a substrate configuration (Ag/ITO/ZnO/CdS/Sb_2Se_3/Mo/glass), demonstrating a PCE of approximately 4.2% [63].

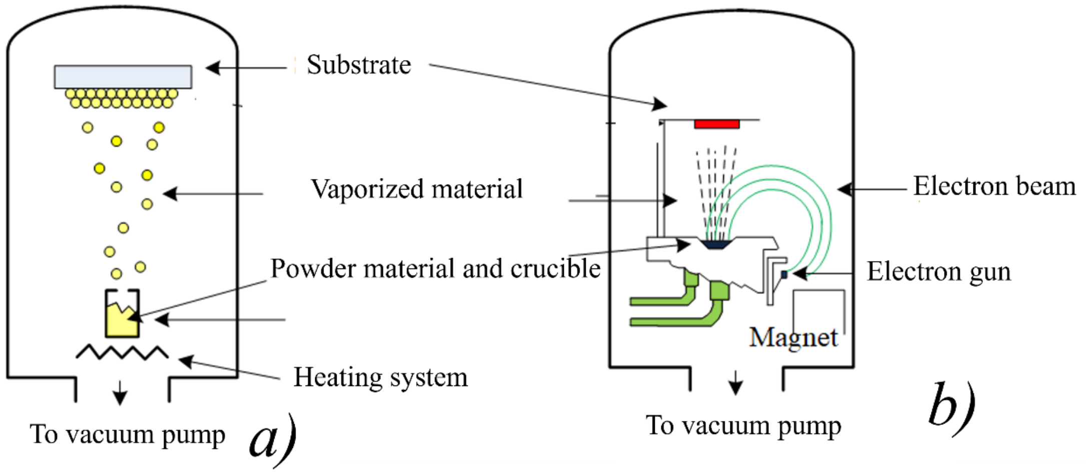

***Figure** 5. Working principle of a) thermal evaporation and b) electron beam gun.*

- Vapor transport deposition (VTD): A vapor transport process used for depositing a compound in the form of a thin film employs a saturated carrier gas carrying the compound, in the gas phase, from the source to the substrate kept at a lower temperature than that of the source. This creates a locally supersaturated condition, enabling the subsequent film growth. In contrast to the rapid thermal evaporation process (RTE), where the substrate and crucible are kept at a fixed distance and very close one to each other, the Vapor Transport Deposition (VTD) technique allows for adjustable substrate temperature and distance between the source and substrate. This flexibility enables better control of the atomic species in the vapor phase, promoting the growth of highly oriented Sb_2Se_3 films with improved crystallinity and reduced defect density [64]. Sb_2Se_3 films deposited using the VTD method have enabled the creation of a superstrate solar cell (ITO/CdS/Sb_2Se_3/Au) for the first time, demonstrating a power conversion efficiency (PCE) of 7.6% [65].

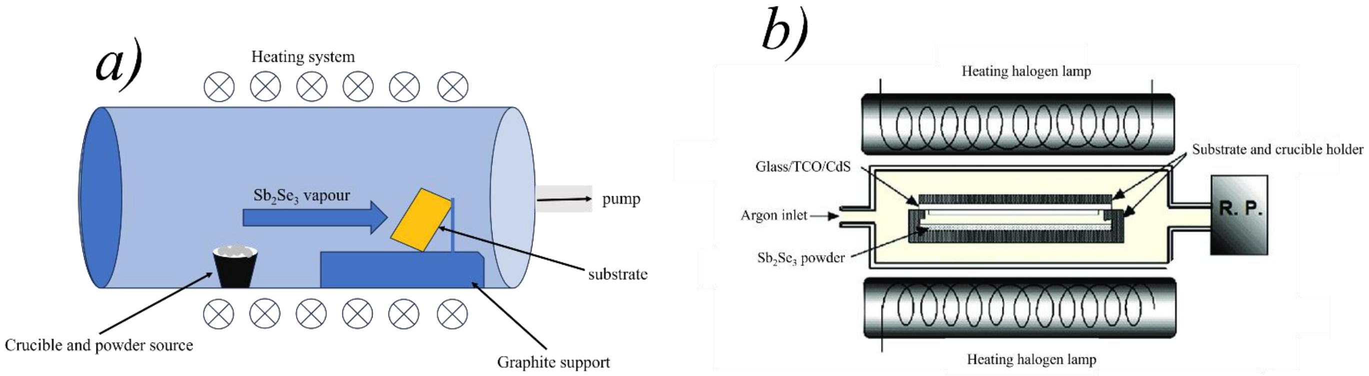

Figure 6. *Working principle of vapour transport deposition (VTD) and b) Close-Spaced sublimation (CSS).*

- Spin coating (SC): The spin-coating technique is employed to create uniform thin films with thicknesses ranging from micrometers to nanometers. The substrate is mounted on a mandrel that rotates the sample, causing centrifugal force to push the liquid solution containing the material to be deposited outward radially. The key factors ensuring flat deposition are viscous force and surface tension, which determine the substrate surface's wettability. Eventually, the thin film forms through the evaporation of solvents present in the deposition solution. Superstrate solar cells comprising FTO/CdS/Sb_2Se_3/Spiro-OMeTAD/Au, fabricated with a spin-coated Sb_2Se_3 film doped with Te, achieved a noteworthy power conversion efficiency (PCE) of around 5.5% [66]. This efficiency level is remarkable for a solution-processed solar cell.

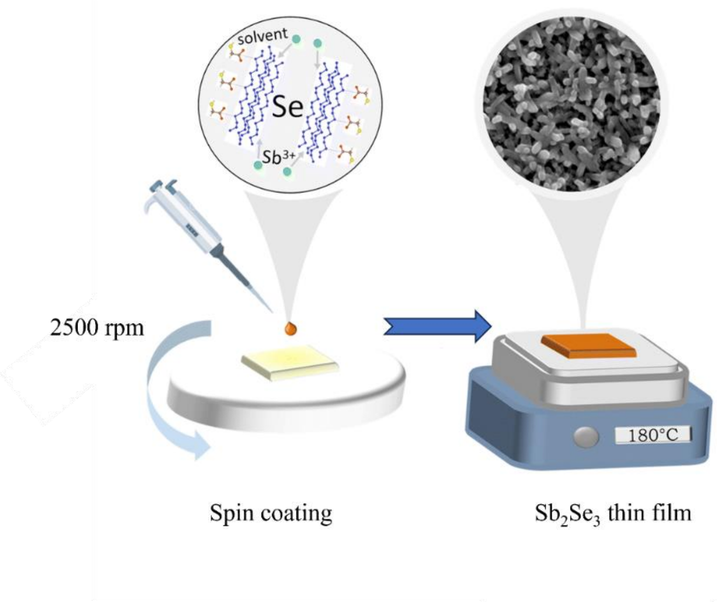

Figure 7. *Schematic representation of the spin coating working system.*

A summary of the maximum PCE for different deposition techniques is reported in table1.

Table 1. *Maximum PCE for each technique used to grow* Sb_2Se_3*. Abbreviations of deposition techniques: Close-Spaced sublimation (CSS); Radio-Frequency Magnetron sputtering (RFMSP); Pulsed laser deposition (PLD); vapor transport deposition (VTD); thermal evaporation (TE); electron beam gun (EBG); spin coating (SC).*

Deposition technique	configuration	Architecture of the solar cell	PCE [%]	Ref.
CSS	substrate	Mo/$MoSe_2$/Sb_2Se_3/i-ZnO/ZnO:Al/Ag	9.2	[35]
RFMSP	substrate	Mo/Sb_2Se_3/CdS/ITO/Ag	5.52	[67]
PLD	superstrate	FTO/SnO_2/CdS/Sb_2Se_3/Au	4.4	[59]
VTD	superstrate	ITO/CdS/Sb_2Se_3/Au	7.6	[65]
TE	substrate	Mo/Sb_2Se_3/CdS/ZnO/ITO/Ag	4.2	[63]
EBG	substrate	Mo/Sb_2Se_3/CdS/ZnO/ITO	4	[62]
SC	superstrate	FTO/CdS/Sb_2Se_3/Spiro-OMeTAD/Au	5.5	[66]

The deposition techniques associated to RFMSP and CSS will be more comprehensively discussed in a separate chapter, as they are used in this work.

1.2 CRYSTALLOGRAPHIC PROPERTIES AND DEFECTS

Antimony selenide crystallizes in orthorhombic structure related to the space group Pbnm (a = 11.62 Å; b = 11.77 Å; c = 3.962 Å) or Pnma (a = 11.7938 Å; b = 3.9858 Å; c = 11.6478 Å) [68,69]. The only difference lies in the Miller indexes permutation [70], as can be seen in figure 8.

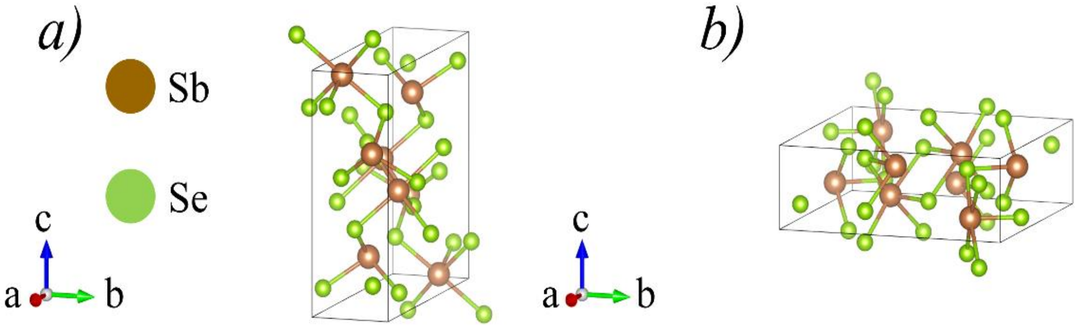

Figure 8. *Representation of Sb_2Se_3 crystal structure considering as space group a) Pnma and b) Pbnm. The images were generated with VESTA tool 3.5.8 [71].*

The peculiarity of this material lies in its structure, which is often described as a one-dimensional semiconductor. In fact, Sb_2Se_3 structure consists of repeated chains of Se-Sb-Se (ribbons) oriented along the vertical axis (c-axis). These chains are held together by van der Waals (vdW) forces between adjacent selenium atoms, along the (010) planes [68]. Instead, the units of $[Sb_4Se_6]_n$ inside the ribbon are formed by strong bonds between Sb and Se atoms (see figure 9b) [72]. The anisotropic behaviour of the bonds is reflected in the optical and electrical properties of antimony selenide films that also depend on the growth techniques used, because the preferential orientation of Sb_2Se_3 grains is very sensitive to the deposition technique [57].

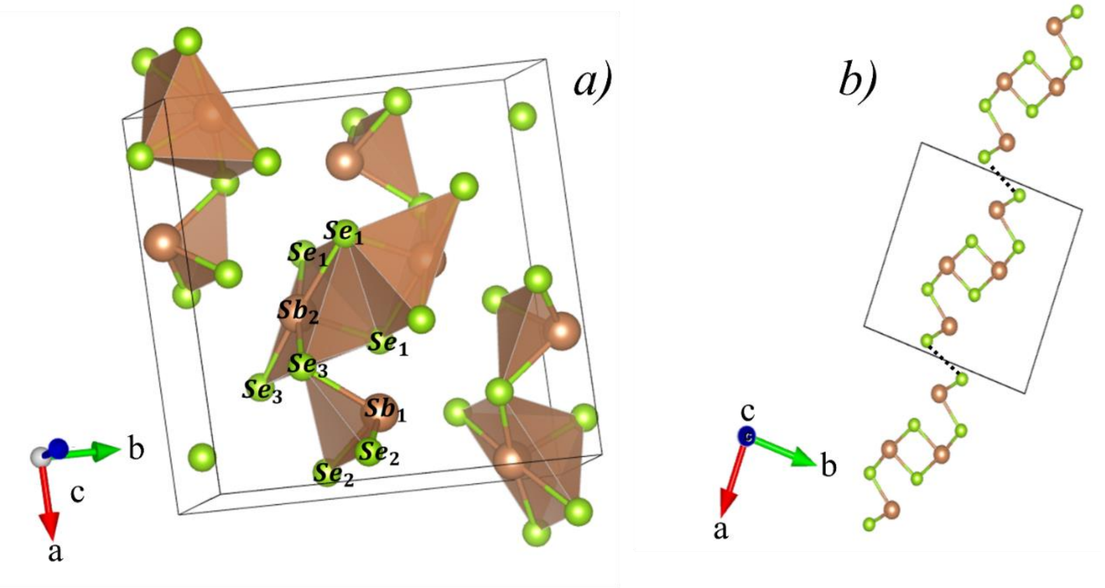

Figure 9. *a) The non-equivalent positions of the Sb (brown dots) and Se (green dots) atoms considering the Pbnm space group. b) The ribbon-like structure of Sb_2Se_3. The dotted black line represents the van der Waals bonds between Se atoms belonging to two different ribbons.*

As reported in figure 9a, there exist two distinct positions for antimony and three for selenium atoms in this configuration. $Sb_{(1)}$ atoms exhibit a six-coordination pattern, involving one $Se_{(3)}$ and two $Se_{(2)}$ atoms at shorter distances, along with one $Se_{(2)}$ and two $Se_{(1)}$ atoms at longer distances. This arrangement results in a noticeably distorted octahedron around $Sb_{(1)}$, characterized by three longer and three shorter Sb-Se distances. On the other hand, $Sb_{(2)}$ atoms adopt a seven-coordinated structure, featuring one $Se_{(1)}$ and two $Se_{(3)}$ atoms at shorter distances, two $Se_{(1)}$ atoms at a medium distance, and finally, two $Se_{(2)}$ atoms at longer distances. $Sb_{(2)}$ sits at the centre of a rectangle formed by two $Se_{(1)}$ and two $Se_{(3)}$ atoms, constituting the base of a tetragonal pyramid. The pyramid's vertex is marked by another $Se_{(1)}$ atom. Two such pyramids around $Sb_{(2)}$ are interconnected via $Se_{(2)}$ atoms, creating a double polyhedron. This double polyhedron is further linked to two octahedrons around $Sb_{(1)}$ through $Se_{(3)}$ atoms [73].

From DFT calculations, a large number of point defects in antimony selenide are observed, in particular a lot of interstitial defects, five types of antisites (Se_{Sb1}, Se_{Sb2}, Sb_{Se1}, Sb_{Se2} and Sb_{Se3}) and five types of vacancies (V_{Sb1}, V_{Sb2}, V_{Se1}, V_{Se2} and V_{Se3}).

In general, there are two limit conditions that influence the defectivity of Sb_2Se_3 that are related to the ratio Sb/Se.

Selenium vacancies (V_{Se}) are considered detrimental to the Sb_2Se_3-based solar cells, because they act as deep donor defects, reducing the number of free holes [74–78], while the antimony vacancies (V_{Sb}) role is debated because is reported that can act as deep or shallow acceptor [79,80].

The antisites formation is related to the amphoteric nature of Sb that can substitute Se into the crystal structure. The behaviour of antisites Sb_{Se} remains still unclear because they can act as acceptor or donor levels, in particular deep donor levels in Se-poor condition (Sb/Se > 0.66) [76,81].

In general, other defects that can affect the performance of a thin film solar cell are recombination centres at grain boundaries [82,83].

1.3 ***OPTICAL PROPERTIES***

The properties of antimony selenide are strongly dependent on the deposition technique used, on the crystalline quality and on the stoichiometric composition. First-principles calculations based on DFT, confirmed by experiments, shown that Sb_2Se_3 is a semiconductor with a direct and indirect energy gap of 1.17 eV and 1.03 eV respectively [77,84–88]. In general, a direct transition from the valence band (VB) to the conduction band (CB) is statistically more probable, compared to an indirect transition which must be mediated by a lattice phonon with appropriate energy. In the case of Sb_2Se_3, the small difference between the values of the direct and indirect band gap suggests a high probability of achieving a direct transition. Consequently, antimony selenide can be regarded as a direct gap semiconductor, with E_g = 1.17 eV. This statement is supported by a high absorption coefficient value in the visible region of the solar spectrum ($\alpha > 10^5$ cm^{-1}), which is characteristic of direct gap semiconductors [78]. Additionally, these properties enable the absorption of all visible light in a relative thin layer of Sb_2Se_3 (~ 800 nm).

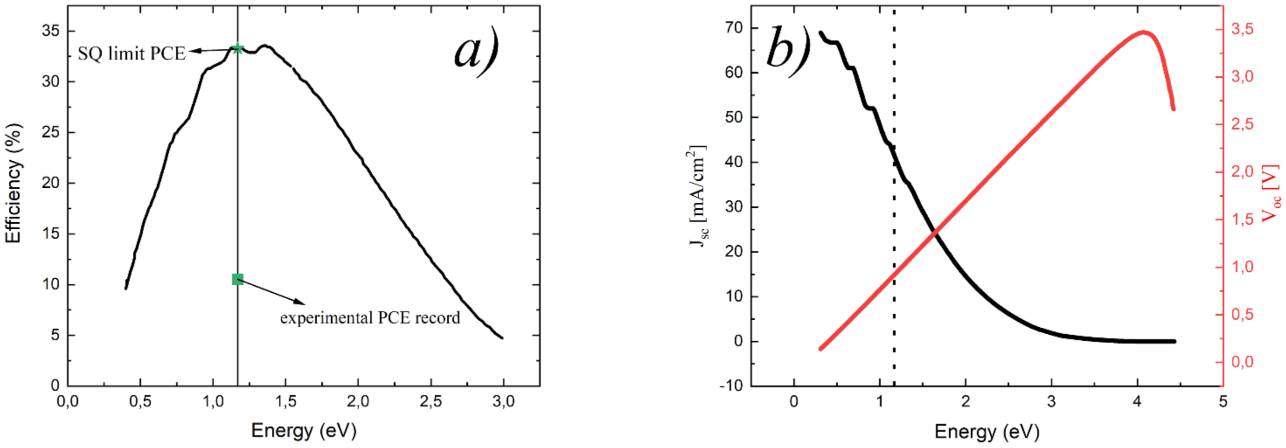

Figure 10. *Representation of Shockley-Queisser limit for Sb_2Se_3 in terms of a) energy conversion efficiency, b) short-circuit current (black line) and open-circuit voltage (red line).*

In figure 10 the maximum limits of efficiency, open-circuit voltage (V_{oc}) and short circuit current (J_{sc}) are reported as a function of the energy gap of the absorber material and the theory was developed by Shockley and Queisser [4]. The discussion sets a thermodynamic limit on the photovoltaic parameters that a single junction solar cell can reach. In particular, the antimony selenide energy gap is within the maximum of the efficiency curve (figure 10a) with a theoretical efficiency, photovoltage (V_{oc}) and photocurrent (J_{sc}) of 33.3%, 0.9 V and 41.4 mA/cm^2 respectively.

The experimental V_{oc} record obtained for Sb_2Se_3-based solar cell is 509 mV [89], far from the theoretical estimates for this material. As discussed in the previous paragraphs, this discrepancy could essentially be due to a non-correct CBO alignment between Sb_2Se_3 and the window layer material, creating a high number of interface states, that acts as recombination centres. Moreover, the V_{oc} loss is associated to Shockley-Read-Hall (SRH) recombination [90].

1.4 ***CARRIER TRANSPORT PROPERTIES***

Antimony selenide exhibits a naturally weak p-type conductivity, with a low concentration of hole density ($p \sim 2 \cdot 10^{14}\ cm^{-3}$) [49,91].

The natural p-type conductivity is attributed to V_{Sb} [92], but also native detrimental defects are presents, such as selenium vacancies and antisites.

In particular, V_{Se} acts as hole killer, affecting the free hole concentration because they are deep donor levels [41,74,75,77,78].

The nature of Sb_{Se} defects is still unclear as they exhibit properties of both acceptor or donor levels. The behavior depends on whether the Sb_2Se_3 film is selenium-rich or selenium-poor. Additionally, it is noted that Se_{Sb} does not significantly reduce the weak p-type conduction, even when it is considered a deep donor defect [57]. The electrical properties of antimony selenide reflect its anisotropic structure. In fact, it is reported that the conduction mechanism is favoured when the Sb_2Se_3 grains are grown along the [001] orientations, the same of the ribbons [93]. It has been calculated that the hole mobility (μ_h) varies as a function of the a-, b- and c directions [94]. In particular, along the [100] direction, the mobility is in the range between 0.7 $cm^2V^{-1}s^{-1}$ and 1.2 $cm^2V^{-1}s^{-1}$ [27,94,95], in accordance with the variable range hopping conduction mechanism [96], found by Chen et al [94]. On the other hand, when the holes transport happens along the same direction of the ribbon axis, the mobility increases of an order of magnitude ($\mu_h \sim 9\ cm^2V^{-1}s^{-1}$), probably because strong covalent bonds are presents (In a covalent bond, there is a strong overlap of the wave functions localized on the individual atoms, allowing charges to be effectively shared among neighbouring atoms, enabling efficient charge transport.) between the Sb and Se atoms, as reported in literature [96–98].

As a consequence, for PV applications the Sb_2Se_3 preferential growth orientation is along the planes (h, k, l ≠ 0), parallel to the ribbon axis, because the recombination processes between two adjacent ribbons decrease, as the charge transport occurs within a single ribbon and not between different ribbons. By first principles calculations, in order to understand the relaxation of the Sb_2Se_3 surface, it has been seen that the termination related to surfaces parallel to the [001] direction did not require the breaking of the Sb-Se bonds [95]. In fact, it is reported that if the grains grow along the aforementioned planes, the grain boundaries are benign, being intrinsically passivated since they are considered dandling bonds free as they exhibit the (h, k, 0) planes [33].

Instead, the mobility of electrons is estimated to be about $(10 \div 17)\ cm^2V^{-1}s^{-1}$ [34,94]. The electron mobility has been calculated on p-type antimony selenide, where electrons are the minority carriers, making it difficult to estimate their mobility while considering the material's anisotropy. Therefore, it is only possible to obtain an estimate by assuming that the grains of Sb_2Se_3 are oriented in the favourable condition for charge transport, namely parallel to the axis of the ribbons.

The anisotropy in the conduction mechanism also affects the antimony selenide resistivity. In fact, a classic planar measurement, such as the transmission line method (TLM) technique [99], fails because the current need to pass through adjacent ribbons providing an excessive overestimation ($\rho \sim 3 \cdot 10^5\ \Omega cm$). However, by exploiting the vertical configuration of the solar cell, through the current-voltage (IV) characteristic, it is possible to estimate the resistivity of the Sb_2Se_3 with electrical conduction parallel to the ribbon axis, which is $\rho \sim 2.3 \cdot 10^4\ \Omega cm$, an order of magnitude lower compared with the resistivity measured exploiting a planar technique [100]. A more detailed discussion will be presented in chapter 4, specifically in a paragraph related to the back-contact problem. To enhance the number of free holes in Sb_2Se_3 a p-type doping strategy is needed.

In general, the elements of group IV of the periodic table, such as Sn and Pb, have been considered as potential extrinsic atoms capable of providing a p-type doping in antimony selenide [81]. Experimentally, from Hall effect measurements at room temperature (RT) introducing 0.1at% of Sn into the crystalline lattice of Sb_2Se_3, under Se-rich conditions, a notable increase in hole density and a drastic reduction in resistivity was found [101]. The doping is attributed to the replacement of Sb atoms with Sn atoms (Sn_{Sb}), which forms an acceptor level located approximately 0.24 eV above the valence band maximum [76].

As regards lead doping, it has been found out that, in Se-rich conditions, it can replace antimony both in site 1 (Pb_{Sb1}) and in site 2 (Pb_{Sb2}), generating two different acceptor levels which, compared to the top of the valence band, are located at 0.19 eV and 0.15 eV respectively. Hall effect measurements show an increasing of the free carrier density, increasing the atomic percentage of Pb atoms inside Sb_2Se_3, with a maximum value about 10^{16} cm^{-3} [102].

SPUTTERING AND CSS DEPOSITION TECHNIQUES

This chapter outlines the two primary thin film deposition techniques used at Thifilab to build the Sb_2Se_3-based solar cell.

2.1 *SPUTTERING SYSTEM*

The sputtering technique exploits a bombardment of a source material, known as the target, to generate a gas of energetic particles via a purely physical process. This is why it falls under the category of physical vapor deposition (PVD) techniques. The phenomenon of sputtering occurs whenever a particle with enough energy impacts the surface of a material in order to dislodge an atom from it. Typically, noble gas ions are used for bombardment, as they readily interact with the surrounding matter, thus preventing contamination during the deposition process. If during the inelastic scattering process, the ions energy is adequate to break the bonds of the surface target atoms and simultaneously conserving the energy and momentum transferred from the ionized gas particles to the surface atoms of the target, the latter is extracted. This process is schematically shown in figure 11 [103].

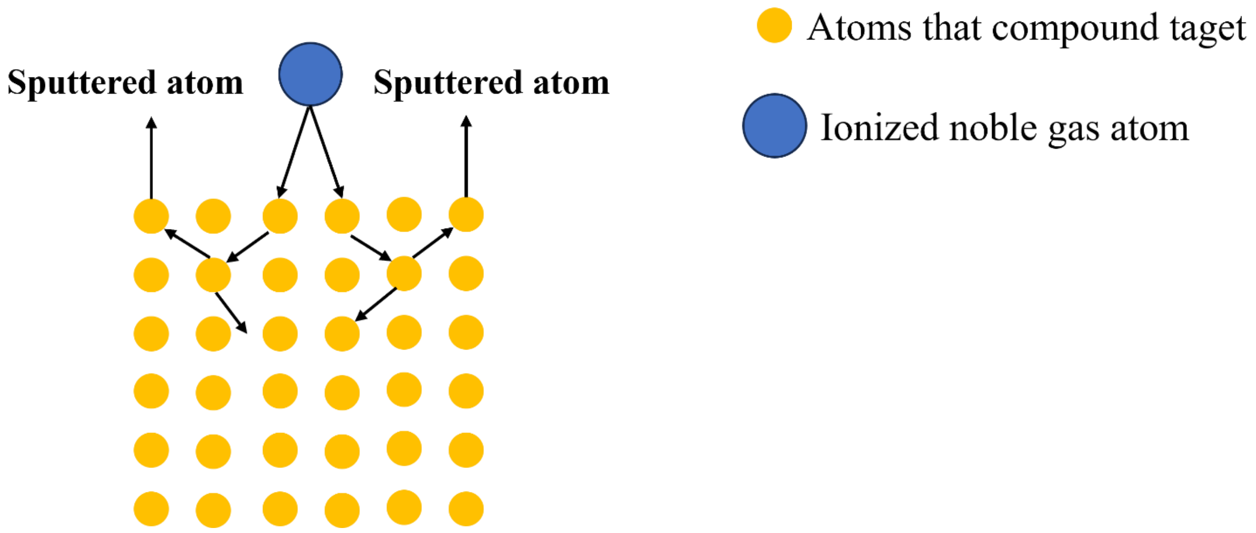

Figure 11. *Schematic illustration of the sputtering physical process.*

Within the system, a discharge (plasma) is established in a rarefied noble gas, exploiting the avalanche effect induced by ionization. The initiation of the discharge is intricately tied to the partial pressure of the working gas and the separation distance between the electrodes. This relationship is depicted by Paschen's law, illustrated in the graph shown in the figure 12. When the product of the pressure (p) and electrode separation distance (d) is low, the ionization process is not sustained. Conversely, for high values of the p·d product, elevated breakdown potential (V_B) values are required to sustain the discharge.

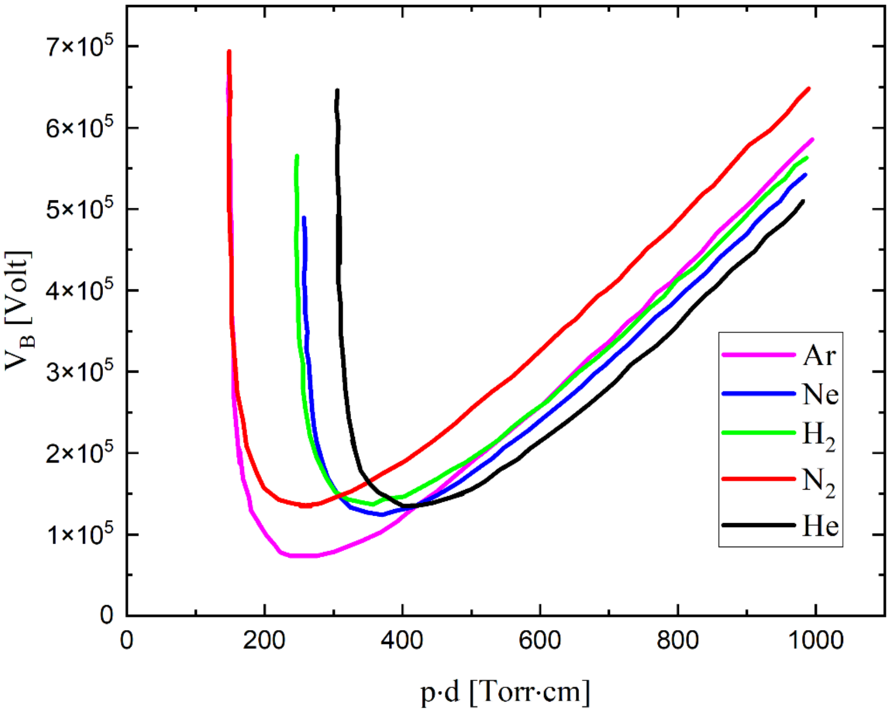

Figure 12. *Comparison of Paschen curves for the most common gases used in sputtering systems.*

However, in the intermediate zone of the p·d product, the breakdown voltage to be applied is relatively low and the minimum voltage required for the plasma ignition, is lower if gas argon is used. Furthermore, argon ions possess sufficient mass to have a high probability of conserving, energy and momentum during collision, thereby inducing the sputtering phenomenon. Consequently, argon is commonly employed as an inert gas inside the sputtering chamber. The sputtering yield (Y), defined as [104]:

$$Y = number\ of\ particles\ emitted / \ number\ of\ incident\ particles \tag{2-1}$$

varies as a function of the energy of the incident ion and four different trends can be observed, as reported in figure 13.

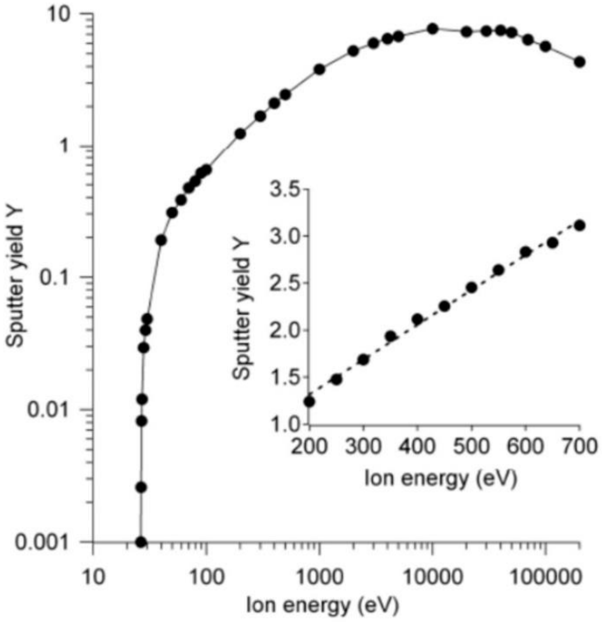

Figure 13. *Sputtering yield as function of the ion energy, in eV [104].*

In the energy range between 30 and 50 eV the yield is nearly zero, representing the threshold energy required for the sputtering phenomenon to occur. This threshold energy is equivalent to the bond energy of the atoms comprising the surface of the target within a thickness that depends on the material. Moreover, this threshold varies depending on the energy of the incident ion and the temperature of the target surface. In the intermediate range (see inset in figure 13), between 50 and 1000 eV, the energies of the incident ions are adequate to initiate the sputtering. During this process the energy is transferred to the atoms on the surface of the substrate, and if energy and momentum are simultaneously conserved during the collision, one or more atoms are removed from the target surface (see figure 11). This energy regime is characterized by peculiar properties:

- The sputtering yield increases linearly with the energy of the incident ion;
- The sputtering yield depends on the material constituting the target;
- Increasing the angle of incidence of the ion with respect to the normal results in an increased yield for many materials;
- Increasing the ionic current there is a linear increase in atoms sputtered.

By increasing the energy, we enter a regime where the sputtering yield is higher, but it becomes technologically unfeasible to work with such high energy levels. In fact, the sputtering yield does not increase linearly with the ion's energy, as not all the energy transferred to the surface of the target is utilized for the sputtering phenomenon; a portion is dissipated in the form of heat. Indeed, the target is always water-cooled to dissipate heat away from it. However, at high energies, the heat transfer is not efficient enough, resulting in target damage or evaporation of atomic species directly from the surface of the target. Finally, when the energy of the ion approaches 50 KeV the sputtering yield diminishes significantly. At this energy level, the ion has enough energy to penetrate into the material and transfer its energy away from the surface, causing damage to the surface of the target or implantation of the ion itself. Another crucial factor influencing sputtering yield is the partial pressure of gas within the chamber. Observing the trend of the sputtering yield as a function of the partial pressure of gas, as depicted in figure 14, we note that at low pressures there are insufficient atoms to sustain the discharge. Conversely, at high pressures, the probability of collisions between ions and sputtered atoms is very high. In both cases the sputtering yield is very low, which indicates the necessity to work under intermediate conditions.

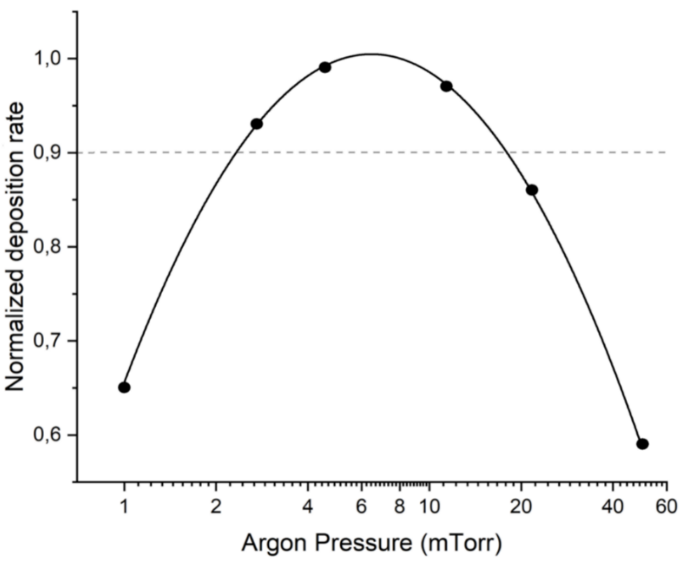

Figure 14. *Sputtering yield as function of the deposition rate. The image is adapted from [105].*

2.1.1 ***Direct current (D.C.) and radiofrequency (RF) sputtering***

In the D.C. sputtering configuration an anode and cathode are positioned within a vacuum chamber, to which a potential difference is applied. This bias causes argon ions to migrate through the discharge towards the target (cathode) triggering the sputtering phenomenon.

In addition, aside from removing atoms, electrons, known as secondary electrons, are emitted from the surface. These electrons migrate within the discharge, and have a high probability of impacting with an argon atom thereby ionizing it. Consequently, the secondary electrons play a crucial role in sustaining the discharge. A schematic representation of this process is depicted in figure 15.

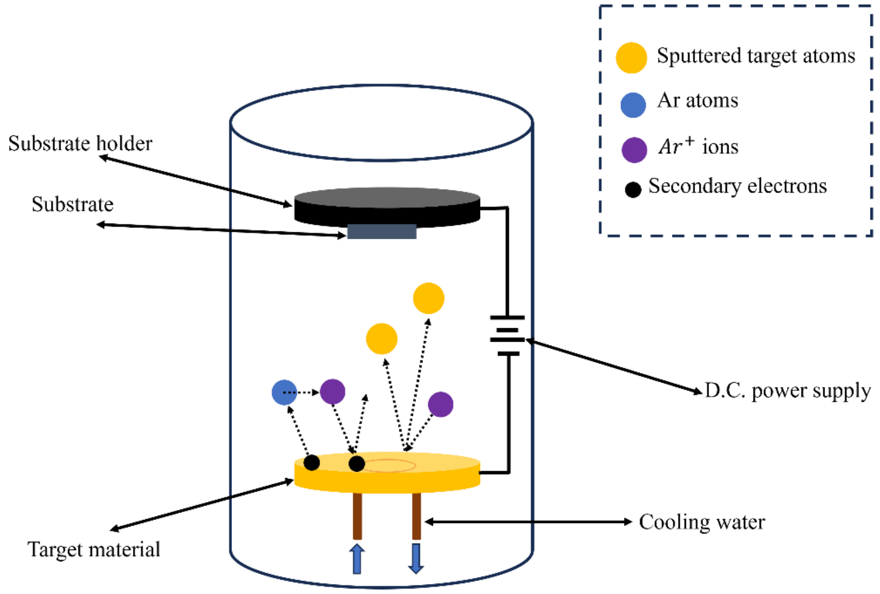

Figure 15. *Schematic representation of D.C. sputtering system. The image is adapted from [106].*

This configuration, in direct current, is suitable for depositing thin films of conductive materials. When sputtered atoms come from targets made of insulating or semiconductor materials, they are unable to exchange the charges accumulated during the bombardment. As a result, a layer of positive charges forms on the surface of the target hindering the arrival of additional argon ions. To grow thin films of insulating or semiconducting materials, it is necessary to apply a radiofrequency power. This is because, after a half-period, there is a reversal of the polarity of the two electrodes. As a result, the sputtering balance becomes zero, since what was deposited on the substrate in the first half-period is sputtered out in the following half-period. Furthermore, during the first half-cycle, there is a high electronic current at the anode, while in the second half-cycle only a small ionic current flow due to the different mobility values (figure 16a). However, by decoupling the electrodes with a suitable capacitor, no net current can pass through the capacitor by definition. Consequently, the potential spontaneously adapts to the system in such a way that there is only for a short period (about 1% of the period) polarity inversion of (figure 16b). During this short period, electrons discharge the target, but the more massive argon ions are unable to travel the reverse direction. As a result, deposition occurs on one electrode, while on the other, decoupled from the capacitor, sputtering action takes place.

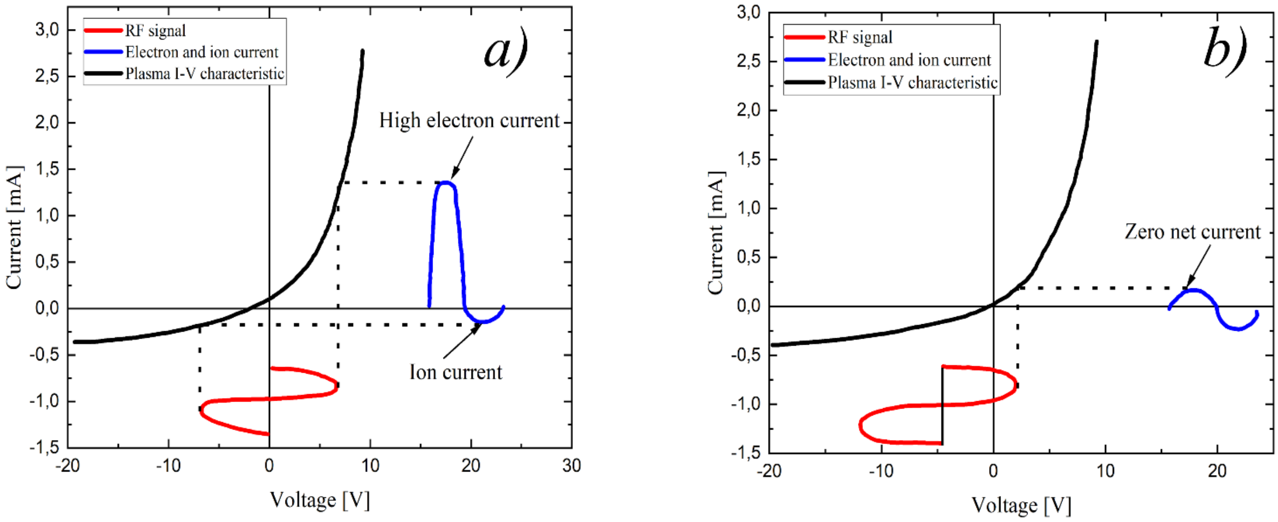

__Figure 16.__ RF supply a) without and b) with an appropriate capacitor that decouples the circuit. The images are reprinted from [105].

Traditional sputtering systems, both DC and RF, present various issues, one of which is the limited number of ionizing collisions with secondary electrons. These electrons, after colliding with an argon atom, migrate along the discharge towards the anode. To overcome this inconvenience, and therefore increase the deposition rate, it is necessary to boost the power of the power supply, thereby effectively increasing the number of secondary electrons impacting the substrate. This results in excessive heating of the substrate, and since the secondary electrons are highly energetic, counter-sputtering action may occur from the substrate due to secondary electron bombardment. Furthermore, under these conditions, the plasma is not uniform, leading to sputtering of the target even on the edges, eroding them, and exposing the deposition to pollution phenomena. This is due toa sputtering action on the target support, typically made of copper. To address these issues, permanent magnets are introduced beneath the target to ensure that magnetic field lines are as parallel to the target surface as possible. This configuration enhances the ionization efficiency of argon atoms near the magnetic field lines, as the secondary electrons will be confined around these lines executing a helical motion. Indeed, the sputtering phenomenon becomes more efficient in the areas limited by the field lines, thereby eliminating the problem of partial exposure of the edges. However, leveraging this technology, as depicted in figure 17a, does not result in uniform erosion of the target, leading to material waste. In Figure 17b, a typical industrial target with cylindrical symmetry is depicted. The cylindrical target is hollow in order to be supported by a rotating pin, which enables uniform erosion of the target, allowing the utilization of 95% of the material comprising the target. This helps to reduce waste associated with material usage.

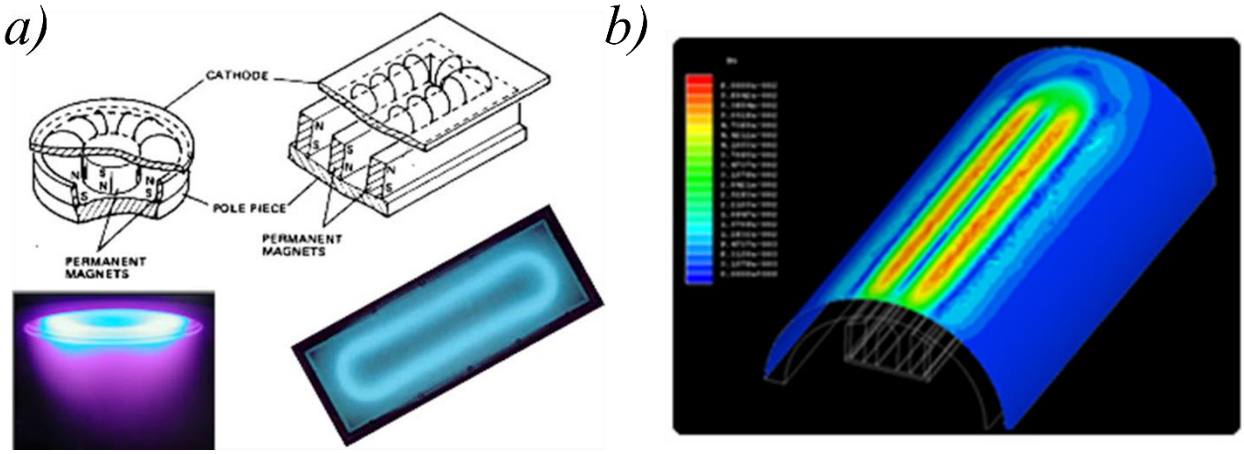

Figure 17. (a) Non-uniform erosion profile of the target. (b) Cylindrical rotating target in which all the constituent material could be sputtered.

Another configuration is reactive sputtering, which enables the growth of thin films of compounds from metal targets, by introducing a partial pressure of argon and reactive gas (typically in molecular form) into the working chamber. Inside the sputtering chamber, the presence of the plasma provides sufficient energy to break apart the molecules. If the atoms are in proximity of the cathode, they can be struck by secondary electrons, which ionize the reactive gas atoms. These ions migrate along the discharge towards the target, chemically bonding with the atoms of the target itself forming a new material ready to be sputtered.

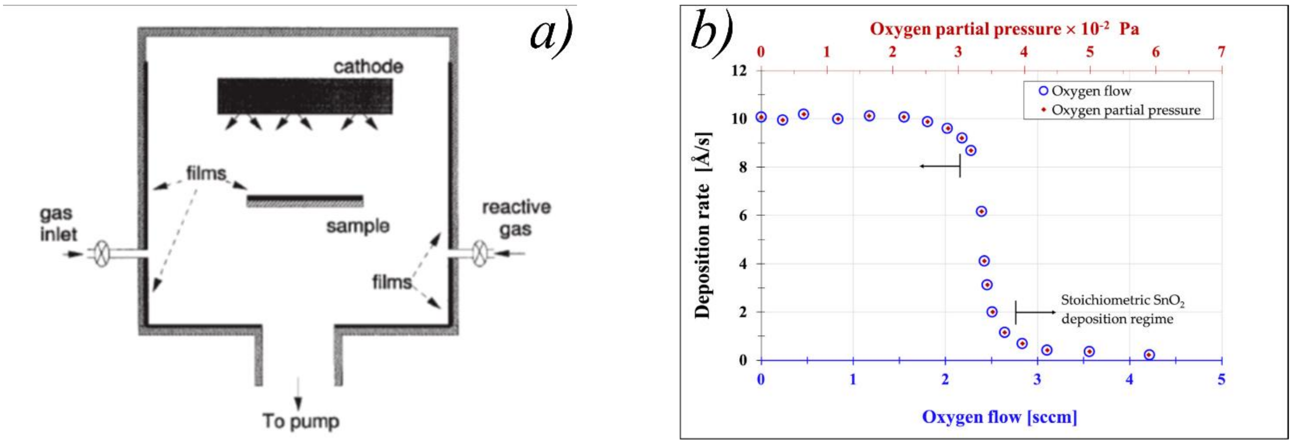

Figure 18. *a) schematic representation of the reactive sputtering system. The image is taken from [103]; b) deposition rate vs oxygen partial pressure in the case of* SnO_{2-x} *compound, starting from a pure Sn target [107].*

As shown in figure 18b, at low partial pressure values of reactive gas, the probability of ionizing a reactive gas is low, resulting in only the material constituting the target being affected. As the partial pressure increases, so does the probability of ionization. Consequently, reactive gas atoms chemically bond with the surface of the target forming a compound. This compound is subsequently sputtered by argon ions and deposited layer-by-layer onto the substrate.

2.2 CLOSE-SPACED SUBLIMATION SYSTEM (CSS)

CSS is a deposition technique that bases on the phenomenon of sublimation. The system comprises a vacuum chamber containing a crucible with a solid source composed of compact Sb_2Se_3 and the substrate, placed at a distance of approximately 5 mm from each other. Both the crucible and the substrate are heated using halogen lamps and their temperature are controlled using two thermocouples. The substrate holder and source holder are both made of graphite. A photograph of the CSS system used in this work is reported in figure 19.

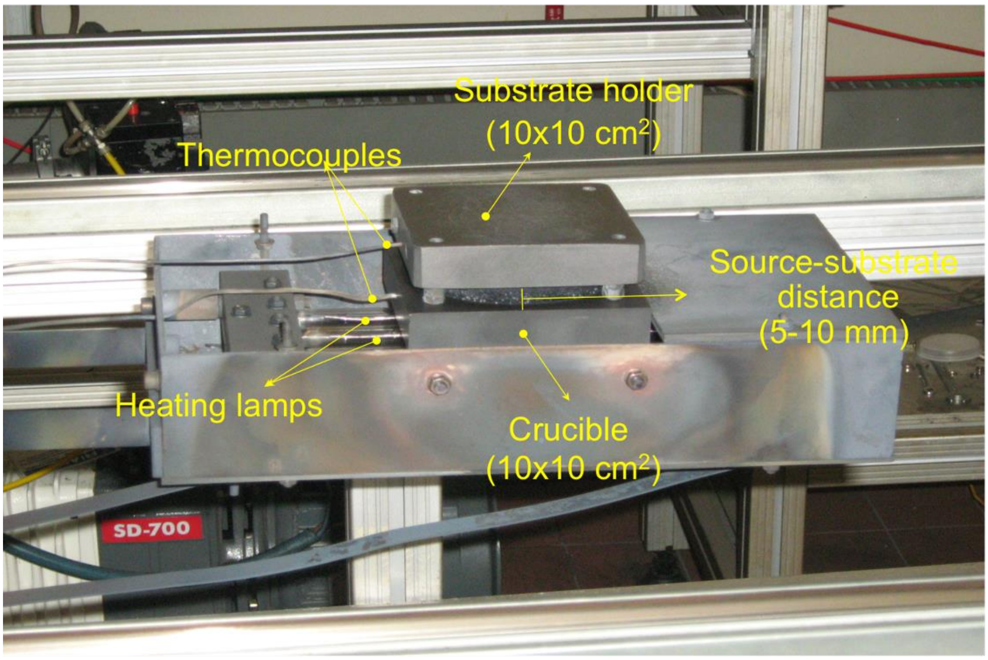

Figure 19. *Photograph of the CSS system used in the thin film laboratory of University of Parma.*

An inert gas, typically argon, is circulated within the vacuum chamber for the purpose of creating a counterpressure on the substrate during the growth, to reduce the vapor pressure of the more volatile element. This enables depositions at significantly higher temperatures than those achievable with more traditional vacuum-based techniques.

improving the uniformity of the deposited film. As atoms sublimate from the crucible, they undergo many collision events with the inert gas, before reaching the substrate. Consequently, they lose energy along the way and are adsorbed onto the substrate under conditions of minimum energy. Some of the main advantages of this technique compared to other thin film deposition method include improved crystalline quality of the thin film with an average increase of the grain size. During the deposition of Sb_2Se_3 layer on top of the CdS/ZnCdS films, beneficial intermixing between these two layers begins to occur, minimizing the lattice mismatch and consequently reducing interface defects. Thanks to the excellent uniformity of the deposition, and the high deposition rate (several μm/min) this technique is particularly suitable for industrial upscaling.

CHAPTER 3

THEORY OF THE SOLAR CELL

The photovoltaic cell is a device capable of converting incident light power into electrical energy. Its operating principle is based on the photovoltaic effect, which arises from the combination of two phenomena: the internal photoelectric effect and the diode effect.

In a semiconductor, the internal photoelectric effect occurs whenever a photon strikes a semiconductor material with energy greater than the band gap energy (E_g). E_g is defined as the range of forbidden energies between the maximum of the valence band (VB) and the minimum of the conduction band (CB). When the energy of the photon ($h\nu$) is greater than the energy gap (E_g), the photon is absorbed by the semiconductor, promoting an electron from the bound state in the VB to a free state, described by a plane wave, in the CB. This process generates an electron-hole pair (e^-/h^+) with an average lifetime τ after which the electron decays back into the valence band and recombines with the hole. This recombination process emits a photon with energy $h\nu = E_g$. However, when the e^-/h^+ pair is generated in a region where a strong electric field is present, the photo-generated charges are drifted towards the external contacts, producing a current flow.

In a diode, the intrinsic electric field is provided by constructing the p-n junction. This structure is formed by putting into intimate contact a semiconductor with an excess of electrons (called n-type doped semiconductor) and another semiconductor with an excess of holes (called p-type doped semiconductor). There are two types of p-n junctions:

- Homojunctions: when the n-type doped material is the same as the p-type doped material
- Heterojunctions: when the two materials p and n are different.

3.1 ***HOMOJUNCTIONS***

One can imagine that the p-n junction is created by bringing a p-type crystal into contact with an n-type one. In the two regions, the carrier densities are different, and a diffusion current arises, consisting of holes diffusing from the p-region to the n-region and electrons diffusing from the n-region to the p-region. The holes that transit into the n-region rapidly recombine with the electrons, which in this region represent the majority carriers. Similarly, the electrons crossing the junction recombine with the holes in the p-region. These recombinations result in a decrease of free charges carriers in a thin region on both sides of the junction surface, called depletion region. In the depletion region, there are fixed charges unbalanced by mobile charges carriers. Indeed, there are donor atoms that have donated an electron, becoming a positive fixed ion, and acceptor atoms that have acquired an electron, becoming a negative fixed ion. For this reason, the depletion region is also called the space-charge region (SCR). The fixed charges give rise to an electric field ($\vec{E}$) that opposes the diffusion current. Between the sections at the ends of the depletion region, there is a difference in the electrical potential ϕ_{BI} called built-in potential, that hinders the movement of holes toward the n-region and electrons toward the p-region. The height of the potential barrier depends on the material, the doping concentration and temperature.

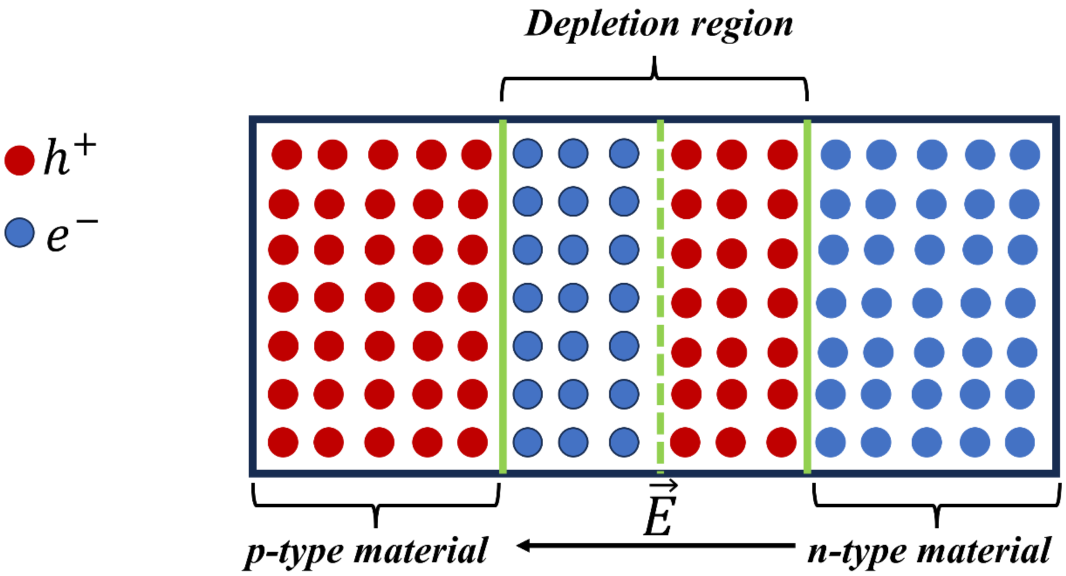

Figure 20. Schematic representation of the p-n junction.

We assume that the junction is abrupt and that the dividing line between the p-doped region and the n-doped region is placed at x = 0. We further assume that at equilibrium the fixed charges not balanced by mobile charges have a spatial density described by a step function, as represented in figure 21.

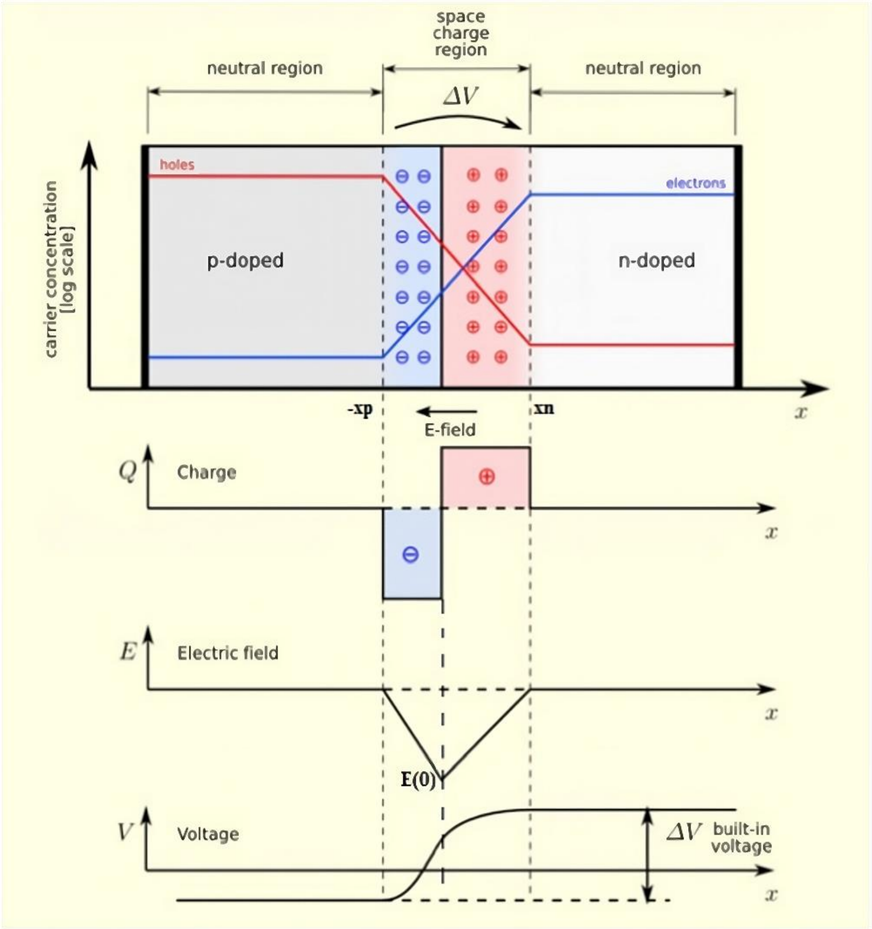

Figure 21. *Profile of charge density, electric field and potential as a function of position x.*

Denoting N_D and N_A as the concentration of donor and acceptor atoms, respectively, and similarly x_p and x_n as the lengths of the depleted regions in the x-direction in the p-region and the n-region, respectively, it is possible to calculate the width of the depletion region $W = x_p + x_n$ by using the one-dimensional Poisson's equation:

$$\frac{\partial^2 \Phi(x)}{\partial x^2} = -\frac{\rho(x)}{\epsilon} \tag{3-1}$$

In the hypothesis of depletion and with boundary conditions according to which the electric field in the neutral regions is zero, meaning the potential is constant, we obtain:

$$\begin{cases} \frac{\partial^2\Phi(x)}{\partial x^2} = 0 \quad (x < -x_p\ and\ x > x_n) \\ \frac{\partial^2\Phi(x)}{\partial x^2} = \frac{eN_A}{\epsilon} \qquad (-x_p < x < 0) \\ \frac{\partial^2\Phi(x)}{\partial x^2} = -\frac{eN_D}{\epsilon} \qquad (0 < x < x_n) \end{cases} \tag{3-2}$$

integrating the Poisson equation once and using the boundary conditions ϕ(-x_P) = ϕ_P and ϕ(x_n) = ϕ_n, we obtain

$$\begin{cases} E(-x_p) = -\left(\frac{\partial\Phi}{\partial x}\right)_{-x_p} = 0 \\ E(x_n) = -\left(\frac{\partial\Phi}{\partial x}\right)_{x_n} = 0 \end{cases} \tag{3-3}$$

That becomes:

$$\begin{cases} E_p(x) = -\frac{eN_A}{\epsilon}(x + x_p) \quad -x_p < x < 0 \\ E_n(x) = \frac{eN_D}{\epsilon}(x - x_n) \qquad 0 < x < x_n \end{cases} \tag{3-4}$$

Whose behaviour is reported in figure 21.

By imposing the continuity of the electric field at x = 0, $E_p(0) = E_n(0)$, one obtains the so-called charge neutrality equation:

$$N_A x_p = N_D X_n \tag{3-5}$$

which shows that the depletion region is greater in the less doped region. Integrating once more the expression of the electric field it is obtained:

$$\begin{cases} \Phi_p(x) = \frac{e}{2\epsilon}N_A(x + x_p)^2 + \Phi_p \qquad -x_p < x < 0 \\ \Phi_n(x) = \Phi_n - \frac{e}{2\epsilon}N_D(x_n - x)^2 \qquad 0 < x < x_n \end{cases} \tag{3-6}$$

which describes the potential as a function of x. Also in this case, by imposing the continuity of the potential at x = 0, $\Phi_p(0) = \Phi_n(0)$, one obtains the junction barrier height:

$$\Phi_n - \Phi_p = \Phi_{BI} = \frac{e}{2\epsilon}\left(N_A x_p^2 + N_D x_n^2\right) \tag{3-7}$$

By inserting the charge neutrality equation into the expression for Φ_{BI}, the width of the depleted regions in the n-type and p-type regions is obtained:

$$\begin{cases} x_p = \left(\frac{2\epsilon\Phi_{BI}N_D}{eN_A(N_A+N_D)}\right)^{1/2} \\ x_n = \left(\frac{2\epsilon\Phi_{BI}N_A}{eN_D(N_A+N_D)}\right)^{1/2} \end{cases} \tag{3-8}$$

The overall amplitude of the depletion region becomes:

$$W = x_p + x_n = \left(\frac{2\epsilon\Phi_{BI}(N_A+N_D)}{eN_AN_D}\right) \tag{3-9}$$

The junction towel-described by two relatively conductive regions (neutral regions) separated by a highly resistive depletion region of width W. A structure of this type can be likened to a parallel flat face capacitor with plates separated by distance W. The specific geometric capacitance (capacitance per unit area) can be written as:

$$C = \frac{\epsilon}{W} \tag{3-10}$$

Substituting the explicit expression of W into the equation and considering a biased junction applying a potential V, one obtains:

$$\frac{1}{C^2} = \frac{2(N_A+N_D)}{e\epsilon N_AN_D}(\Phi_{BI} - V) \tag{3-11}$$

3.2 *HETEROJUNCTIONS*

A p-n junction is defined as a heterojunction when two semiconductors with different energy gap, electron affinity, and permittivity are brought into contact. To form a high-quality heterojunction, several requirements are necessary, namely:

- The thermal expansion coefficients of the two semiconductors must be similar;
- The lattice mismatch of the two semiconductors should be as small as possible. In fact, a lattice mismatch greater than 1% at the heterojunction interface results in interface states that act as traps, or recombination centres that can accumulate charges or annihilate them, in both cases reducing the photogenerated current [108];
- Comparable electron affinities. Differences in the electron affinities of the two materials cause a discontinuity at the interface of the energy bands, leading to a cliff or a spike.

The simplest model to describe a heterostructure is the Anderson model, as it predicts the absence of interface states [109].

We start to consider the energetic structure for the two different semiconductors with energy gaps E_{g1} and E_{g2} and electron affinity χ_1 and χ_2, as reported in figure 22a. For photovoltaics purposes, it is crucial that the energy gap of the n-type material (E_{g1}), which acts as window layer, is higher than the energy gap of the p-type material (E_{g2}). When these two semiconductors are directly put in contact, the Fermi energy needs to be equal, resulting in a bending of the energy bands (figure 22b). If we denote $\Delta E_C = \chi_1 - \chi_2$ and $\Delta E_V = (\chi_1 + E_{g1}) - (\chi_2 + E_{g2})$, it is possible to determine the total built-in potential Φ_{BI} as:

$$\Phi_{BI} = \phi_1 - \phi_2 = V_{d1} - V_{d2} = E_{g2} - (E_f - E_{V2}) - (E_{C1} - E_f) + \chi_2 - \chi_1 \tag{3-12}$$

And so

$$V_d = E_{g2} - (E_f - E_{V2}) - (E_{C1} - E_f) + \Delta E_C = V_{d2} + \Delta E_V \tag{3-13}$$

As a function of the doping concentration, it is possible to observe two different behaviours in the conduction band:

- Cliff-like structure: when the junction is p⁺-n;
- Spike-like structure: when the junction is p-n⁺.

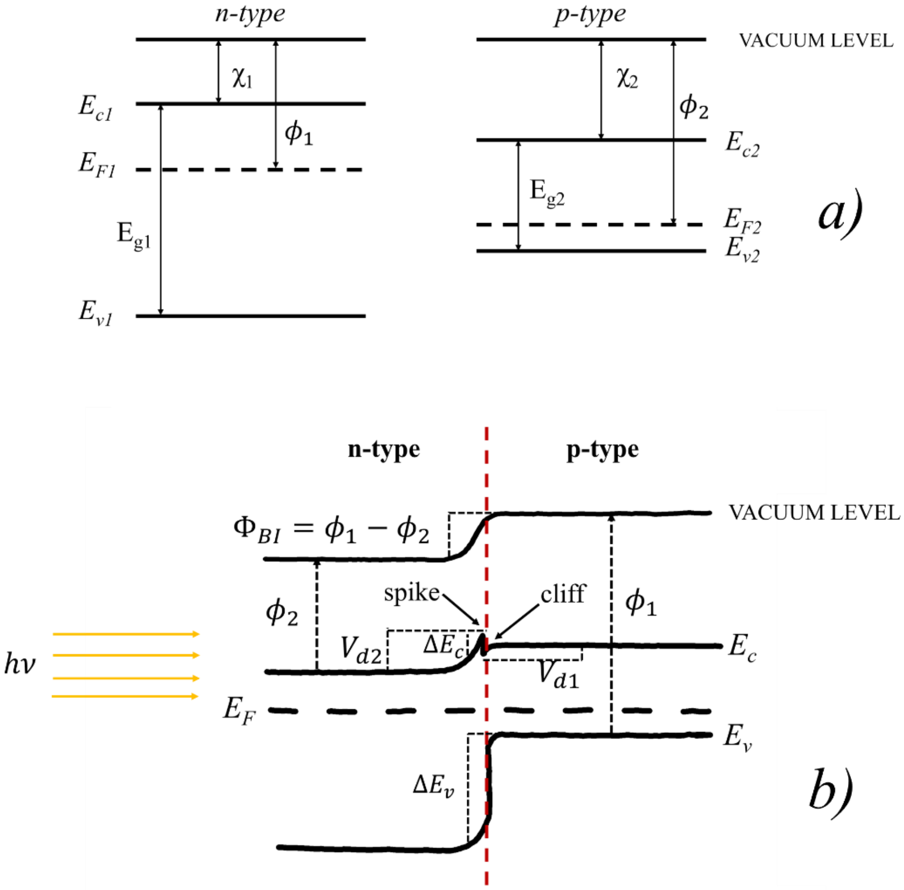

Figure 22. *Band diagram of a) two isolate semiconductor, p-type and n-type. b) band diagram of the heterostructure.*

The depletion region and capacitance are determined by solving the Poisson equation, like in the homojunction case:

$$C = \left[\frac{qN_{D1}N_{A2}\epsilon_1\epsilon_2}{2(\epsilon_1 N_{D1}+\epsilon_2 N_{A2}(\Phi_{BI}\pm V)}\right]^{1/2} \tag{3-14}$$

$$\begin{cases} x_p = \left[\frac{2N_{A2}\epsilon_1\epsilon_2(\Phi_{BI}-V)}{qN_{D1}(\epsilon_1 N_{D1}+\epsilon_2 N_{A2})}\right]^{1/2} \\ x_n = \left[\frac{2N_{D1}\epsilon_1\epsilon_2(\Phi_{BI}-V)}{qN_{A2}(\epsilon_1 N_{D1}+\epsilon_2 N_{A2})}\right]^{1/2} \end{cases} \tag{3-15}$$

In thin-film solar cells, light initially impacts the material with the wider band gap, before being absorbed in the p-type material. In the operating region of the solar cell, which correspond to the fourth quadrant of the current-voltage (IV) characteristic, the electric field at the junction pushes the photogenerated holes to the positive contact and the electrons to the negative one. Assuming there is a spike-like structure in the conduction band, if it is sufficiently narrow, electrons can easily pass through via the tunnelling effect without loss of photocurrent. In the first quadrant of the current-voltage characteristic, we are above the open circuit voltage (V_{oc}), and it is the external power supply that provides a potential difference by delivering positive charges that migrate to the negative terminal and negative charges that migrate to the positive one. In this condition, due to band bending, the holes pushed into the n-type region by the applied potential, encounter an energy barrier, accumulating at the interface. In the first quadrant, Ohm's law applies, and thus the current is a function of the number of trapped holes and the number of electrons extracted from the positive pole. In this way, the system is no longer neutral but positively charged. To maintain charge neutrality, the external power supply delivers a number of electrons equal to the sum of the number of holes extracted at the negative contact and those trapped. The presence of holes trapped by the energy barrier can cause recombination with some electrons from the conduction band.

This situation is typical in thin-film heterojunction solar cells, and this phenomenon is observed in the IV characteristic through a kink in the first quadrant, indicating a decrease in photocurrent [110]. A more detailed explanation will be presented in the chapter 6, specifically for antimony selenide-based solar cells.

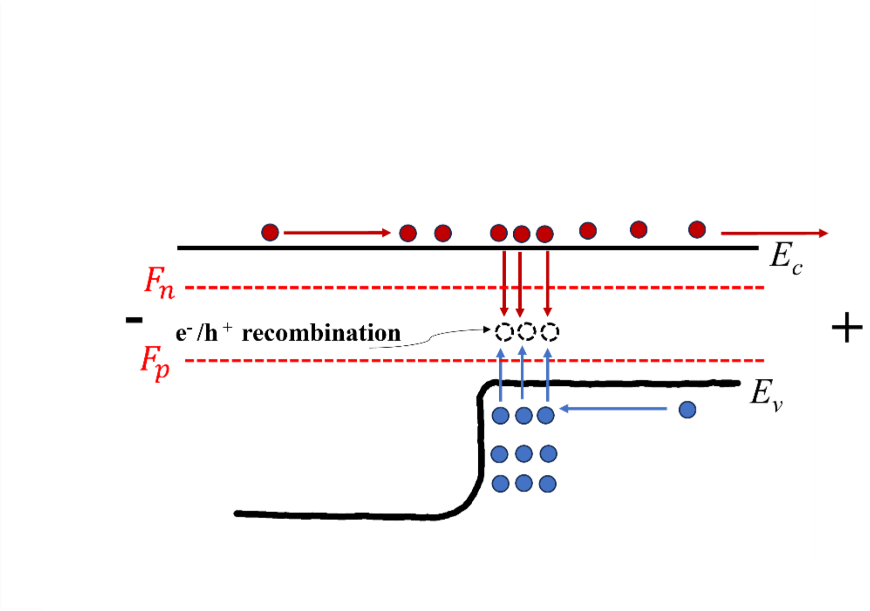

Figure 23. *Schematic representation of the recombination phenomena at the accumulation hole layer when* $V > V_{oc}$.

3.3 SOLAR CELL EQUIVALENT CIRCUIT

A solar cell can be schematized with an equivalent circuit like the one shown in figure 24, where the diode represents the ideal junction and the electric generator represents the current generated under illumination (J_{ph}). R_{sh} indicates the losses that can occur due to a short-circuit in the cell junction, while R_s represents the series resistance given by two contributions: resistance of the materials and resistance of the ohmic contacts. Finally, R_L represents the load applied to the cell terminals.

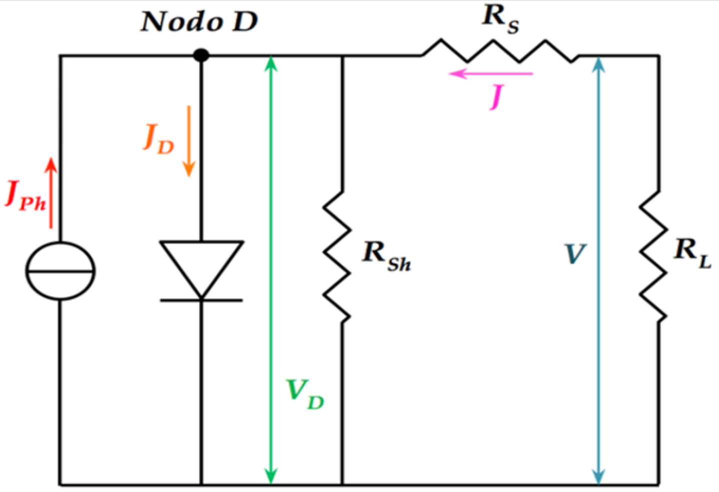

Figure 24. Equivalent circuit of a real solar cell.

Applying the first Kirchhoff's law to the node D, one obtains:

$$J_{ph} + J = J_D \rightarrow J = J_D - J_{ph} \tag{3-16}$$

In this way, one obtains the current-voltage (IV) characteristic of the real solar cell, which is the expression relating the output current to the voltage across the cell terminals for each value of generated photocurrent:

$$J = J_0 \left[\exp\left(\frac{q(V + JR_S)}{nKT}\right) - 1\right] - J_{ph} \tag{3-17}$$

In the case of an ideal homojunction solar cell, it is known that the series resistance is zero and the diode ideality factor is n = 1.

$$J = J_0 \left[\exp\left(\frac{qV}{KT}\right) - 1\right] - J_{ph} \tag{3-18}$$

The figure 25 shows the J-V characteristic of a silicon-based solar cell under various lighting conditions.

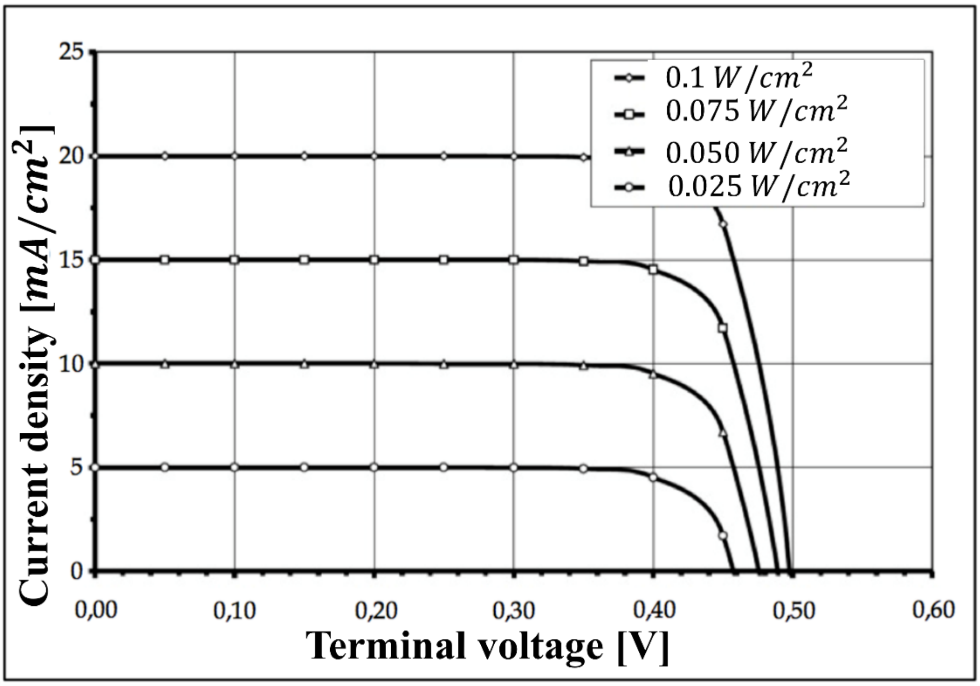

Figure 25. *Current-Voltage (IV) characteristic of a Silicon cell under various illumination levels. By convention the real characteristic is shown in the first quadrant, i.e. the current values collected experimentally in the fourth quadrant are multiplied by -1.*

From figure 25, it is possible to define the fundamental photovoltaic parameters of the solar cell:

- The intersection of the characteristic curve with the current axis, i.e., V = 0, corresponds to the current called short-circuit current indicated by J_{SC};
- The intersection of the characteristic curve with the voltage axis, i.e., J = 0, corresponds to the open-circuit voltage indicated by V_{OC};
- P_M indicates the maximum power point, i.e., the power delivered by the solar cell corresponding to the coordinates J_M and V_M, where P_M is the product $P_M = J_M \times V_M$.
- In general, a solar cell is a device when exposed to sufficiently energetic light: There exists a potential difference V_B across its terminals;
- It generates an electric current at its output is proportional to the intensity of the incident radiation;
- There is an electrical power P_{out} at the terminals of the cell proportional to the incident luminous power, when R_s and R_{sh} are near the ideality.

The photovoltaic conversion efficiency of a solar cell can be defined as:

$$\eta = P_{out} / P_{inc} \qquad (3\text{-}19)$$

where P_{out} is the power output of the solar cell and P_{inc} is the incident luminous power.

The maximum power generated by a solar cell in the ideal case would be:

$$P = J \cdot V = VJ_{ph} - VJ_0 \left[\exp\left(\frac{qV}{nKT}\right) - 1\right] \qquad (3\text{-}20)$$

In the hypothesis that $J_{ph} >> J_0$, calculating the derivative of the output power with respect to the potential, we obtain:

$$\frac{\partial P}{\partial V} = J_{ph} + J_0 - J_0(1 + \gamma V_M)e^{\gamma V_M} = 0 \rightarrow e^{\gamma V_M} \approx \frac{J_{ph}}{J_0(1+\gamma V_M)} \qquad (3\text{-}21)$$

Having set $\gamma = q/nKT$.

This expression cannot be solved analytically, but it is still possible to calculate the analytical expression of the maximum power. By writing the expression of the current corresponding to the value V_M, we obtain:

$$J_M = J_{ph} - J_0 e^{\gamma V_M} = J_{ph} - \frac{J_{ph}}{1+\gamma V_M} = \frac{J_{ph}\gamma V_M}{1+\gamma V_M} \qquad (3\text{-}22)$$

Remembering that the maximum power is given by the product of the maximum current and the maximum voltage, the expression is derived:

$$P_M = J_M \cdot V_M = V_M J_{ph} \frac{\gamma V_M}{1+\gamma V_M} \qquad (3\text{-}23)$$

The efficiency, being the ratio between the maximum output power and the incident light power, can be rewritten as $\eta = (J_M V_M)/P_{inc}$. Multiplying the numerator and denominator by the $J_{SC} \cdot V_{OC}$ product introduces a new parameter, called fill factor (FF), defined as

$$FF = \frac{J_M V_M}{J_{sc} V_{oc}} \qquad (3\text{-}24)$$

The efficiency can be rewritten in terms of fill factor as

$$\eta = FF \frac{J_{sc} V_{oc}}{P_{inc}} \qquad (3\text{-}25)$$

As shown in Figure 26, the product $J_{sc} \cdot V_{oc}$ represents the area of the minimum rectangle that circumscribes the characteristic, and $J_M \cdot V_M$ represents the area of the maximum rectangle inscribed within the JV curve. Therefore, the Fill Factor is the ratio between the areas of these two rectangles.

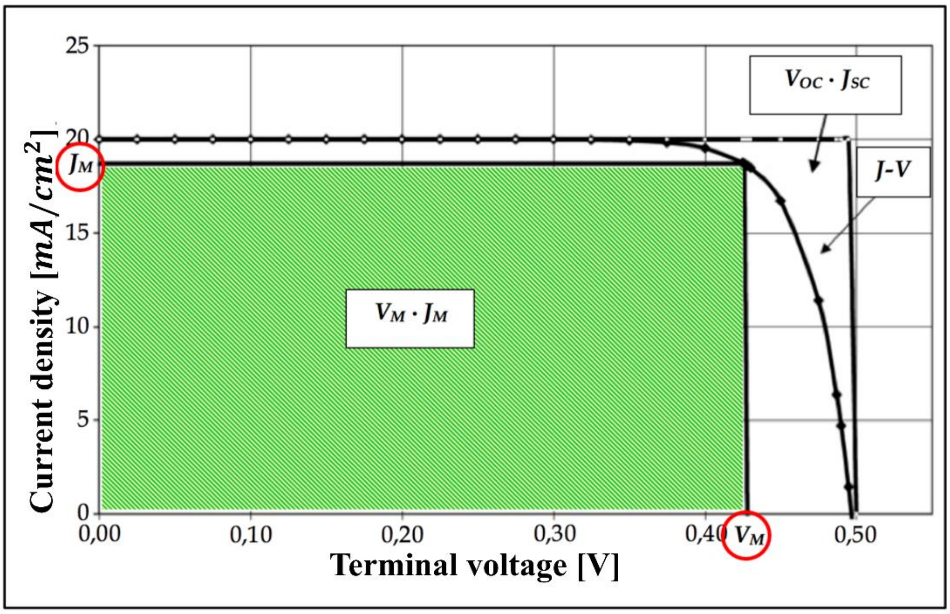

Figure 26. *Geometrical representation of fill factor.*

3.4 ***PHOTOELECTRIC AND PHOTOVOLTAIC EFFICIENCY***

3.4.1 Photoelectric efficiency

The spectrum of solar radiation exhibits the emission characteristics of a black body and is well described by Planck's formula, outside the atmosphere, considering a temperature on the surface of the Sun of 5760 K.

$$I(\lambda, T) = \frac{1.62 \cdot 10^{-9} \cdot C_1 \cdot \lambda^{-5}}{\exp\left(\frac{C_2}{\lambda T}\right) - 1} \tag{3-26}$$

where the constant $1.62 \cdot 10^{-9}$ accounts for the attenuation factor of radiation for the Earth-Sun distance and the loss due to the Earth's albedo, T represents the absolute temperature, and the constants C_1 and C_2 are $C_1 = 2\pi hc^2 = 3.7419 \cdot 10^{-12}\ Wcm^2$ and $C_2 = \frac{hc}{K} = 1.4388\ cmK$.

Knowing that the energy of the electron can be written as $E_e = h\nu - E_g$, then, defining the characteristic wavelength of the semiconductor as $\lambda_g = hc/E_g$, the relation defining the energy of the electron can be rewritten in terms of this wavelength.

$$E_e = hc\left[\frac{1}{\lambda} - \frac{1}{\lambda_g}\right] \tag{3-27}$$

This relation shows that the internal photoelectric effect occurs for photons with wavelengths shorter than λ_g.

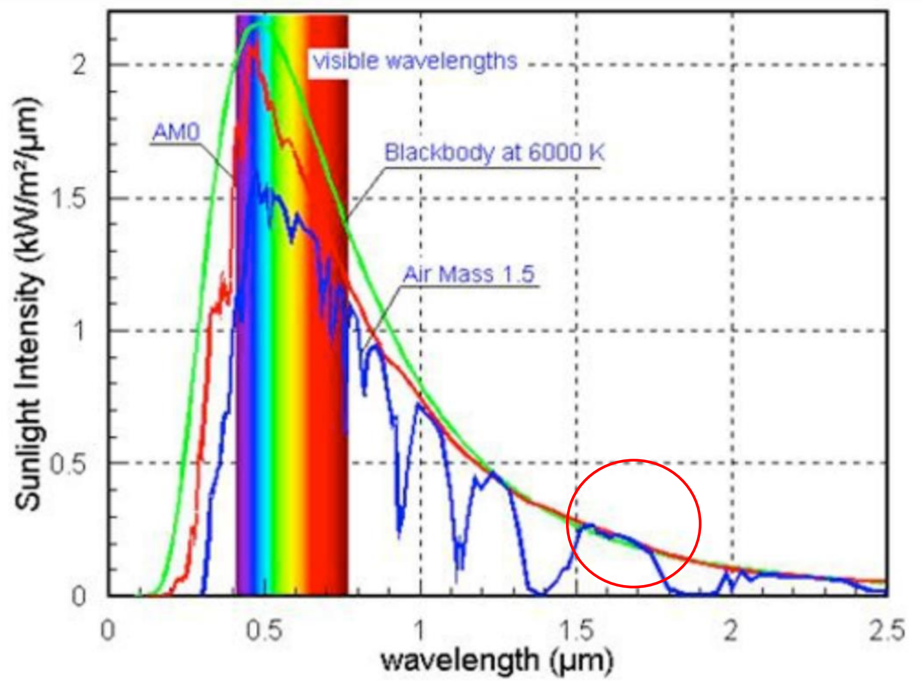

Figure 27. *Blackbody spectrum (green line), AM1.5 and AM0 solar spectrum (blue and red line respectively).*

In the solar spectrum shown in Figure 27, let's consider an infinitesimal interval of width between λ and λ+dλ, and calculate the number of photons that cross the unit area per unit time.

$$dN_{ph} = I_\lambda \frac{d\lambda}{h\nu} = \frac{1}{hc} I_\lambda \lambda d\lambda \tag{3-28}$$

Considering a photon with a wavelength above the threshold for internal photoelectric effect, the number of photons just calculated corresponds to an equal number of electrons and holes each requiring an energy equal to E_g to be brought into the conduction band or the valence band. Therefore, the energy expenditure for creating the electron-hole pair will be:

$$I_{E_g} = E_g \int_{E_g}^{\infty} dN_{ph}(\lambda < \lambda_g) = \frac{1}{\lambda_g}\int_0^{\lambda_g} I_\lambda(\lambda)\lambda d\lambda \tag{3-29}$$

The photoelectric efficiency is defined as the ratio:

$$\eta_{ph} = \frac{I_{E_g}}{I} = \frac{1/\lambda_g \int_0^{\lambda_g} I_\lambda(\lambda)\lambda d\lambda}{\int_0^{\infty} I_\lambda d\lambda} \tag{3-30}$$

3.4.2 ***Photovoltaic efficiency***

If we denote by $dN_{ph}(E > E_g)$ the number of photons per second present in the infinitesimal element of the solar spectrum between λ and $\lambda+d\lambda$ with energy greater then E_g, the photocurrent will be expressed by the charge of the electron multiplied by this number, further multiplied by a factor Q, less than one, representing the external quantum efficiency.

$$dJ_{ph} = QqdN_{ph}\left(E > E_g\right) \tag{3-31}$$

This efficiency is defined as the fraction of electrons that are effectively collected at the electrodes compared to the number of photogenerated electrons. Considering the expression for dN_{ph} already found:

$$dN_{ph} = \frac{1}{hc} I_\lambda \lambda d\lambda \tag{3-32}$$

Substituting dN_{ph} into the equation for J_{ph} and integrating up to the semiconductor gap wavelength gives:

$$J_{ph} = \frac{q}{hc}\int_0^{\lambda_G} QI_\lambda \lambda d\lambda \tag{3-33}$$

In the ideal case where all the photogenerated charges are collected in the external circuit (Q = 1), the efficiency turns out to be:

$$\eta = \frac{J_M V_M}{P_{inc}} = \frac{J_{ph}\frac{\gamma V_M}{\gamma V_M+1}}{P_{inc}} = \frac{1}{P_{inc}} \cdot \frac{\gamma V_M}{\gamma V_M+1} \cdot \frac{q}{hc}\int_0^{\lambda_G} I_\lambda \lambda d\lambda \tag{3-34}$$

To explicitly evaluate the maximum power V_M, it is necessary to utilize the empirical expression:

$$V_M \approx V_{oc} - \frac{1}{\gamma}\ln(\gamma V_M) \tag{3-35}$$

In general, in thin film solar cells the quantity $\frac{1}{\gamma}\ln(\gamma V_M)$ is negligible compared to V_{oc}. In particular, in our Sb_2Se_3-based solar cells this quantity is about 0.02 V, considering V_M equal to 0.06 V and V_{oc} 0.5 V.

Furthermore, remembering that we consider n =1 and $J_{ph} >> J_0$, we obtain:

$$V_M \approx V_{oc} = \frac{nKT}{q}\ln\left[\frac{J_{ph}}{J_0}+1\right] = \frac{KT}{q}\ln\left(\frac{J_{ph}}{J_0}\right) = \frac{KT}{q}\left[\ln(J_{ph}) - \ln(J_0)\right] \quad (3\text{-}36)$$

The reverse current J_0 is defined as an unwanted signal in a photodetector in the absence of light, resulting from thermally excited electrons or leakage currents in the junction region, and it is expressed as

$$J_0 = Ce^{-\frac{E_g}{BKT}} \quad (3\text{-}37)$$

Where B is a numeric factor between 1 and 2 that depends on which type of junction is under consideration and the constant $C = 1.6 \cdot 10^6$ A/cm^2.

By explicitly expressing J_{ph} and J_0 in the expression for V_M, we obtain a representation of the maximum efficiency as a function of the energy gap value of the semiconductors used to manufacture the solar cells, considering B = 1.

$$V_M \approx \frac{E_g}{q} - \frac{KT}{q}lnC + \frac{KT}{q}\ln\left[\frac{q}{hc}\int_0^{E_g} QI_\lambda \lambda d\lambda\right] \quad (3\text{-}38)$$

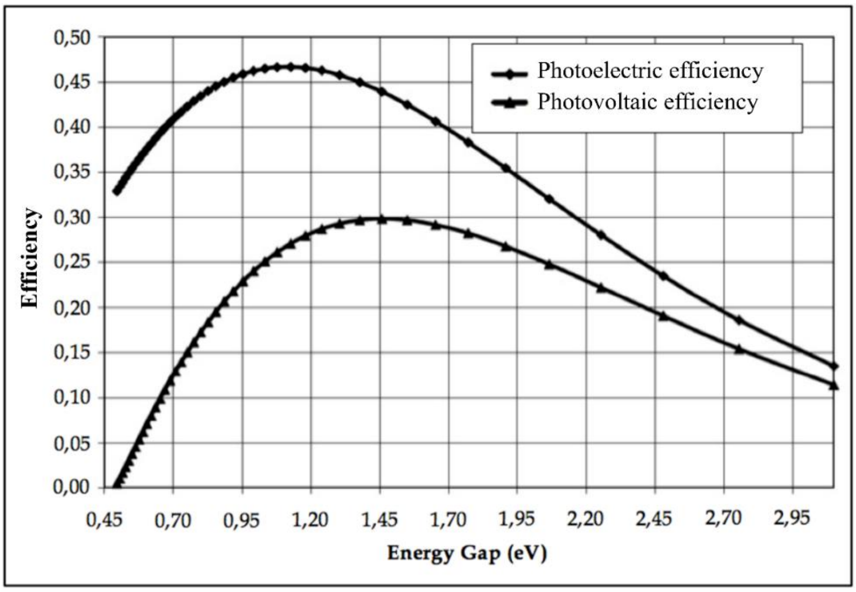

Figure 28. *Comparison of the photoelectric and photovoltaic efficiency trends.*

The two curves in figure 28, represent the photoelectric efficiency and the photovoltaic efficiency. It is noted that the maximum efficiency value decreases, going from 47% in the photoelectric efficiency curve to 30% in the photovoltaic efficiency curve. Furthermore, there is a clear shift of the maximum point to higher E_g values. In the photoelectric efficiency curve, the point of maximum efficiency corresponds to an energy gap of 1.1 eV, namely silicon. Instead, the maximum of the photovoltaic efficiency curve is about 1.45 eV, which well fits the energy gap of GaAs and CdTe. The maximum efficiency of silicon-based cells is comparable to the theoretical one obtained with the model just described, reaching the maximum limits of its technology.

FABRICATION OF SB$_2$SE$_3$-BASED SOLAR CELLS

The Sb_2Se_3-based solar cell studied in the frame of this PhD thesis is in superstrate configuration, with the stratigraphy shown in the figure 29.

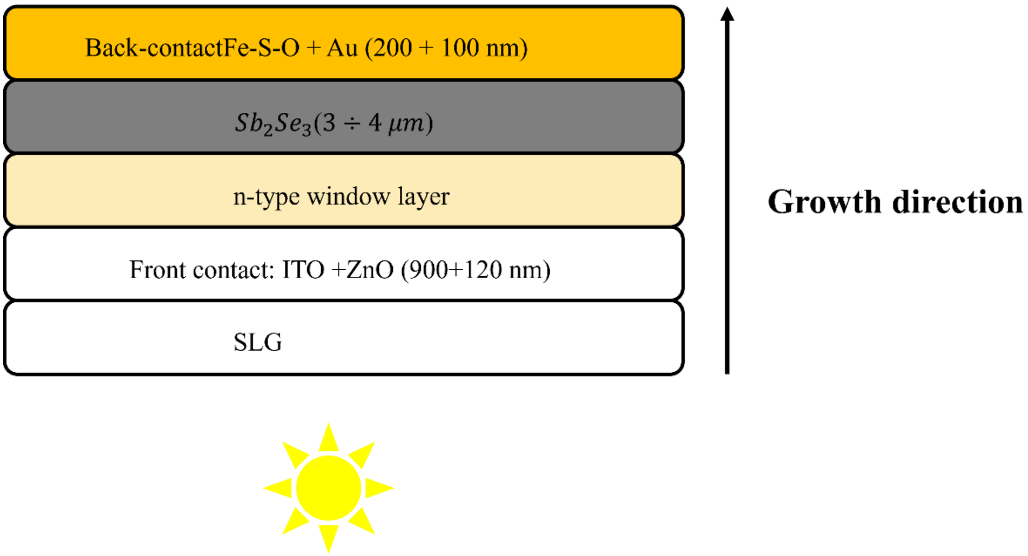

Figure 29. *Sketch of the Sb_2Se_3-based solar cell in superstrate configuration.*

All layers, except for Sb_2Se_3, are grown by magnetron sputtering using DC power supply (Back-contact and ITO) or RF power supply (window layer and ZnO). To determine the main photovoltaic parameters of solar cells, a voltage-current density (J-V) characteristic measurement is performed using a continuous LOT-Oriel solar simulator (Oriel, Irvine, CA, USA), equipped with an air mass AM1.5G filter. The solar simulator is equipped with a 600 W Xenon lamp (Oriel, Irvine, CA, USA) that can produce a light power density of 1 kW/m^2. To ensure accuracy, a calibrated pyranometer was used as a reference, and the measurements were taken at a standard temperature of 298 K.

Before performing the J-V measurement, the solar cell undergoes a treatment known light soaking (LS). This process, lasts about one hour and involves illuminating the cell from the front contact side using an intense light source, typically halogen lamp, to achieve a surface temperature of around 80°C. Experimental evidence has shown that this enhances the photovoltaic parameters in thin film solar cells, although the underlying mechanisms are not yet fully understood. It is believed that this treatment facilitates the filling of electron traps located at the heterojunction interface while simultaneously passivating bulk defects within the absorber material, which can serve as channels for reverse current transport [111]. An example is illustrated in figure 30, which shows the J-V characteristic of our Sb_2Se_3-based solar cell, both before and after the light soaking treatment.

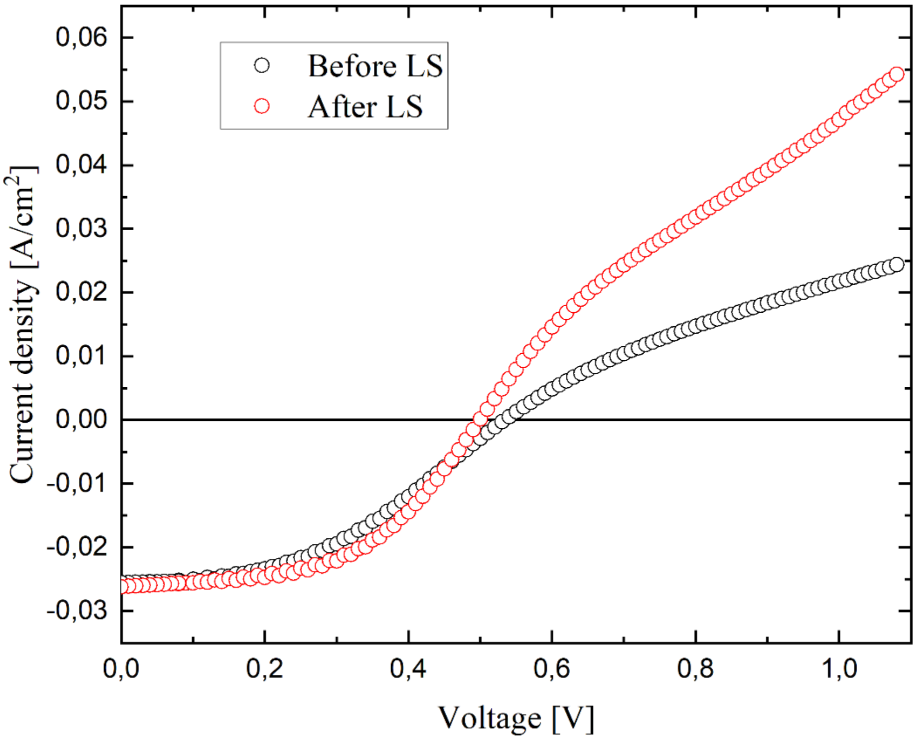

Figure 30. *Comparison of the J-V characteristic before (black dots) and after (red dots) the LS.*

The main photovoltaic parameters are summarized in Table 2. Following the light soaking treatment, there was a significant variation in the fill factor and power conversion efficiency (PCE), with increases of 21% and 19%, respectively.

Table 2. *Main photovoltaic parameters of the Sb_2Se_3-based solar cell before and after the LS treatment.*

	Before LS	After LS
V_{oc} [mV]	534	500
J_{sc} [mA/cm²]	25.5	26.2
F.F.	0.43	0.52
PCE [%]	5.68	6.77

4.1 SUBSTRATE

The choice of the substrate on which the solar cell layers are deposited is of great importance. Historically, high-efficiency thin-film solar cells have been deposited on rigid glass substrate. This substrate must exhibit great optical transmission in the visible range because the solar photons have to penetrate the substrate, to reach the active layers of the cell. The glass substrate used is "Soda Lime Glass" (SLG), which is characterized by a sufficiently high softening point (between 790 and 800 K) to allow heat treatments for the deposited materials. Furthermore, it is characterized by high availability on the market and allows for cost-effective final device fabrication. However, commercial glasses contain iron impurities, which reduce the natural transmission of light, therefore for photovoltaic purposes it is advisable to use SLG with a low content of iron impurities as a substrate, such as iron-free SLG.

In addition to SLG, polymeric materials were also tested as substrates. For example, Kapton polyimide, exhibits suitable optical properties. However, it has rather modest processing temperatures (around 720 K), compared to SLG glass.

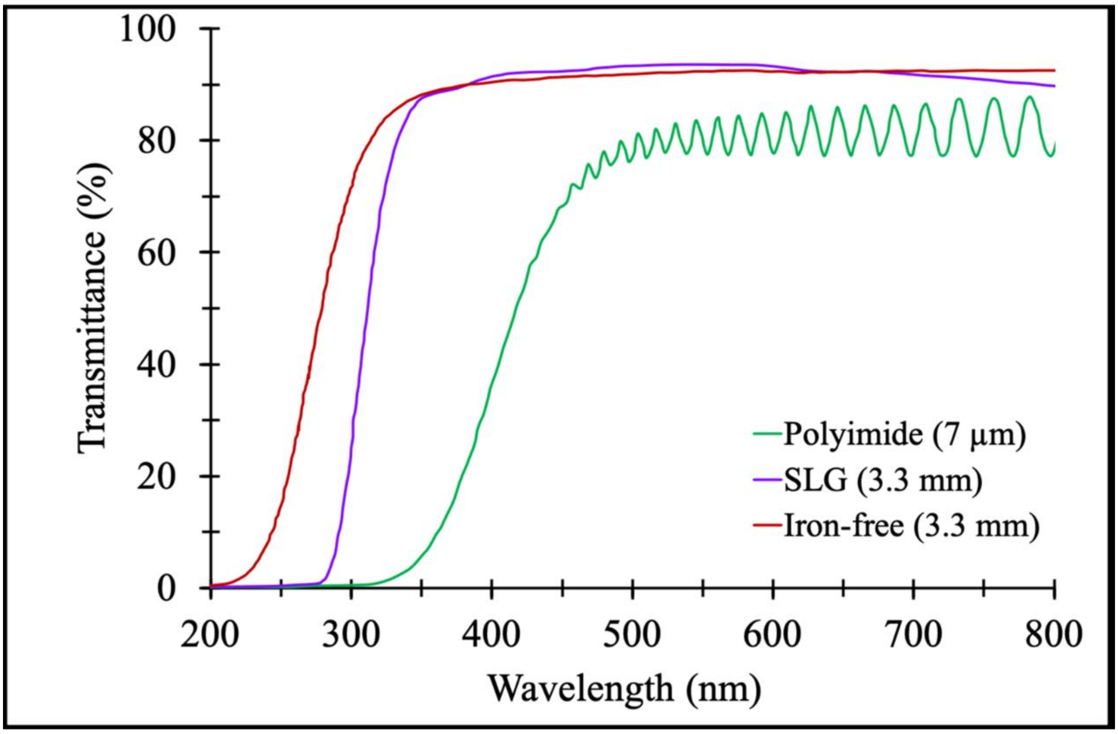

Figure 31. *Transmittance spectra of Polyimide (green line), SLG (purple line) and SLG-iron free (red line). The figure is taken from [15].*

Furthermore, as shown in figure 31, even if it has good optical transmittance properties, it is still lower compared with SLG.

Cleaning the SLG substrate is the first critical step for a good performance of the solar cell, as it must guarantee good adhesion of the films on the glass surface. Initially, the glass, measuring 1 inch^2, is mechanically washed using absorbent paper soaked in a solution of 60% acetone (CH_3COCH_3) and 40% isopropyl alcohol ($CH_3CH(OH)CH_3$) in order to remove the macroscopic impurities presents on the glass surface. Afterward, glass undergoes a plasma etching process in an oxidizing environment for ten minutes. The machine maintains a vacuum of approximately $5 \cdot 10^{-1}$ mbar inside, while external air is introduced into the chamber, to generate a plasma. Oxygen ions within the plasma bombard the substrate, oxidizing any remaining organic residues on the glass surface.

At the end of the whole process, the glass surface is cleaned and suitable to be used as a substrate for the subsequent thin films deposition that gives the complete Sb_2Se_3-based solar cell.

4.2 TRANSPARENT CONDUCTIVE OXIDES (TCO)

In thin film solar cells, it is crucial to use front contacts that are transparent (with optical transparency of approximately 90%, see figure 32a) to the visible part of the solar spectrum while being conductive at the same time. The low resistivity requirement is essential to collect the photogenerated carriers without introducing series resistances into the device. In general, materials that are transparent to the visible component of the solar spectrum have an energy gap greater than 3 eV. Therefore, in principle, it is challenging to achieve both conductivity and transparency in these materials, given the difficulty in doping them. Among these wide band gap semiconductors, only oxides are considered for this purpose, as they can be doped to the point of degeneracy. Above a certain threshold of embedded dopant atoms, bands of energy levels in the forbidden band energy may form. This energy band, if close enough, can merge with the conduction band. In this case the electrons can pass from the donor level to the conduction band with energies comparable to the thermal ones. This causes a shift of the Fermi energy within the conduction band, resulting in an electrical conductivity comparable to metals. A Fermi level shifted to energies greater than the minimum of the conduction band and all the energy levels below the Fermi level are occupied by electrons, describes the degeneracy condition. Moreover, in this scenario, the energy gap is really increased being in this scenario equal to the energy difference between the top of the valence band and the first free energy level within the donor band. This phenomenon is known as the Burstein-Moss effect. If, as shown in the figure 32b, ΔE is defined as the difference in energy between the bottom of the conduction band and the Fermi level and E_g is the original energy gap, then the apparent energy gap will be:

$$E_g^{eff} = E_g + \Delta E \tag{4-1}$$

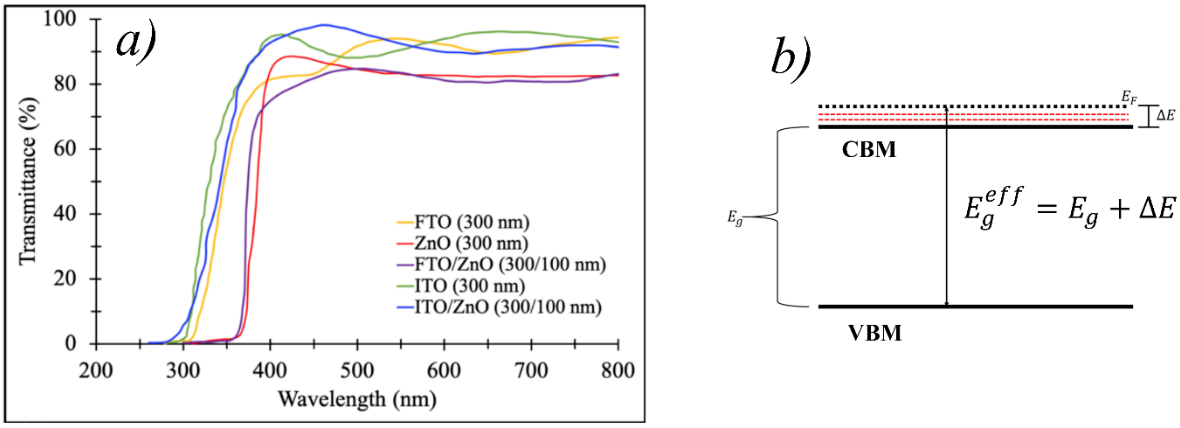

Figure 32. *a) Transmittance spectra of the most common TCOs used [15]. b) Schematic representation of the band model of a degenerate semiconductor.*

A typical TCO that exploits this phenomenon is indium tin oxide (ITO), with a typical absorption in the near-infrared region due to free charges. This material exhibits an energy gap of about 3.5 eV and high transparency in the visible region. The ITO prepared in our laboratory is obtained by reactive DC magnetron sputtering. The sputtering gas is a mixture of Ar and O_2 with an oxygen flux fixed at 2.5% of the total. The power density incident on the target is 1.75 W/cm^2 that permits a deposition rate of about 11 Å/s.

The target material is composed of 90% In_2O_3 and 10% SnO_2, which allows tin atoms to replace indium atoms, creating a sufficiently dense band of donor levels in order to exploit the Burstein-Moss effect and obtaining a free carrier concentration of about 10^{20} cm^{-3} [112].

During the deposition, the substrate is heated at 500 °C, in order to promote good crystallinity, which leads an enlargement of the grains size. This increase in grain size enhances carrier mobility, consequently, reducing the resistivity of ITO, as demonstrated by Ray et al. [113].

Using these parameters, we obtain an ITO thin film with a resistivity about $2 \cdot 10^{-4}$ Ωcm, with a thickness of 900 nm.

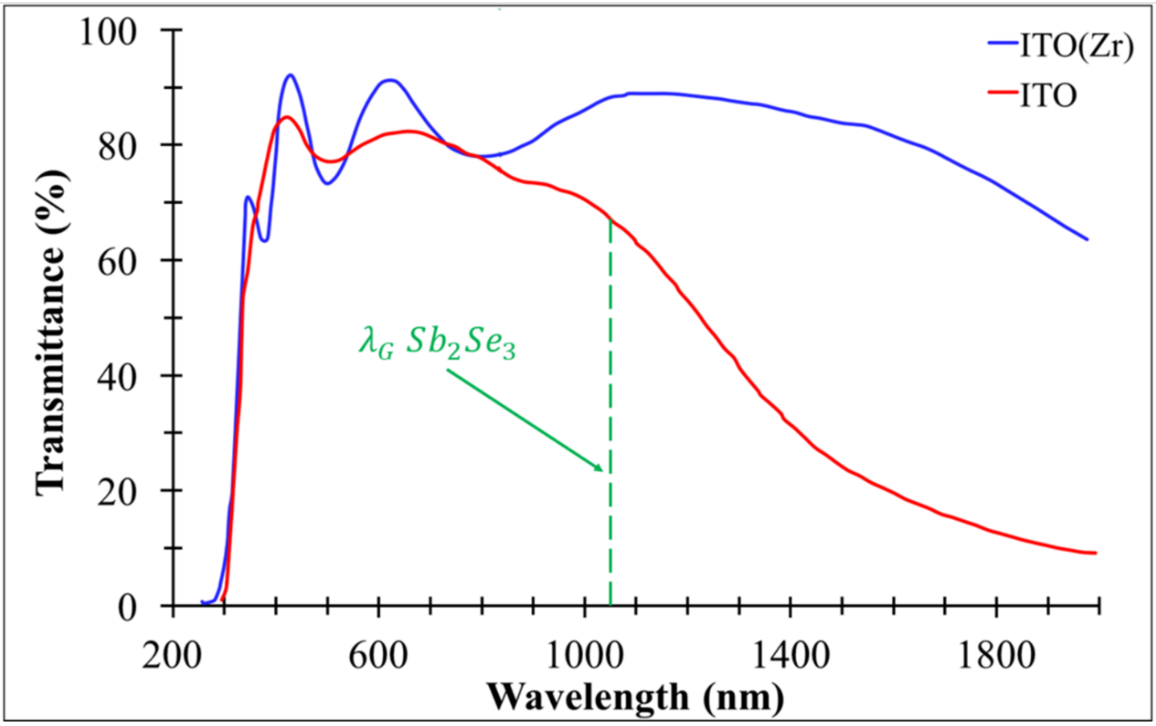

***Figure* 33.** *ITO transmittance spectra with (blue line) and without (red line) zirconium inclusions. The image is adapted from [114].*

As shown in figure 33, transparency of the material decreases down to 70%, for wavelengths greater than 825 nm, resulting in absorption of part of the photons intended for the absorber material. This phenomenon occurs because the electrons in the impurity bands are not only thermally activated, but also promoted to the conduction band by photons with near-infrared (NIR) energy. To overcome this problem, ITO can be doped with a small amount of high permittivity oxides, such as ZrO_2 or HfO_2, to shift the plasma frequency to longer wavelengths. This optimization allows for optimal transmittance in the NIR, without the absorption phenomenon by free carriers. Importantly, this doping method does not alter the concentration or the mobility of the charge carriers, resulting in no change in TCO resistivity. To prevent the diffusion of In and Sn atoms from the TCO layer, during the growth of the subsequent layers, which could create preferential metallic path for current flow and cause a short circuit in the solar cell. It is necessary to mechanically isolate ITO from the other layers. This is achieved by introducing a high resistivity layer (HRL), typically ZnO. Zinc oxide is a semiconductor belonging to II-VI group that crystallize in hexagonal Wurtzite structure. It has an energy gap about 3.3 eV and exhibits an optical transparency near 90% in the visible and NIR region (see figure 32a, green line). The n-type conductivity of ZnO is attributed to deviations in stoichiometry during growth and is dependent on the oxygen concentration within the crystalline structure (see figure 34). In particular, the electrical properties are governed by the presence of oxygen vacancies (V_O) and interstitial sites of zinc (Zn_i), both of which act as donor defects.

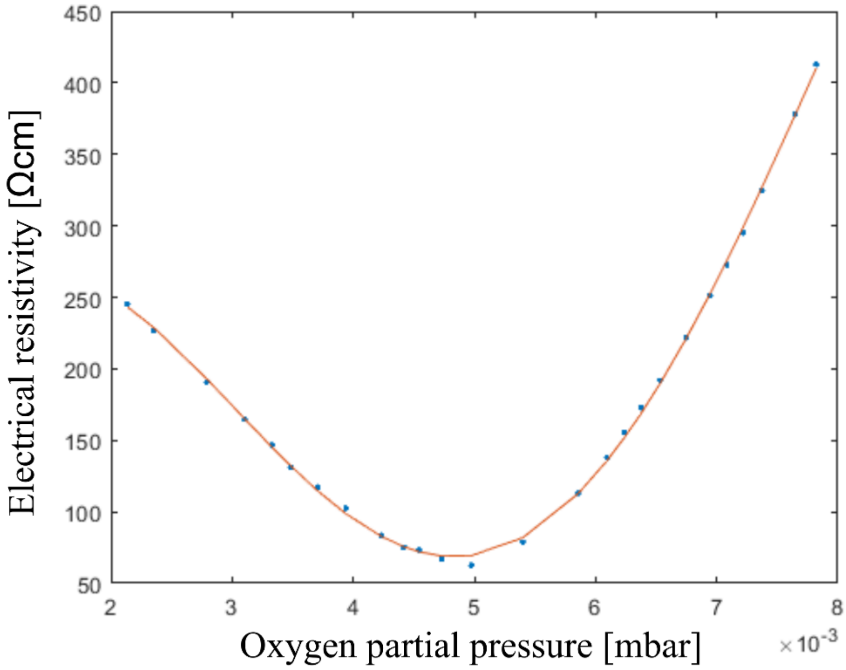

Figure 34. *Trend of ZnO resistivity as a function of the partial pressure of oxygen in the chamber during the growth. The image is adapted from [115].*

Here, ZnO is deposited starting from a Zn metal target using reactive RF magnetron system, using a power density of 1.56 W/cm^2, that provides a deposition rate about (2.2) Å/s. The substrate is heated at about 400 °C to promote a good crystalline quality.

The sputtering gas is a mixture of argon and oxygen, with an oxygen flux 15% of the total. This oxygen content allows us to obtain a ZnO film with a resistivity about 10^3 Ωcm, with a thickness of 120 nm.

Another reason for introducing ZnO as a buffer layer is to prevent direct contact between ITO and the absorber material through the thin layer of the window material, which may contain pinholes. This avoids short-circuiting the solar cell.

4.3 <u>WINDOW LAYERS</u>

The window layer (WL) serves as substrate on which the p-type absorber material is grown, in this case Sb_2Se_3, and thus acts as the n-partner in forming the p/n heterojunction. As the name suggests, the window layer needs to be, as transparent as possible, to the visible light and must exhibit n-type conductivity.

In this study, five different WL materials were tested to assess their impact on the preferential grain orientations of the antimony selenide and their correlation with key photovoltaic parameters, such as V_{oc} and J_{sc}. All WL materials were grown through RF magnetron sputtering, maintaining an Ar pressure about 5×10^{-1} Pa. The only deviation was observed in sample B, where reactive sputtering was utilized, introducing a pressure of CHF_3 gas at 5×10^{-3} Pa into the chamber. Table 3 provides details of the deposition parameters for each window layer.

Table 3. *Deposition RF sputtering parameters for each window layer.*

WL material and working atmosphere	Substrate temperature [°C]	Power density [W/cm^2]	Deposition rate [nm/s]	Thickness [nm]	Sample name
CdS (Ar)	250	0.7	0.40	300	A
CdS (Ar + CHF_3)	250	0.9	0.40	300	B
CdS + CdSe (Ar)	250	0.7 and 0.6	0.40 and 0.44	300 + 50	C
CdS + As_2S_3 (Ar)	250	0.7 and 0.6	0.40 and 0.24	300 + 50	D
CdS + $Zn_{0.15}Cd_{0.85}S$ (Ar)	250	0.7 and 0.8	0.40 and 0.40	60 + 30	E

In sample A cadmium sulphide (CdS) was utilized., CdS is known for its direct energy gap of 2.42 eV and crystallize in a hexagonal structure [116]. It is worth noting that CdS is a popular choice for window layer in high-efficiency thin-film solar cells. Furthermore, the CdS/Sb_2Se_3 heterostructure is a good reference point, because the current PCE record for Sb_2Se_3-based solar cell was achieved using CdS as the WL [15,35,117]. However, a major challenge with this structure is the significant lattice mismatch between CdS and Sb_2Se_3. In fact, with a CdS lattice parameter of a_{CdS} = 4.14 Å [118] and assuming antimony selenide grows in the preferred orientation (parallel to the (002) planes), we have to consider the b = 3.99 Å axis [57]. The lattice mismatch is around 3.7%, and it is calculated using the equation [119]:

$$\delta = \frac{2|a_{Cds} - b_{Sb_2Se_3}|}{a_{Cds} + b_{Sb_2Se_3}} \cdot 100 \qquad (4\text{-}2)$$

A lattice mismatch exceeding 1% introduces a significant number of interfaces states adversely affecting the device performance. Simulations suggest that this mismatch can be minimized introducing a double buffer layer composed by ZnS and CdS, aiming to reduce interface states and enhance device functionality [120].To enhance the chemical stability of CdS, during its deposition, CHF_3 gas is introduced into the sputtering chamber. The plasma discharge within the sputtering has adequate energy to dissociate the CHF_3 molecule releasing fluorine ions. These being electronegative, naturally migrate towards the positive electrode (substrate), where they react with cadmium to form CdF_2 This compound segregates within the CdS grain boundaries, effectively passivating them as an insulating material [121].

Furthermore, the highly energetic fluorine ions, accelerated by the electric field inside the glow discharge, can impact the surface of the growing CdS film dislodging the less tightly bound sulphur and cadmium atoms. This process helps to prevent the formation of unwanted stoichiometric excesses resulting in a CdS film with improved optical transparency (as shown in figure 35) and structural properties.

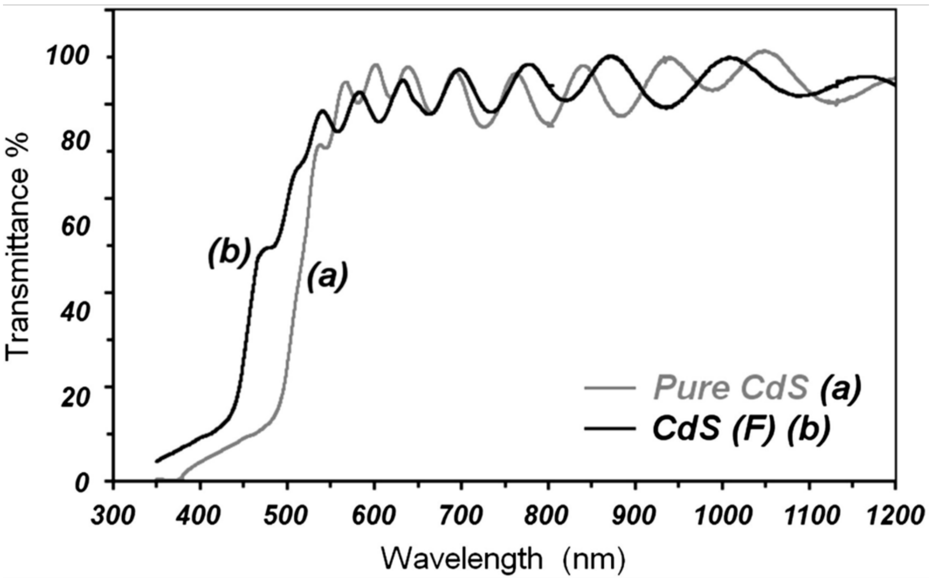

Figure 35. *Transmittance spectrum of CdS in the presence and absence of CHF_3. The image is taken from [121].*

The sample B is characterized by CdS:F as window layer exhibiting a direct energy gap of 2.85 eV and crystallizing in hexagonal structure [122].

In the Sb_2Se_3 composition, selenium has a higher vapour pressure compared to antimony. Consequently, during the antimony selenide deposition selenium vacancies are generated. As reported in the previous chapter, these V_{Se} act as deep donor levels, influencing the transport of the charge carriers in the solar cell. In sample C, CdSe was introduced to interact with Sb_2Se_3 during the growth, aiming to fill the selenium vacancies by utilizing Se diffusion from CdSe. From crystal structure standpoint, CdSe has an energy gap of 1.74 eV and crystallizes in a hexagonal crystal structure [123]. Ensuring a good crystalline quality of the absorber layer is crucial for reducing lattice defects and controlling the preferential orientation of the crystalline grains. One potential approach is to use arsenic sulphide (As_2S_3) to exploit the quasi-rheotaxy effect during the Sb_2Se_3 growth [124,125].

In the quasi-rheotaxy approach, the surface layer of a material essentially behaves like a liquid, albeit at temperatures up to 30% lower than the material melting point. Consequently, the material maintains its structural integrity without undergoing full melting but giving the appearance of molten surface layers. This phenomenon enhances the mobility of adsorbed atoms allowing them to form clusters on the surface. The increased mobility of these clusters facilitates coalescence and orientation, thereby promoting the growth of large crystalline grains [126,127]. This effect is particularly pronounced in glassy systems like As_2S_3 [128]. Quasi-rheotaxy retains the advantages of traditional rheotaxy, which involves thin film growth on liquid surfaces, while avoiding its primary drawback, the formation of undesired droplets.

Arsenic sulphide crystalizes in a monoclinic crystal structure exhibiting an energy gap of 2.35 eV [129].

In the last sample (sample E) cadmium sulphide with a 15at% zinc content its crystal structure was tested as the WL. The system CdS-ZnS follow the Vegard’s law [130,131], where the energy gap of CdS increases linearly with the zinc content. An optimal concentration of 15 at% Zn has been determined to maximize transparency and achieve a window layer resistivity suitable for photovoltaic applications. To accurately estimate the real energy gap and the percentage of zinc inside the target material a UV-VIS spectroscopy measurement were performed on a thin film of ZnCdS deposited on glass. To extract these quantities one can make use of a Tauc plot reported in[132]:

$$(\alpha h\nu)^2 = B\left(h\nu - E_g\right) \tag{4-3}$$

Where α is the absorption coefficient, ν is the frequency of incident photons, E_g is the energy gap and B is a constant. The exponent 2 is utilized because ZnCdS is a direct energy gap semiconductor. For indirect energy gap semiconductor an exponent ½ is typically used. The theory behind this equation assumes that the energy $h\nu$ of the photon is slightly higher than

E_g. In this case, transitions from VB to CB involve states near the band edges, which results in a parabolic dispersion law.

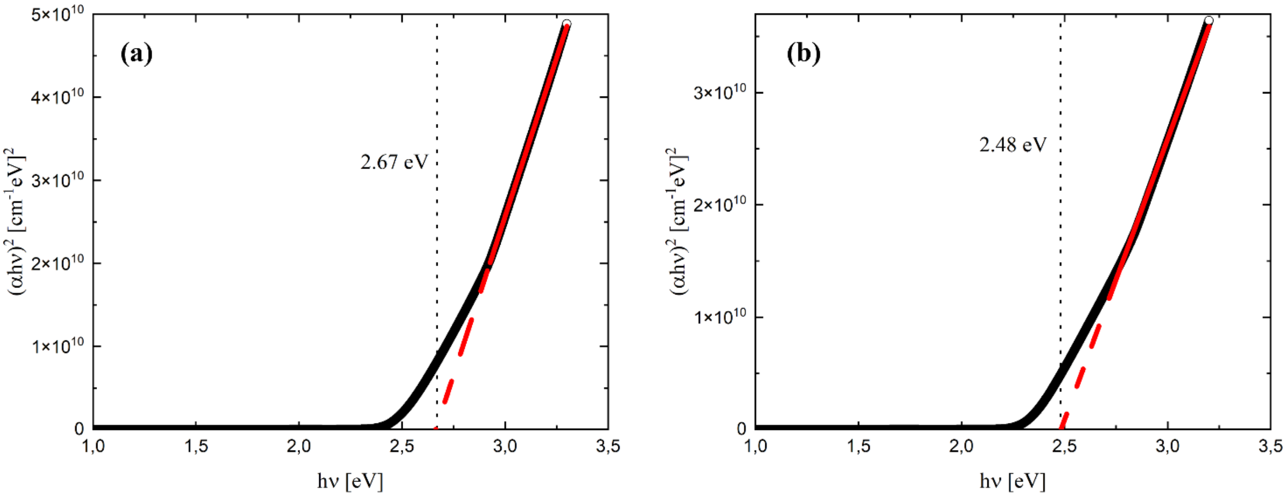

Figure 36. *Tauc plot of (a) ZnCdS and (b) CdS thin films on glass. Data processed based on UV-VIS spectroscopy measurements.*

A linear fit on the data represented in figure 36, allow us to determine an energy gap equal to $E_g = (2.67 \pm 0.01)\, eV$ and $E_g = (2.48 \pm 0.01)\, eV$ for ZnCdS and CdS respectively. Considering a tabulated energy gap of and E_g^{ZnS} = 3.6 eV for ZnS [133,134], we determined a Zn content of about (17 ± 2)%, assuming the validity of Vegard law. The thicknesses of these films were fine-tuned to minimize absorption of blue light, such as with E_g^{CdS} (2.42 eV), and to prevent, as much as possible, the formation of pinholes that could disrupt the behaviour of the p-n junction.

4.4 ANTIMONY SELENIDE

Antimony selenide serves as the absorber layer and must exhibit excellent crystalline quality and an appropriate grain size to minimize the number of crystalline defects and grain boundaries, which can adversely affect the device's performance. Consequently, the technique used for its growth is the CSS.

To achieve optimal growth conditions, a study was conducted by varying the partial pressure of argon in the growth chamber (from 0.01 mbar to 1 mbar), while maintaining a constant substrate temperature 360 °C and a constant deposition rate. To maintain a constant deposition rate at different Ar counterpressures, the crucible temperature was adjusted accordingly. In all cases, the antimony selenide was deposited on the preceding layers of the solar cell, specifically SLG/ITO+ZnO/CdS+ZnCdS.

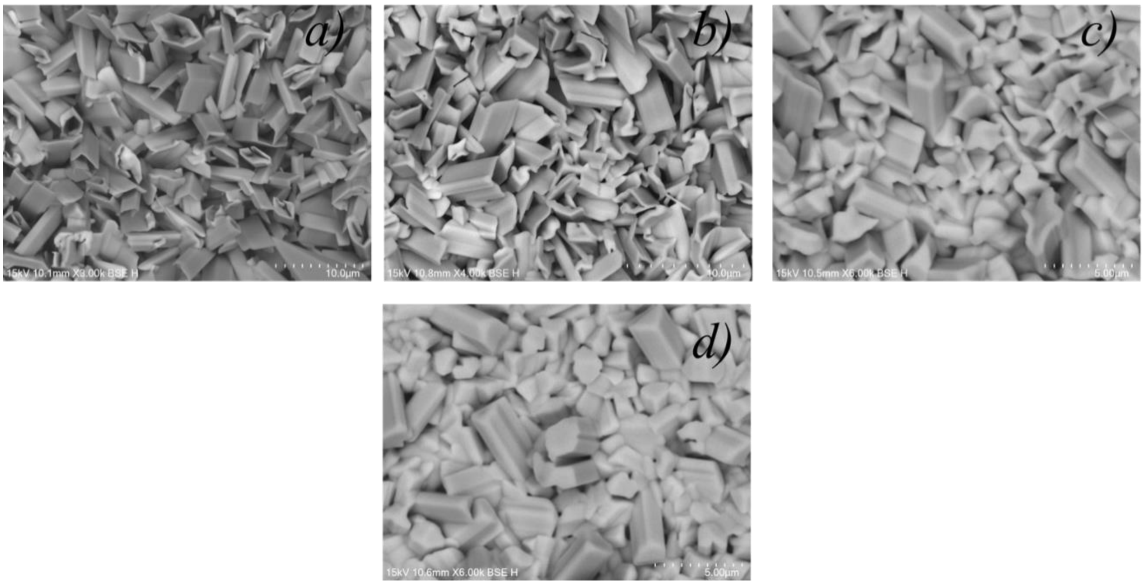

Figure 37. *SEM image of Sb_2Se_3 grown under different Ar counterpressure of a) 0.01 mbar, b) 0.1 mbar, c) 0.5 mbar and d) 1 mbar.*

In figures 37a, b, c, d display the SEM images of the Sb_2Se_3 surfaces how casing the effects of different Ar counterpressure during the growth of antimony selenide. The images indicate that morphology of the antimony selenide is significantly influenced by the amount of argon present in the chamber during growth. However, in all cases, the grain size is appropriate for photovoltaic purposes, ranging between 4 and 7 μm.

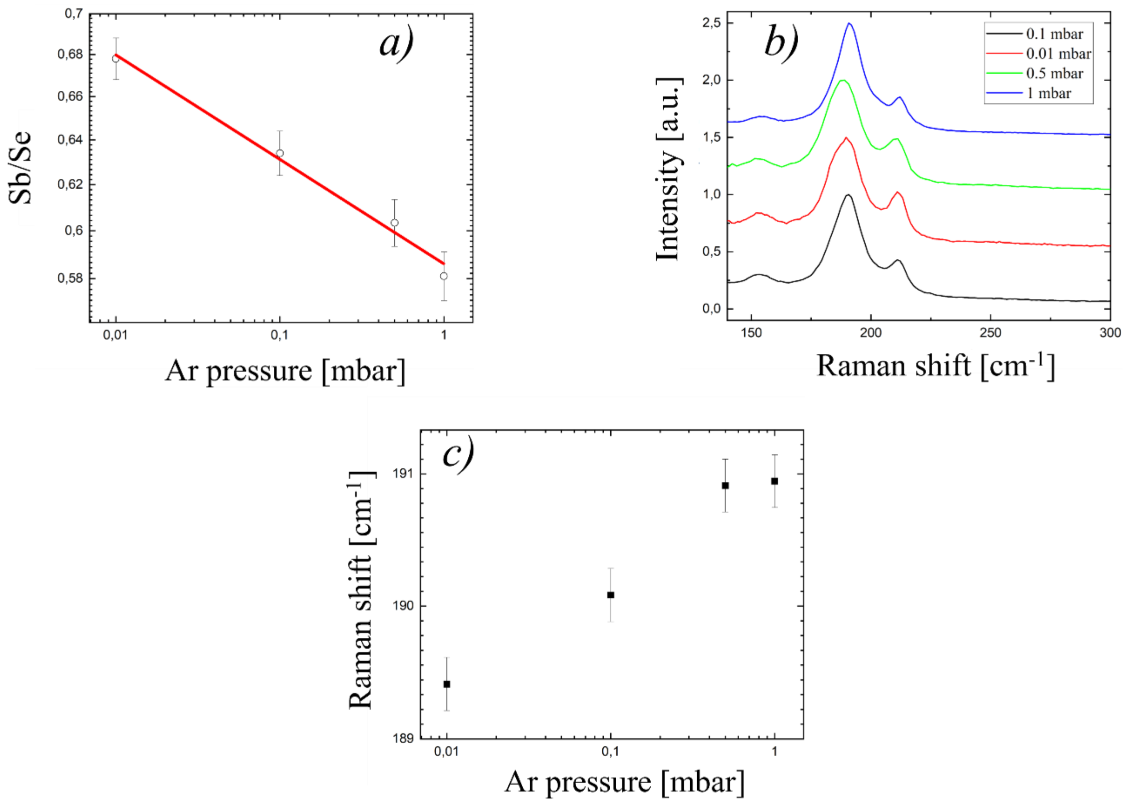

Figure 38. *a) ratio of atomic percentage (at%) between Sb and obtained from EDX measurements with the red line representing the linear fit; b) Raman spectra of antimony selenide under different Ar counterpressure during growth; c) The Raman shift of the principal peak as a function of Ar counterpressure.*

Additionally, different argon counterpressures enable control over the stoichiometry of the Sb_2Se_3 film, as shown in figure 38a. The Sb/Se ratio exhibits a linear trend on a log-log scale decreasing with increasing Ar pressure. At low counterpressures, the Sb_2Se_3 film shows an excess of antimony, while at higher Ar counterpressures, it becomes selenium-rich. These measurements were conducted using SEM with an EDX probe. Notably, Seebeck effect measurements reveal that even the antimony-rich film exhibits p-type conductivity, which can be attributed to the presence of excess metallic antimony within the Sb_2Se_3 crystalline lattice.

The Raman measurements, displayed in figure 38b, were performed using a 532 nm excitation laser. By comparing the experimental peaks with established data from the literature, we can identify the presence of a peak at 154.4 cm^{-1}, the main peak at 191.5 cm^{-1}, and another peak at 212.8 cm^{-1} [135]. Notably, the main peak is asymmetrical, resulting from the convolution of the peak at 184.7 cm^{-1} and the peak at 191.5 cm^{-1}.

Figure 38b illustrates various graphs demonstrating a shift in the Raman peak position. Following the deconvolution shown figure 38c, it is observed that the main peak shifts to higher Raman shift values as the Ar pressure increases. This result aligns with the EDX results, as a higher argon content enriches the Sb_2Se_3 film in Se, thereby enhancing its p-type conductivity. In fact, a rightward shift in the Raman signal towards higher values, indicates an increase in p-type doping [136]. In literature is reported that antimony selenide evaporates congruently, releasing Sb_4 and Se_2 molecules from the crucible, as demonstrated by thermodynamic calculations [137,138]. The experimental results reveal that when Sb_4 and Se_2 molecules reach the substrate, at temperature of 360 °C and a fixed deposition rate of about 8.3 nm/s, antimony evaporates more readily than selenium as the Ar pressure in the growth chamber increases. Conversely, by reducing the Ar pressure, the Sb/Se ratio approaches stoichiometry, ultimately resulting in a condition of Sb excess at an Ar pressure of around 10^{-2} mbar.

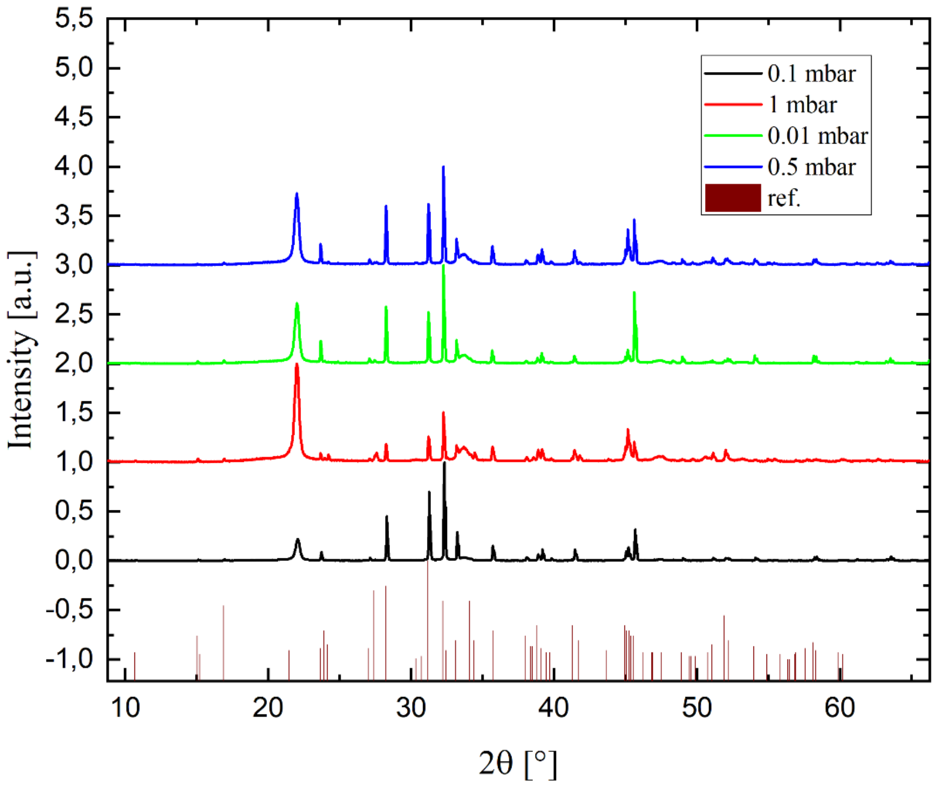

Figure 39. *XRD spectra of Sb_2Se_3 grown at different Ar counterpressures.*

The XRD measurements, shown in figure 39, were carried out to assess the impact of Ar pressure on the preferential growth plane of Sb_2Se_3 crystalline grains. The XRD graphs reveal a notably intense peak at a 2θ angle of 21.99°. This peak was not observed in our previous work [91], where antimony selenide was grown on the CdS+ZnCdS system. Therefore, it is reasonable to hypothesize arises from the contribution of the underlying layers beneath the Sb_2Se_3. To validate this hypothesis, a deconvolution operation was performed on this asymmetric peak using a Voigt profile, considering two distinct peaks. As illustrated in figure 40, the ratio between the cumulative curve (blue line) and the peak represented by the green curve remains nearly constant across all four samples, suggesting that it likely arises from the underlying layers on which Sb_2Se_3 has grown. On the other hand, the second peak, depicted by the red curve, shows significant variation among the different samples. When compared to the reference card JCPDS 15-0861, this peak is attributed to the (220) crystalline plane of antimony selenide. In all cases, the deconvolution process yielded an R^2 value of 0.999.

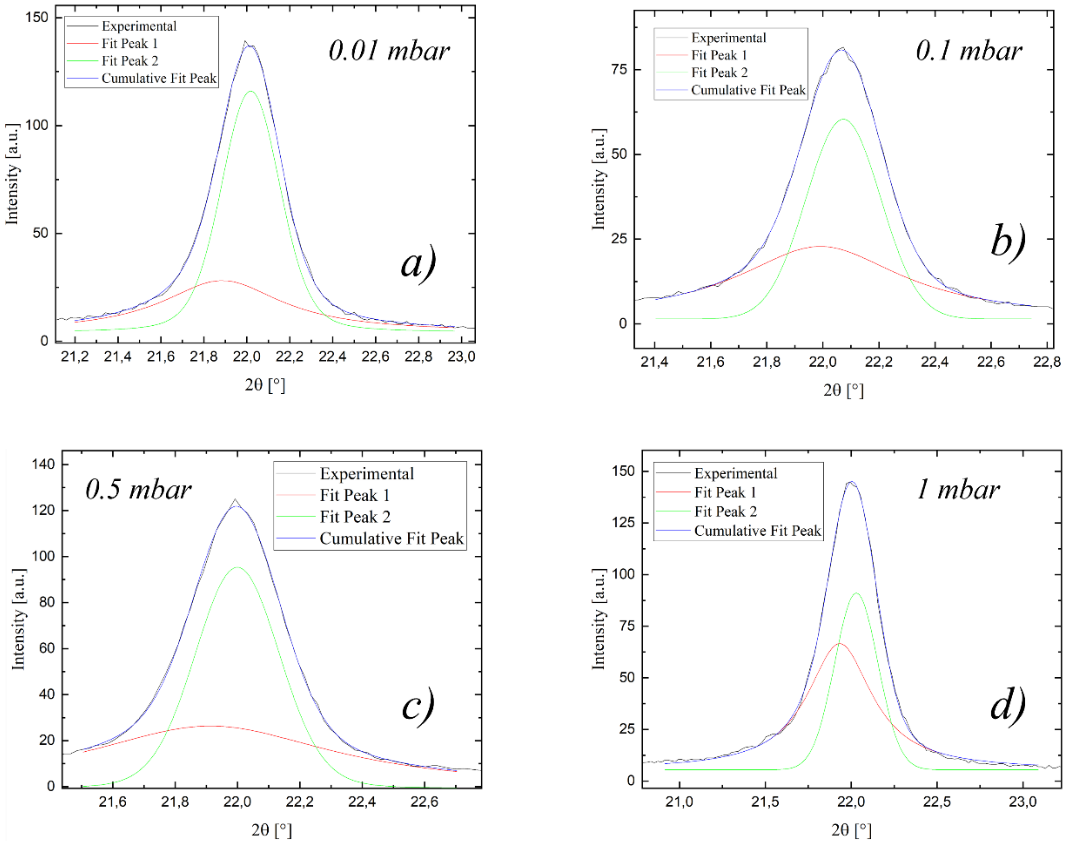

Figure 40. *Focus of the antimony selenide XRD spectra near the 21.99° peak. A deconvolution process is shown.*

To identify the predominant crystal plane relative to the others, a figure of merit, known as the texture coefficient (TC) can be defined [139]

$$TC_{hkl} = \frac{I_{hkl}/I_{0hkl}}{\sum_{i=1}^{n} I_{h_i k_i l_i}/I_{0h_i k_i l_i}} \cdot 100 \tag{4-4}$$

Here I_{hkl} represents the experimental peak intensity related to the selected plane, I_{0hkl} is the intensity of the same plane reported in the reference card and n is the total number of the selected crystalline planes.

This equation is well documented in [140] and assumes that the intensity of the diffraction peaks of a sample, when measured at a Bragg angle θ, is given by:$I_0 = \frac{AD}{2\mu}$

Where A represents the intensity of the incident beam, D is the intensity of the diffracted beam per unit of length and μ is X-ray absorption coefficient of the material. It is important to note that the intensity of I_0 is independent of the Bragg angle. The quantity D can be expressed as a product of three factors:

$$D = F^2(hkl)p(\alpha,\beta,\gamma)\frac{(\delta\theta)^2}{4} \tag{4-5}$$

Where $p(\alpha,\beta,\gamma)$ denotes the total volume fraction of the sample oriented along a specific $\delta\theta$ angle and $F^2(hkl)$ is the structure factor that represents the discrepancy between the theoretical crystallographic model and the experimental results obtained from XRD measurements.

Thus, the quantity I_0 (for a specific hkl plane) can be rewritten, incorporating a parameter B that accounts for any imperfections of the crystalline structure and remains constant for each peak corresponding to the same sample, as follows:

$$I_0 = \frac{AB}{2\mu}p(\alpha,\beta,\gamma)\frac{(\delta\theta)^2}{4}F^2(hkl) \tag{4-6}$$

Considering the $\frac{AB}{2\mu}$ quantity as a constant, we can define a parameter C. For a thin film with randomly oriented grains, the intensity is given by:

$$I'(hkl) = C'F^2(hkl) \tag{4-7}$$

The intensity ratio between a sample with grains exhibiting preferential orientation and one with randomly oriented grains is found to be:

$$\frac{I(hkl)}{I'\ (hkl)} = \frac{C}{C'}p(\alpha,\beta,\gamma) \tag{4-8}$$

Furthermore, the ratio between the constants C and C′ can be neglected under the assumption that the sum of $p(\alpha,\beta,\gamma)$ over all orientations equals one. Consequently, the ratio of the sum of intensities for a specific number of reflections from oriented and random samples is exactly equal to C/C′. Thus, we exactly obtain the formula for the texture coefficient:

$$p(\alpha,\beta,\gamma) = \frac{I(hkl)}{\sum I(hkl)} \cdot \frac{\sum I'\ (hkl)}{I'\ (hkl)} \tag{4-9}$$

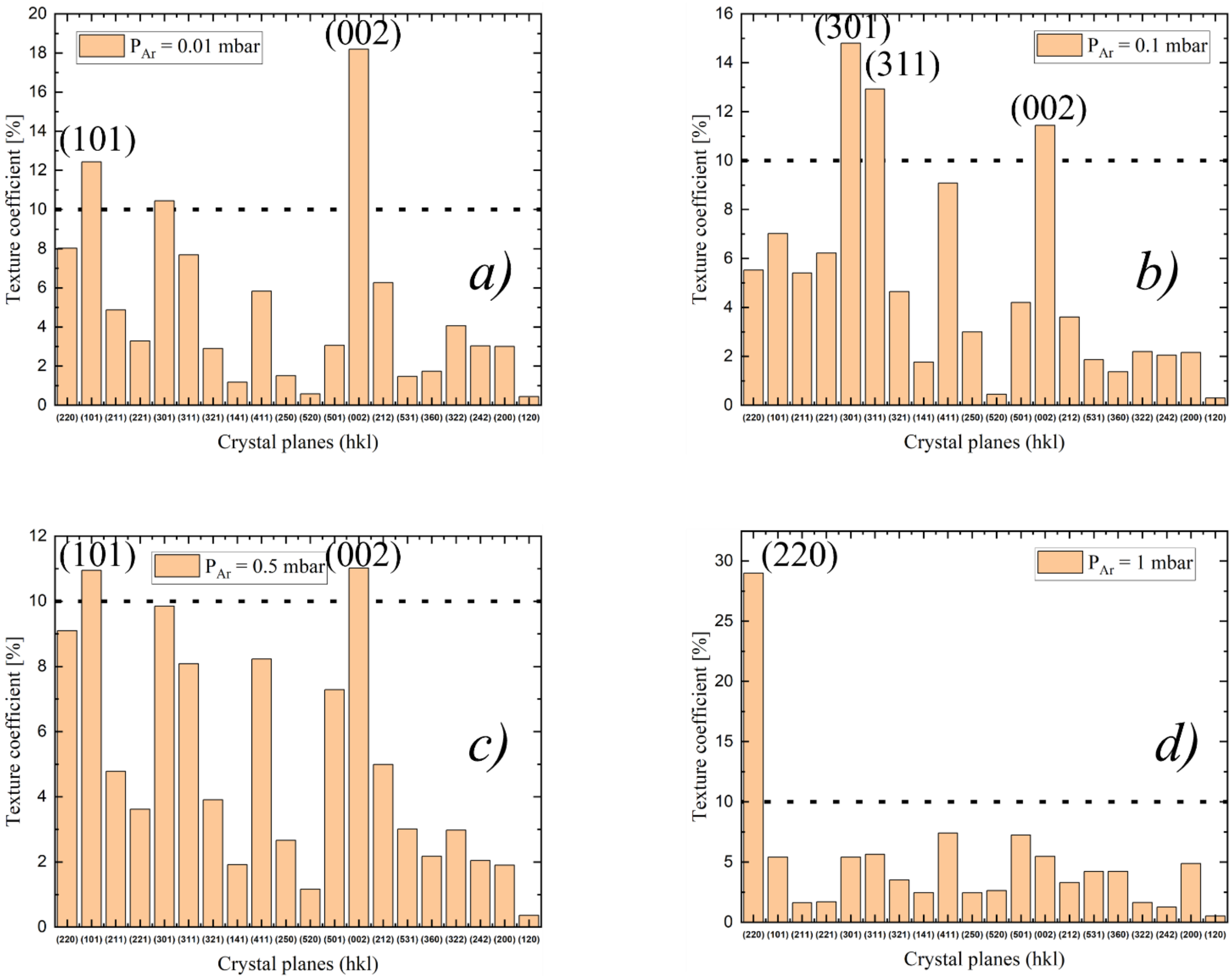

__Figure 41.__ TC evaluation of the XRD patterns for the Sb$_2$Se$_3$ films growth under different Ar counterpressures: a) 0.01 mbar, b) 0.1 mbar, c) 0.5 mbar, d) 1 mbar.

In figures 41a, b, c, and d, the results of the texture coefficient calculation are shown, with a minimum threshold of 10% used to classify a crystallographic plane as non-negligible. At low Ar pressures, the preferential growth plane is the (002) plane, which corresponds to the

[001] direction, which is favourable for charge transport within a single ribbon. At an argon pressure of 0.1 mbar, the (002) plane continues to be the preferential plane, alongside the (hk1) planes. As the argon pressure increases, the Sb_2Se_3 grains exhibit a tendency to orient more randomly particularly at 0.5 mbar. This trend culminates at 1 mbar, where the only preferential crystallographic plane is the (220) plane. The (hk0) planes, which grow perpendicular to the ribbon axis, impede efficient charge transport, since photogenerated charges must traverse two adjacent ribbons, connected by weak van der Waals bonds. Consequently, the transport mechanism becomes hopping-like.

In conclusion the optimal condition for growing antimony selenide is to introduce an Ar counterpressure of 0.1 mbar in the deposition chamber. This setting facilitates the growth of a nearly stoichiometric with grains oriented perpendicular to the substrate.

4.4.1 ***Deep levels in antimony selenide***

To detect and characterize the deep levels of the Sb_2Se_3 in the depletion region admittance spectroscopy measurement were performed under both dark and illumination conditions varying the temperature in the range between 193 K and 353 K 20 K steps.

In general, to experimentally determine the characteristics of a deep level, it is essential to alter the occupancy state and observe the variation of an appropriate physical quantity over time. A space charge region is characterized by curved band profiles, allowing the deep center level to intersected the Fermi level. This intersection enables the alteration of the occupancy state of the center by applying an external electric field. Specifically, admittance is a complex quantity, expressed as: $Y = G + iS$, where the real part G represents conductance, and the imaginary part S represents susceptance. If $S > 0$, the system exhibits capacitive behaviour, which can be expressed as $C = S/\omega$, where ω is the angular frequency of the applied voltage. Each variation in the reverse voltage δV_R corresponds to a change in the space charge $\delta\varrho(x)$, and these two variations are related through the expression:

$$\epsilon\delta V_R = \int_0^\infty x\delta\rho(x)dx \qquad (4\text{-}10)$$

In this equation, the left-hand side represents the product of permittivity ϵ and the variation in reverse voltage δV_R. The integral on the right-hand side quantifies the variation of the center of mass of the space charge. In particular, a variation δV_R induces a change in the space charge near the edge of the depletion region (W) as well as a variation due to the position $\bar{x}$, where the trap occupancy level intersects with the quasi-Fermi level F_e. this intersection locally results in a change in the charge state of the trap.

Thus, the previous integral can be rewritten as follows:

$$\epsilon \delta V_R = \int_0^{\infty} x \delta \rho_T(x) dx + \int_0^{\infty} x \delta \rho_W(x) dx \tag{4-11}$$

In this expression, the first integral accounts for the variation in the charge due to the traps (δϱT(x)), while the second integral represents the variation in the charge at the depletion region edge (δϱW(x)). In admittance measurement, the reverse voltage oscillates with small-amplitude sinusoidal variations, so $\delta \rho_W(x)$ to be non-zero only near x = W. Similarly, $\delta \rho_T(x)$ is non-zero only in the vicinity of $\bar{x}$.

The two previous integrals can be approximated as follows:

$$\int_0^{\infty} x \delta \rho_T(x) dx \sim \bar{x} \int_0^{\infty} \delta \rho_T(x) dx = \bar{x} \delta Q_T \tag{4-12}$$

And

$$\int_0^{\infty} x \delta \rho_W(x) dx \sim W \int_0^{\infty} \delta \rho_W(x) dx = W \delta Q_W \tag{4-13}$$

where δQ_T and δQ_W have the dimensions of charge per unit area.

In this way, the integral became:

$$\epsilon \delta V_R = \bar{x} \delta Q_T + W \delta Q_W \tag{4-14}$$

The temporal evolution of the charge δQ_T can be expressed as:

$$\frac{\partial \delta Q_T}{\partial t} = -\widetilde{\omega} \delta Q_T + g \delta V_R \tag{4-15}$$

Here $-\widetilde{\omega} \delta Q_T$ represents the exponential relaxation of the charge when δV_R is set to zero, and $g \delta V_R$ is proportional to the perturbation of the reverse voltage. The frequency $\widetilde{\omega}$ is the inverse of the characteristic relaxation time, which varies for each individual trap.

The proportionality constant g is defined as:

$$g = \widetilde{\omega} \left(\frac{\delta Q_T}{\delta V_R} \right)_0 \tag{4-16}$$

The admittance for unit of area is given by:

$$Y = \frac{1}{\delta V_R} \left(\frac{\partial \delta Q_T}{\partial t} + \frac{\partial \delta Q_W}{\partial t} \right) \tag{4-17}$$

By solving the differential equation for δQ_T with the sinusoidal perturbation $\delta V_R = (\delta V_R)_0 \exp(i\omega t)$, and making the appropriate substitutions while separating the real imaginary parts, one obtains:

$$Y = G + iS = \frac{\omega^2 g}{\tilde{\omega}^2+\omega^2}\left(1 - \frac{\bar{x}}{W}\right) + i\omega\left\{\frac{\epsilon}{W} + \frac{g\tilde{\omega}}{\tilde{\omega}^2+\omega^2}\left(1 - \frac{\bar{x}}{W}\right)\right\} \tag{4-18}$$

In the low frequency limit ($\omega \ll \tilde{\omega}$), the capacitance becomes:

$$C(0) = \frac{\epsilon}{W} + \frac{g}{\tilde{\omega}}\left(1 - \frac{\bar{x}}{W}\right) \tag{4-19}$$

While in the high frequency limit ($\omega \gg \tilde{\omega}$) it simplifies to:

$$C(\infty) = \frac{\epsilon}{W} \tag{4-20}$$

Note that $C(\infty)$ represents the capacitance of the depletion region.

In conclusion, the capacitance and conductance are given by the following expressions:

$$C(\omega) = \frac{C(0)-C(\infty)}{1+(\omega/\tilde{\omega})^2} + C(\infty); \quad \frac{G(\omega)}{\omega} = \frac{[C(0)-C(\infty)]\cdot(\omega/\tilde{\omega})}{1+(\omega/\tilde{\omega})^2} \tag{4-21}$$

As shown in Figure 42, at the frequency $\tilde{\omega}$, the ratio $\frac{G(\omega)}{\omega}$ reaches a maximum value of $\frac{C(0)-C(\infty)}{2}$, while the capacitance shows a step-like behavior at $\tilde{\omega}$.

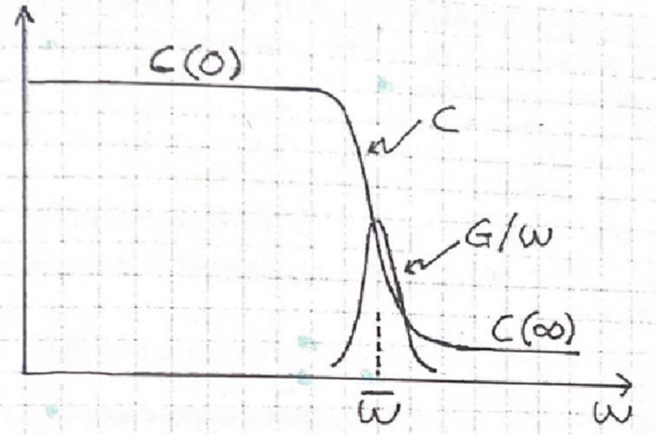

Figure 42. *Qualitative trends of the functions C(ω) and $\frac{G(\omega)}{\omega}$. The image is taken from [141].*

The qualitative trends of the functions $C(\omega)$ and $G(\omega)/\omega$ are as follows:

1. Capacitance $C(\omega)$: As the frequency ω increases from low to high, the capacitance $C(\omega)$ transitions from its low-frequency value $C(0)$ to its high-frequency value $C(\infty)$. This transition occurs in a step-like manner, with a noticeable change around the characteristic frequency $\widetilde{\omega}$. At low frequencies ($\omega \ll \widetilde{\omega}$), the capacitance is close to $C(0)$, while at high frequencies ($\omega \gg \widetilde{\omega}$), it approaches $C(\infty)$, which corresponds to the depletion capacitance.
2. Conductance-to-frequency ratio $\frac{G(\omega)}{\omega}$: The ratio $\frac{G(\omega)}{\omega}$ shows a distinct peak at the frequency $\widetilde{\omega}$. At $\omega = \widetilde{\omega}$, $\frac{G(\omega)}{\omega}$ reaches a maximum value of $\frac{C(0)-C(\infty)}{2}$. For frequencies lower than $\widetilde{\omega}$, the conductance increases, while for frequencies higher than $\widetilde{\omega}$, it decreases.

These behaviors reflect the dynamic response of the system, with the characteristic frequency $\widetilde{\omega}$ marking the point where both the capacitance and conductance exhibit significant changes. In our specific case, the C-ω characteristics under both light and dark conditions, as depicted in Figures 43a and 43b, exhibit an inflection point in the capacitance at high frequencies and elevated temperatures. This inflection point is a clear indication of the presence of deep traps as described in reference [142].

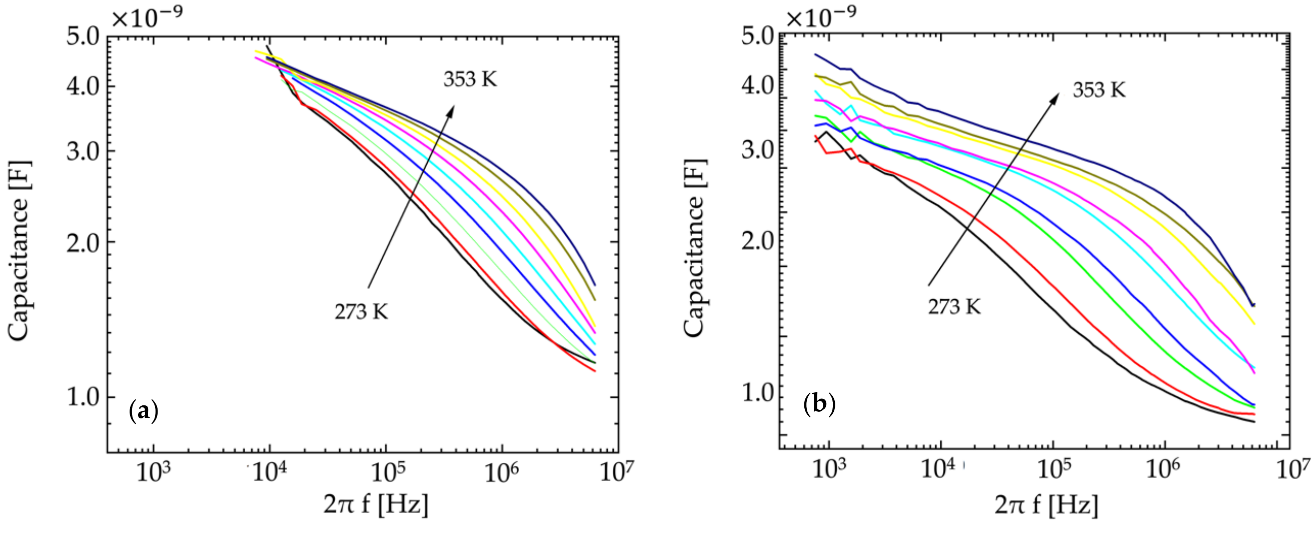

Figure 43. *Admittance spectroscopy measurements carried out under two different conditions: a) under light and b) in dark.*

After identifying the frequency $\widetilde{\omega}$ at which the inflection point occurs, the activation energy of the deep levels can be calculated using the following relationship [143]:

$$\frac{\widetilde{\omega}}{T^2} = 2\xi_0 \exp\left(-\frac{E_a}{KT}\right) \tag{4-22}$$

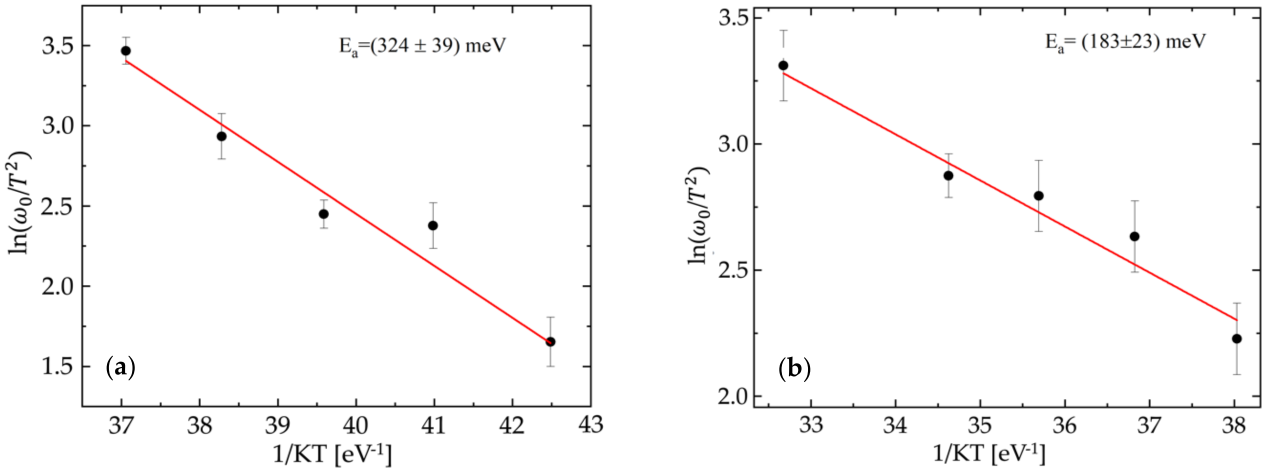

Figure 44. *Plot of* $ln(\omega_0/T^2)$ *(unit:* $s^{-1} \cdot K^{-2}$*) versus 1/KT, showing two distinct activation energies observed under (a) light and (b) dark conditions.*

As shown in figure 44a, b, two deep levels are detected at (324 ± 39) meV and (183 ± 23) meV under light and dark condition respectively. It is important to note that these values are estimates, as the C-ω curves were obtained using relatively large D-factor values. Consequently, this method does not allow for the precise determination of the trap locations, whether in the p-type or n-type regions. Nevertheless, based on the curves in Figures 43-44, we can infer that these energies represent the boundaries of a narrow energy band corresponding to a trap distribution. This conclusion is further supported by the absence of a distinct inflection point in each curve, as the gradual decrease in capacitance suggests the overlapping influence of multiple trap levels close in energy. The presence of this trap band may explain the detection of two different energy levels under dark and illuminated conditions (Figure 44). This phenomenon could be attributed to the band bending at the intermixing layer between ZnCdS and Sb_2Se_3. Due to the extended trap levels and the variable Fermi and quasi-Fermi levels in both dark and illuminated conditions, only specific energy-related fractions of the traps will be occupied. According to the literature [81] several energy levels have been identified within the Sb_2Se_3 energy gap, most of which are classified as deep donors, with only a few recognized as acceptor-like defects. Among these, the antimony vacancy (V_{Sb}) corresponds to an energy level located 180 meV above the valence band edge [81,144], aligning with the lower boundary of the trap band detected by admittance measurements (Figs. 43-44). If the V_{Sb} [81,144] defect is indeed responsible for trapping, then the trap band is likely localized within the Sb_2Se_3 layer.

4.5 BACK-CONTACT

A good contact must meet two key requirements: it must be ohmic and exhibit low resistivity. A contact is considered ohmic when its current-voltage characteristic (I-V) is linear and symmetrical over a range of potential values V centered at the origin of the axis. For a p-type semiconductor the general rule is that the work function of the metal contact (ϕ_M), defined as the energy difference between the Fermi level and the vacuum level, must be greater than or equal to the electron affinity of the semiconductor (χ_{sc}), which is the difference between the Fermi level close to the band edges of the (doped) semiconductor and the vacuum level. If this rule is not respected, a Schottky barrier is formed, creating a potential difference that impedes the extraction of holes, thus failing the requirement for an ohmic contact (figure 45). Generally, p-type semiconductors have high electron affinity, making it difficult to form ohmic contacts with conventional metals. In particular, the electron affinity of antimony selenide is approximately 4 eV [57], and only rare or expensive metals such as gold, platinum, or iridium are capable of establishing ohmic contacts.

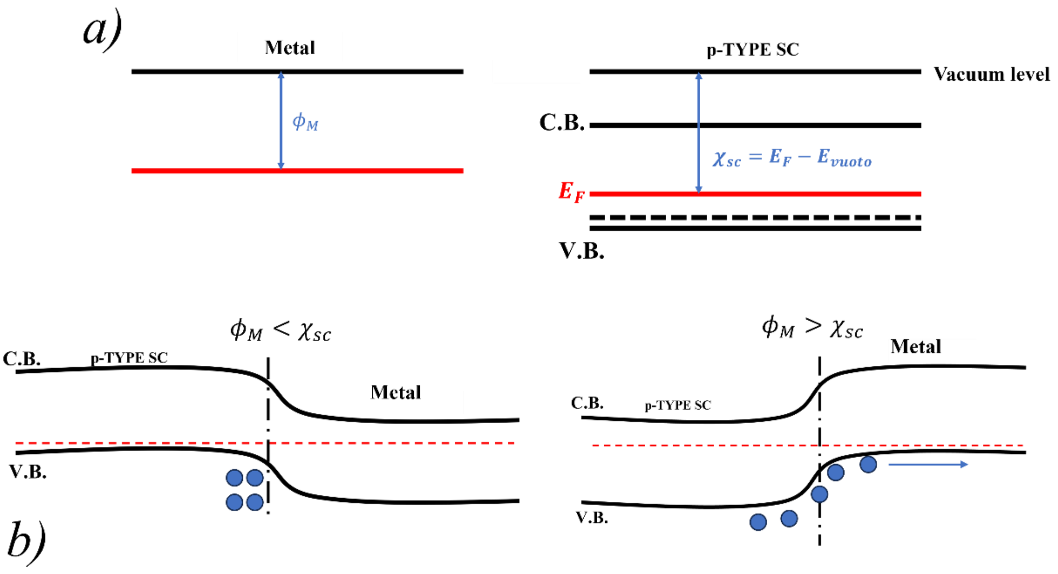

Figure 45. *Band diagram of p-type semiconductor and metal a) before contact formation; b) after contact formation highlighting the two possible situations.*

Metals such as molybdenum or nickel-vanadium alloys are commonly used, along with a thin layer of heavily doped semiconductor with a low energy gap, placed between the metal and the absorber semiconductor. Although a Schottky barrier forms at the metal-semiconductor interface, the presence of this layer, ensures a narrow depletion region at the semiconductor side. This narrow depletion region allows free charge carriers to pass through the barrier via the tunnelling effect, facilitating their extraction at the contact. As a result, the configuration produces a linear current-voltage characteristic, satisfying the requirements for ohmic contact.

In this study a novel back-contact structure for Sb_2Se_3-based solar cell, consisting of amorphous magnetite and troilite, named Fe-S-O, is proposed. This 200 nm thick layer is deposited on the Sb_2Se_3 film by RF magnetron sputtering at room temperature. The deposition process occurs under an Ar pressure of 0.5 Pa, with a power density of 3.3 W/cm^2.

4.5.1 Composition and morphology of Fe-S-O layer

Scanning electron microscopy (SEM) measurements were carried out on different areas of the sample growth on glass, to evaluate the thin film uniformity. The SEM image (figure 46) reveals a characteristic structure of amorphous material exhibiting a uniform and flat morphology.

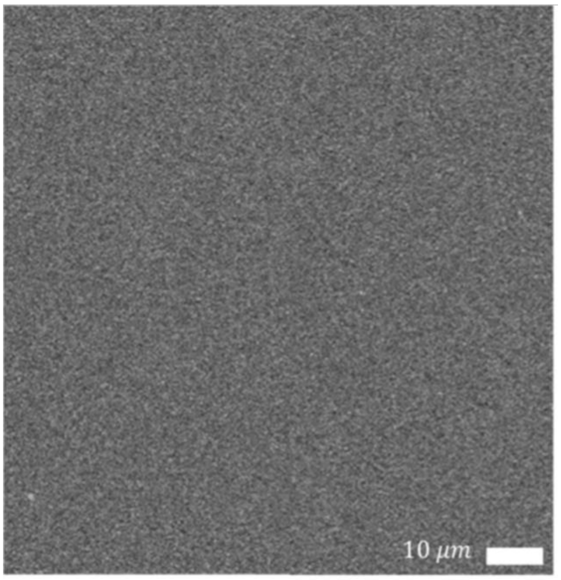

Figure 46. *SEM image of the amorphous Fe-S-O structure. The film is deposited on SLG at RT [100].*

Compositionally, Energy-Dispersive X-ray (EDX) measurements indicate that the layer is composed mainly of oxygen, sulphur and iron, as reported in the spectrum shown in figure 47.

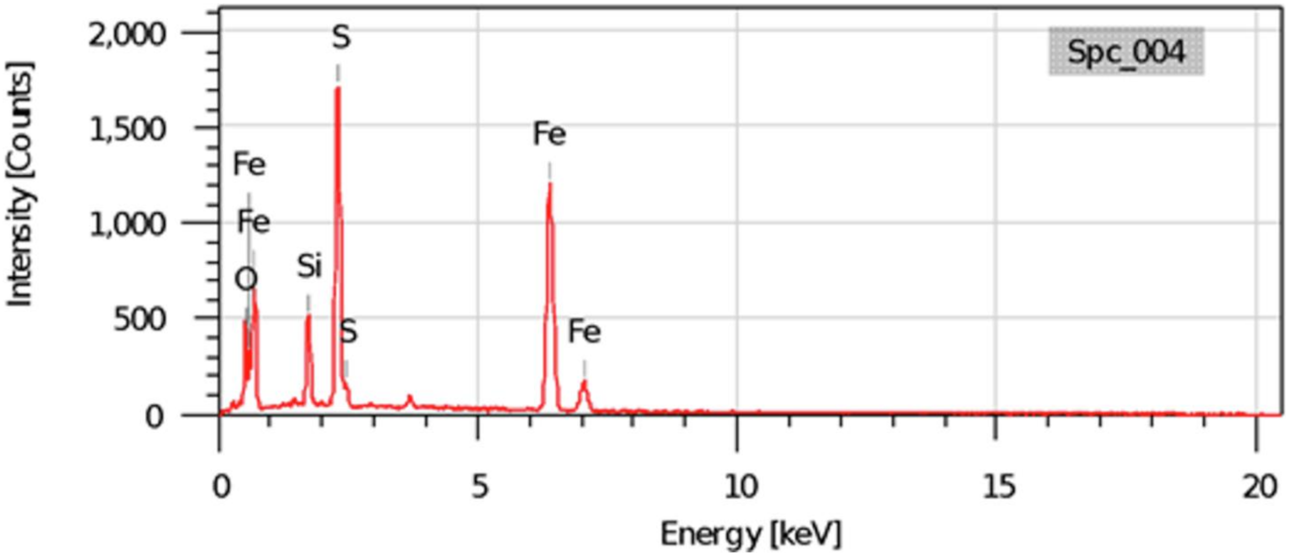

Figure 47. *EDX spectrum of the Fe-S-O film [100].*

The silicon peak, originating from the SLG substrate, is also present. Due to the high electron beam acceleration voltage (20 keV), the substrate is also affected. The EDX spectrum was acquired from different areas of the sample, and the average values of atomic composition are reported in table 4.

Table 4. *EDX analysis of the Fe-S-O film, related to the figure 45.*

Chemical element	Average at%
silicon	8 ± 1
iron	40 ± 1
oxygen	22 ± 1
sulphur	30 ± 1

By studying the XRD patterns, various crystalline structures were observed in the sputtered thin films deposited at both low and high temperatures. The XRD profile of a film deposited at RT (Figure 49a) indicates an amorphous structure. Raman spectroscopy performed on the same film in air (Figure 48a) indicates peaks at 655 cm^{-1} and 525 cm^{-1} corresponding to magnetite (Fe_3O_4), while peaks at 401 cm^{-1} and 290 cm^{-1} correspond to the distinctive Raman signals of hematite (Fe_2O_3) [145,146]. However, repeating the Raman measurement using a gas-tight sample holder under an Ar atmosphere (Figure 48b) fails to identify any previously observed peaks, consistent with the behaviour of amorphous compounds. The disparity between spectra collected in air and under Ar atmosphere can be explained as follows:

- in air, the combined effect of laser-induced heating and oxidation triggers crystallization of the film [147];
- in Ar atmosphere, the film remains unchanged due to the absence of reactive oxygen, resulting in a noisy spectrum characteristic of an amorphous structure. Moreover, the defocusing of the laser beam passing through the Polystyrene window of the gas-tight sample holder attenuates its power, thereby failing to induce film crystallization.

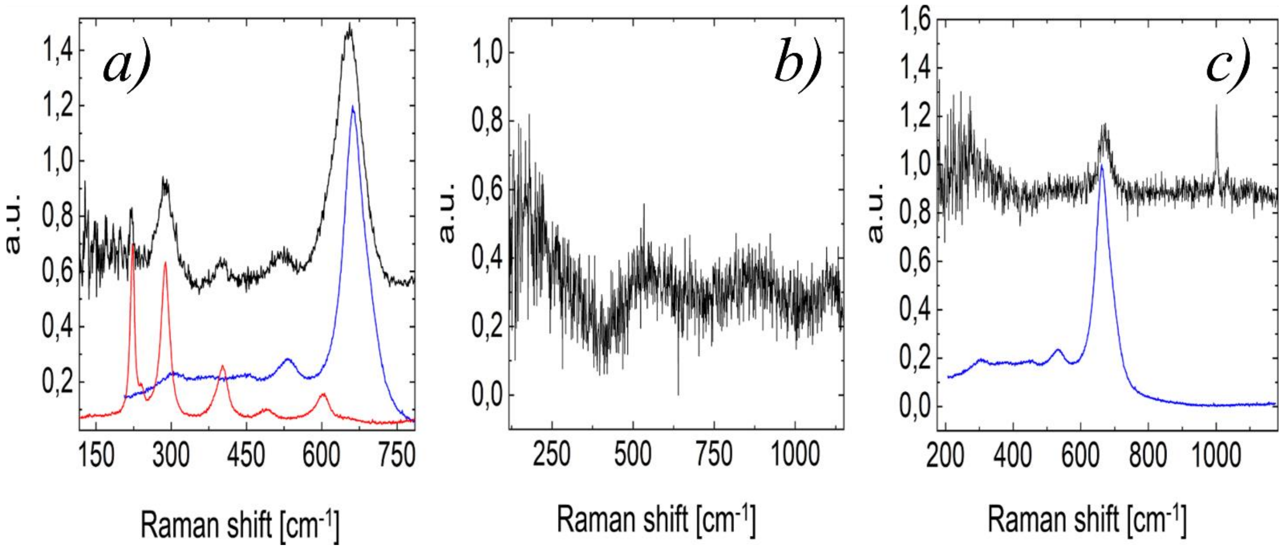

Figure 48. *(a) The Raman spectrum performed with the sample in air is depicted in black, with the references to hematite and magnetite minerals highlighted in red and blue respectively. (b) The Raman spectrum of the same sample taken under an Argon atmosphere. (c) Raman spectrum of the sample deposited at 520°C measured in an Argon atmosphere with the magnetite reference highlighted in blue; the peak at 1001 cm^{-1} is related to Polystyrene [100].*

In contrast, the XRD spectrum of a film deposited at high temperature (520 °C) (Figure 49b) exhibits peaks corresponding to two crystalline compounds: Fe_3O_4 in both cubic (JCPDS-00–065-0731) and orthorhombic (JCPDS-04–007-1061) structures, and hexagonal $Fe_{(1-x)}S$ (JCPDS-00–037-0477). Raman measurements performed under Ar atmosphere reveal peaks at 661 cm^{-1} and 1001 cm^{-1}, corresponding to magnetite and Polystyrene, respectively (Figure 48c). However, the Raman spectrum is weak and noisy, significantly different from the pattern observed in Fig. 48b, attributed to the lower excitation power of the laser in the controlled atmosphere setup. It's noteworthy that detecting Raman peaks of hexagonal $Fe_{(1-x)}S$ is challenging even in pure samples [148]. Although Raman and XRD measurements fail to identify the $Fe_{(1-x)}S$ phase in amorphous films, EDX measurements suggest the presence of iron sulfide, which is corroborated by XRD patterns of the crystalline TFs grown at high temperature, which exhibit peaks indicative of the $Fe_{(1-x)}S$ phase.

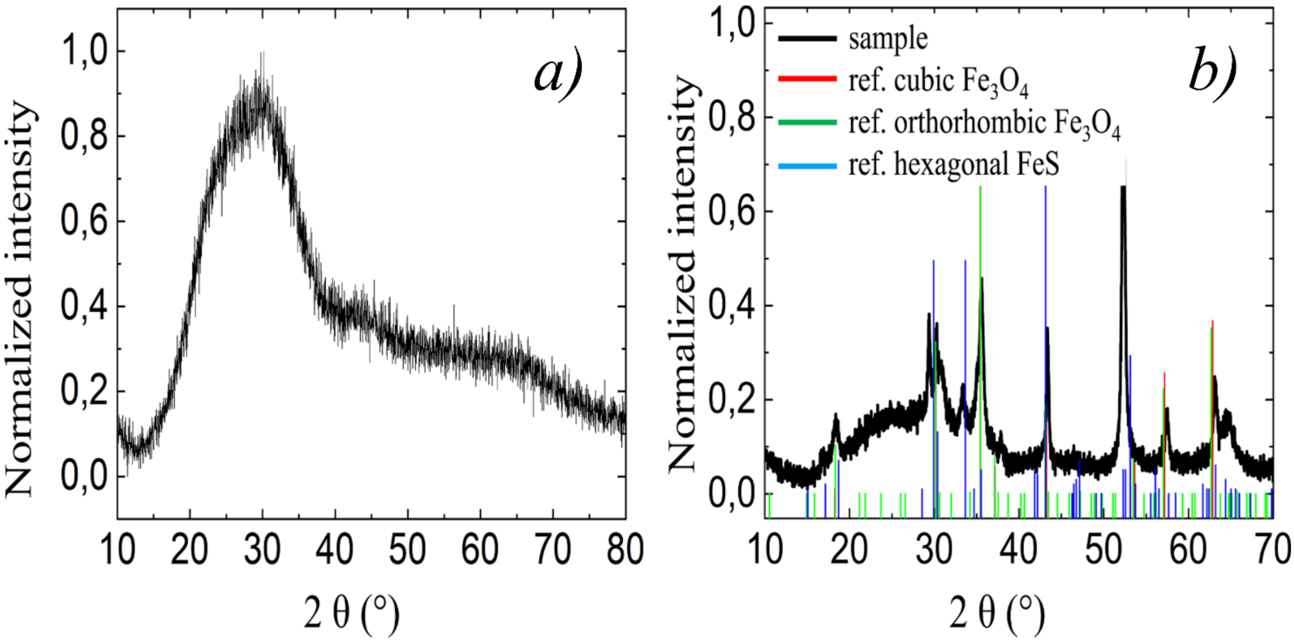

Figure 49. *(a) XRD pattern illustrating the amorphous nature of the* Fe_3O_4 *+ FeS film deposited via RF sputtering at room temperature (RT). (b) XRD pattern demonstrating preferential orientations of cubic and orthorhombic* Fe_3O_4 *and hexagonal FeS associated with a film deposited by RF sputtering at a substrate temperature of 520°C [100].*

4.5.2 Electrical measurements

The Fe-S-O thin film was investigated by Seebeck effect measurements. A temperature gradient was applied between the two Au metal contacts, determining the direction of the electric potential based on the predominant charge carriers. In cases where electrical conduction is predominantly governed by holes, the hotter contact exhibits a negative sign, whereas it assumes the opposite polarity when electrons are the majority carriers. This measurement revealed the p-type characteristics of the Fe-S-O films [149].

Measurement resistivity under dark conditions, using the van der Pauw method with gold contacts in a temperature range from 4 K to 600 K, allowed us to identify (figure 50) two different linear trends at high temperature: these trends corresponds to two acceptor levels with activation energy of 0.12 eV and 0.04 eV, as evidenced by the Arrhenius plot:

$$\rho(T) = \rho_0 \exp\left(\frac{E_a}{KT}\right) \tag{4-23}$$

Here E_a is the activation energy required for charges to transit from the energy state inside the energy gap to the conduction band (trap level), K is the Boltzmann constant, and T is the absolute temperature.

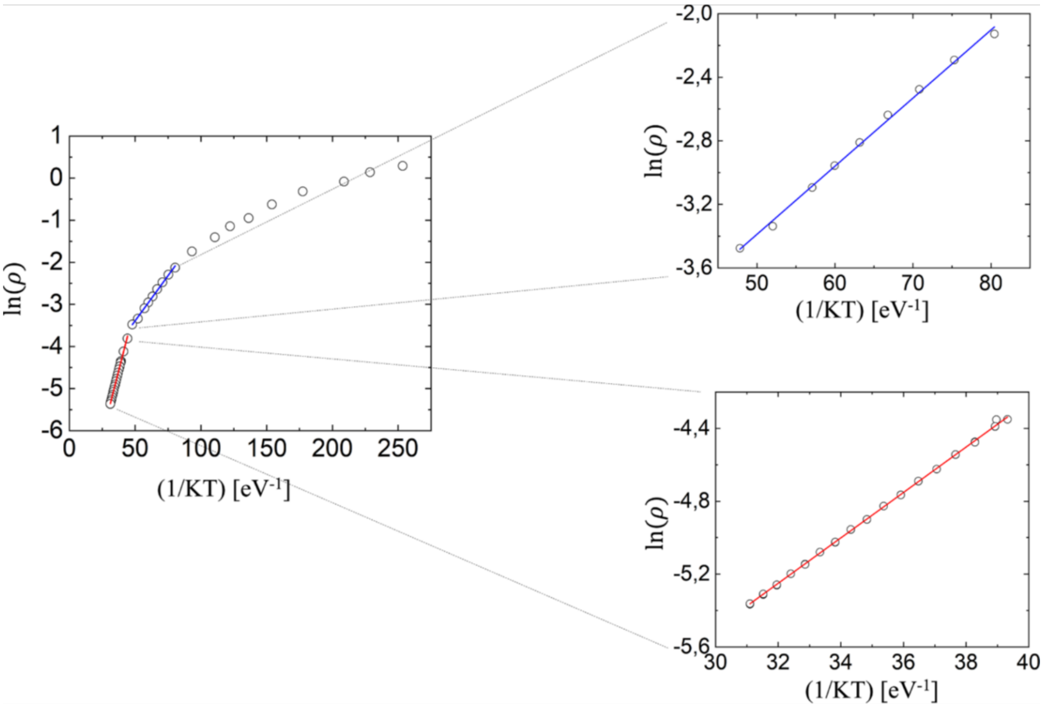

Figure 50. *Arrhenius plot of natural logarithm of resistivity, expressed in Ωcm, vs 1/KT.*

As reported in figure 51, transmission line method (TLM) contact geometry was implemented on the top of the Sb_2Se_3 layer to evaluate the ohmic behaviour of the Fe-S-O+Au contact [100].

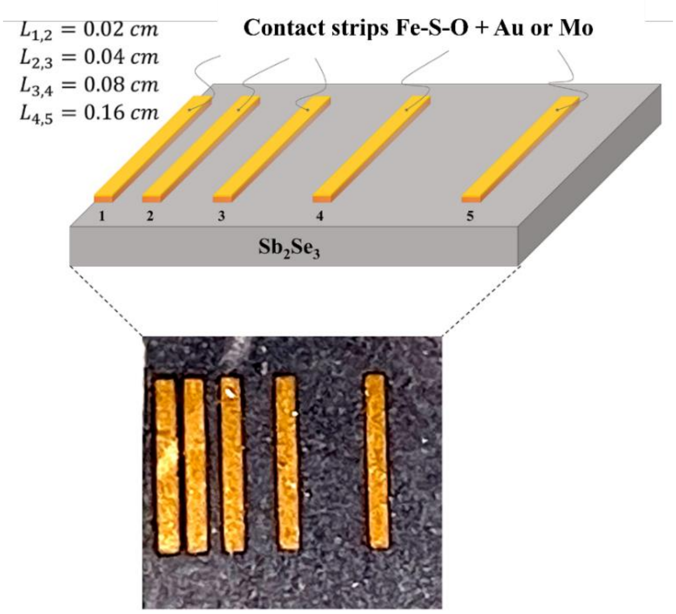

Figure 51. *Here's the contact pattern for IV measurements, with the sequence numbers of the contact pads [100].*

The I-V characteristic for each pair of contacts (as shown in figure 52a), measured under dark condition, exhibit a linear trend, indicative of the ohmic behaviour of the Sb_2Se_3/(Fe-S-O + Au) system. Notably, the resistance, calculated as the inverse of the slopes of the I-V curves, increases in accordance with the distances between the pads, aligning with our expectations.

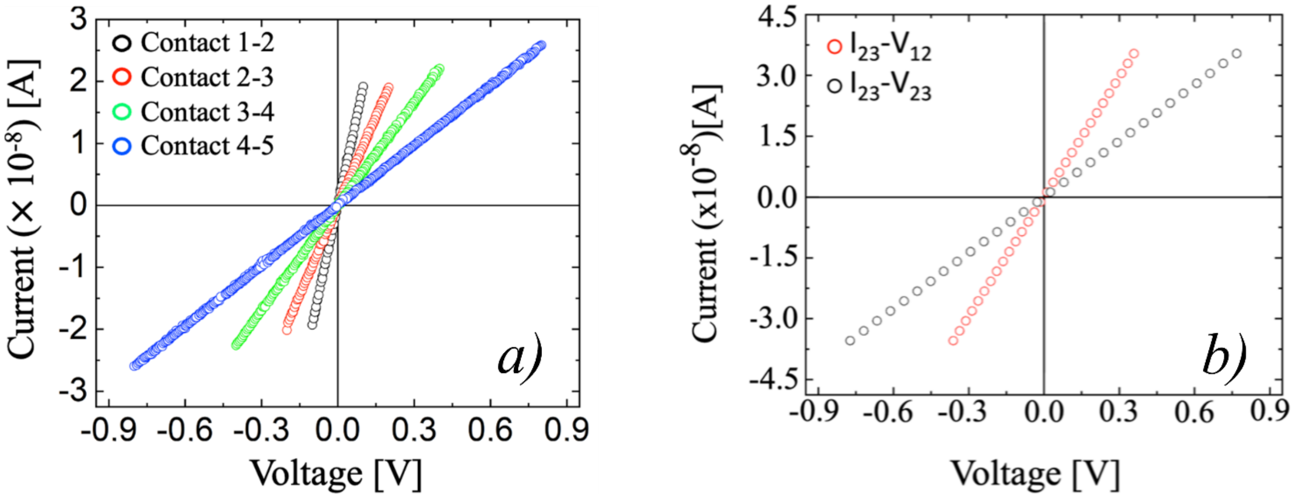

Figure 52. *a) The current-voltage characteristics under dark conditions vary with the distance between the contact pairs, as depicted in Figure 50. b) The current-voltage characteristic involves injecting current between contacts 2 and 3 while measuring the potential between them (indicated by black dots). Additionally, current is consistently injected between contacts 2 and 3 while measuring the potential between contacts 1 and 2 (depicted by red dots) [100].*

A more accurate method for determining the specific resistivity of the contacts, as an alternative to the traditional TLM approach, employs a three-terminal TLM configuration [150]. This method focuses exclusively on the first three contact pads of the geometry illustrated in Figure 51, and offers insights into the dark resistivity of Sb_2Se_3 in the direction parallel to the substrate. Initially, current is injected into the 2–3 contact pair, and the resulting voltage is recorded. Next, current is injected into the 2–3 contacts, while the voltage between the 1–2 contacts is measured. In this method, we denote the semiconductor resistance as R_{sc}, the specific contact resistivity as ρ_c, the distance between the pads as d and the contact length as w. We define the in-resistance $R_i = \frac{V_{23}}{I_{23}} = cotgh(\alpha_0 d)$ and the end-resistance $R_e = \frac{V_{12}}{I_{23}} = \frac{z_0}{\sinh(\alpha_0 d)}$, where $\alpha_0 = \sqrt{R_{sc}/\rho_c}$ and $z_0 = \frac{1}{w}\sqrt{R_{sc}\rho_c}$ [151,152]. The values of R_i and R_e were determined through a linear fit of the data presented in figure 52b, using the inverse of the slope coefficient. By combining the equations for R_i and R_e, we can extract the resistivity of antimony selenide, yielding a result of $(3.05 \pm 0.18) \cdot 10^5$ Ωcm.

When working with polycrystalline thin films, it is crucial to approach experimental results with cautions. Grain boundaries can significantly affect current flow, potentially hindering charge transport due to traps or recombination centers. In our specific scenario, this concern is particularly relevant as the Sb_2Se_3 film consists of one-dimensional $(Sb_4Se_6)_n$ ribbons aligned along the [001] direction via Sb-Se covalent bonds [72]. These ribbons are held together by van der Waals forces. The electrical conductivity perpendicular to the ribbon axis is restricted to the ribbon boundaries, leading to considerably higher resistance in that direction. This limitation is notably observed in the planar contact structure of TLM methods, as depicted in Figure 51. A study of conductance perpendicular to the substrate was conducted using the I-V characteristics of Sb_2Se_3-based solar cells, which were equipped with a Fe-S-O film as the back contact. The vertical structure of these solar cells facilitates transport along the ribbons, capitalizing on the favourable anisotropy of the Sb_2Se_3 film. The series resistance (R_s) of the solar cells was determined by performing a linear fit of the I-V characteristic (Figure 53b) in the first quadrant of the current-voltage plane. Given the higher electron mobility and thinner n-type layer compared to the hole mobility and thickness of Sb_2Se_3 ($\sim 4\mu m$), respectively, the contribution of the former layer to the total resistance of the solar cell can be considered negligible [72,100,153,154].

Consequently, R_s depends solely on the resistance of the absorber and the back contact layers. Following this approximation, R_s as a function of the different thicknesses (d) of the Sb_2Se_3 film (Figure 53b) can be expressed by the following relation:

$$R_s = R_{sc} + R_c = \rho_{sc} d + R_c \tag{4-24}$$

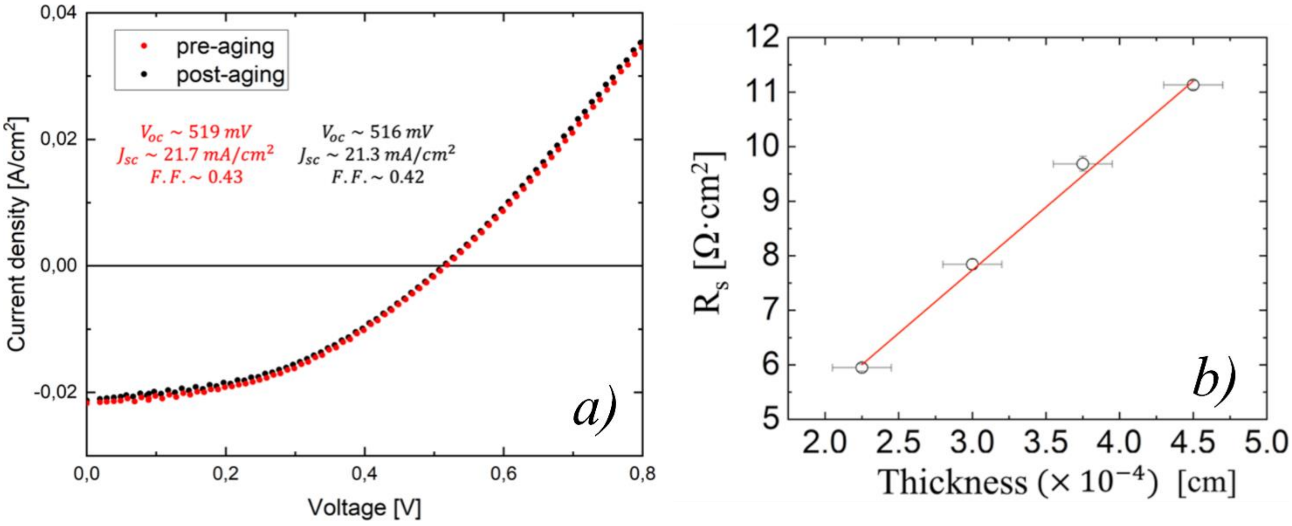

Figure 53. *a) I-V characteristic of Sb_2Se_3-based solar cell before (red dots) and after (black dots) three months of aging. b) Series resistance extrapolated from IV characteristic as a function of varying the absorber material thickness [100].*

The specific contact resistivity value was extrapolated from the y-intercept of the linear fit of the data shown in figure 53b yielding (0.8 ± 0.2) Ωcm^2. Furthermore, the slope allowed us to determine the resistivity of antimony selenide, in dark condition and for electrical conduction along the ribbons, which is (2.31 ± 0.07) $\cdot 10^4$ Ωcm. This value is an order of magnitude lower compared to resistivity measured with a planar structure.

It is important to note that the IV measurements were carried out under illumination. However, it is expected that the contributions R_{sc} and R_c remain consistent with their values in the dark. This expectation arises from the fact that the thickness of the Sb_2Se_3 layer and the distance of the back contact from the junction are significantly greater than the light penetration depth. One of the main challenges associated with polycrystalline solar cells is the diffusion of atoms from the metal contact. These atoms migrate within the absorber grain boundaries and may eventually reach the p-n junction impacting the lifetime of the device. As reported in figure 53a, the solar cell exhibits a PCE of about 5%, which is consistent with literature values. Devices stored at room temperature and in the dark were tested after three months, revealing minim al changes in the main photovoltaic parameters. Specifically, there was a decrease of 0.73% in V_{oc} and 0.15% in J_{sc}, while a slight increase of 0.12% in FF was observed.

In conclusion, a thin film of Fe-S-O can serve as an effective back-contact for Sb_2Se_3-based solar cells, exhibiting favourable contact resistivity and demonstrating long- time stability.

IMPACT OF WINDOW LAYER ON STRUCTURAL PERFECTION AND PHYSICAL PROPERTIES OF DEVICES

As detailed in the previous chapter, five different WLs were tested as substrates for the Sb_2Se_3 growth. The purpose was to determine which WL, through its interaction with the growing antimony selenide, promotes preferential grain growth along the (002) plane, perpendicular to the ribbon axis, thereby facilitating the conduction of photogenerated charges carriers. This approach aims to establish a correlation between crystallographic information regarding the preferential growth planes of Sb_2Se_3 and photovoltaic parameters, particularly J_{sc}. From the XRD patterns of antimony selenide, reported in figure 54, we selected the most representative and intense peaks, corresponding to the (221), (301), (211), (002), (310), (212), (041) and (141) crystal planes.

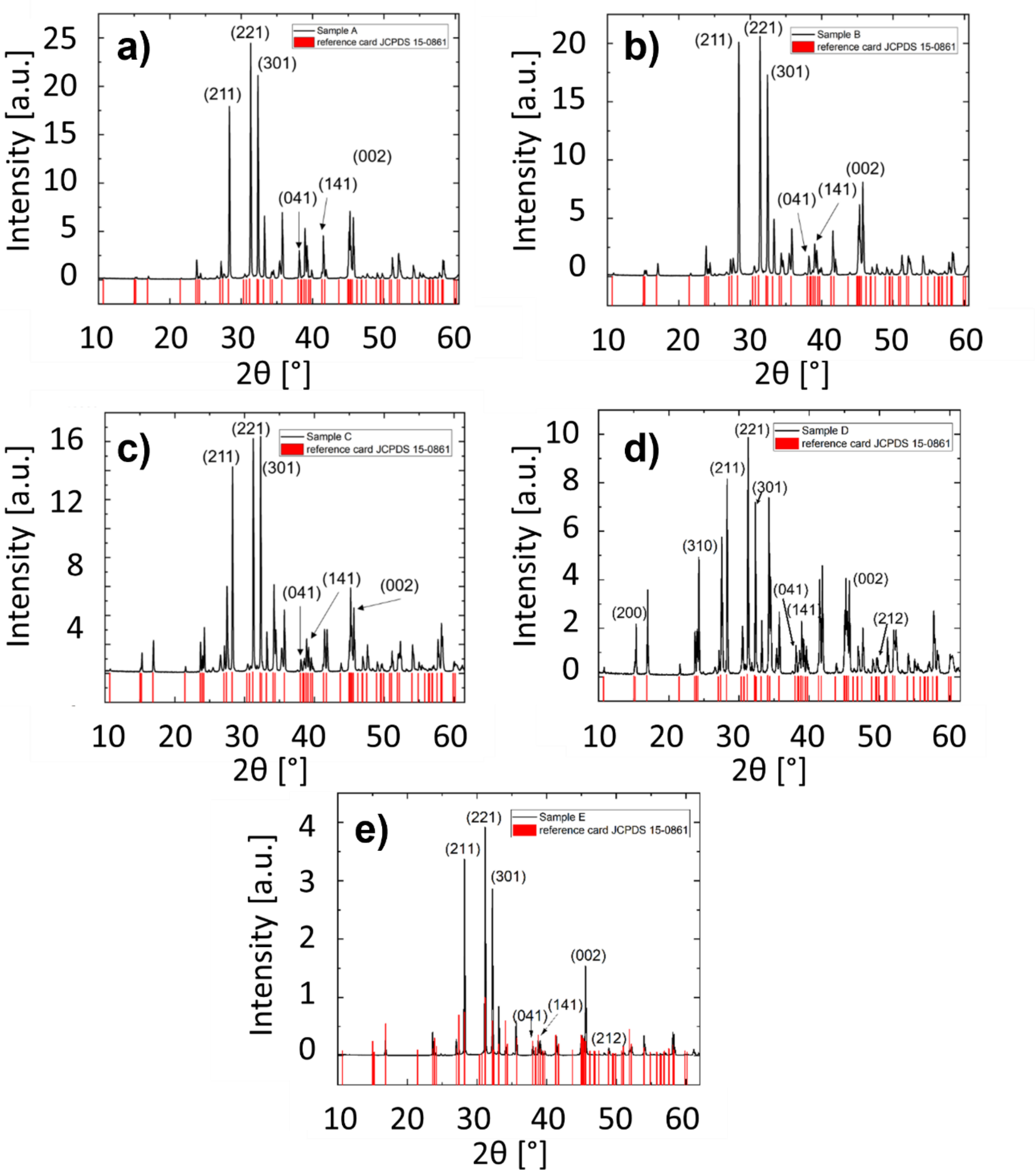

Figure 54. *XRD spectra of* Sb_2Se_3 *polycrystalline thin film, grown on a) CdS, b) CdS:F, c) CdSe, d)* As_2S_3 *and e) ZnCdS [91].*

To determine predominant crystal plane we utilized the figure of merit defined by the texture coefficient, as outlined in section 4.4.

Before presenting quantitative results of the texture coefficient, it is important to note that experimental XRD patterns of Sb_2Se_3 match precisely with the reference card JCPDS 15-0861. Combining this information with the Raman spectra shown in figure 55, which displays three peaks at 155, 192 and 212 cm^{-1} corresponding to B_{xg} and A_g Raman active vibrational modes [135], we can confidently assert that no spurious secondary phases are presents in any of the samples.

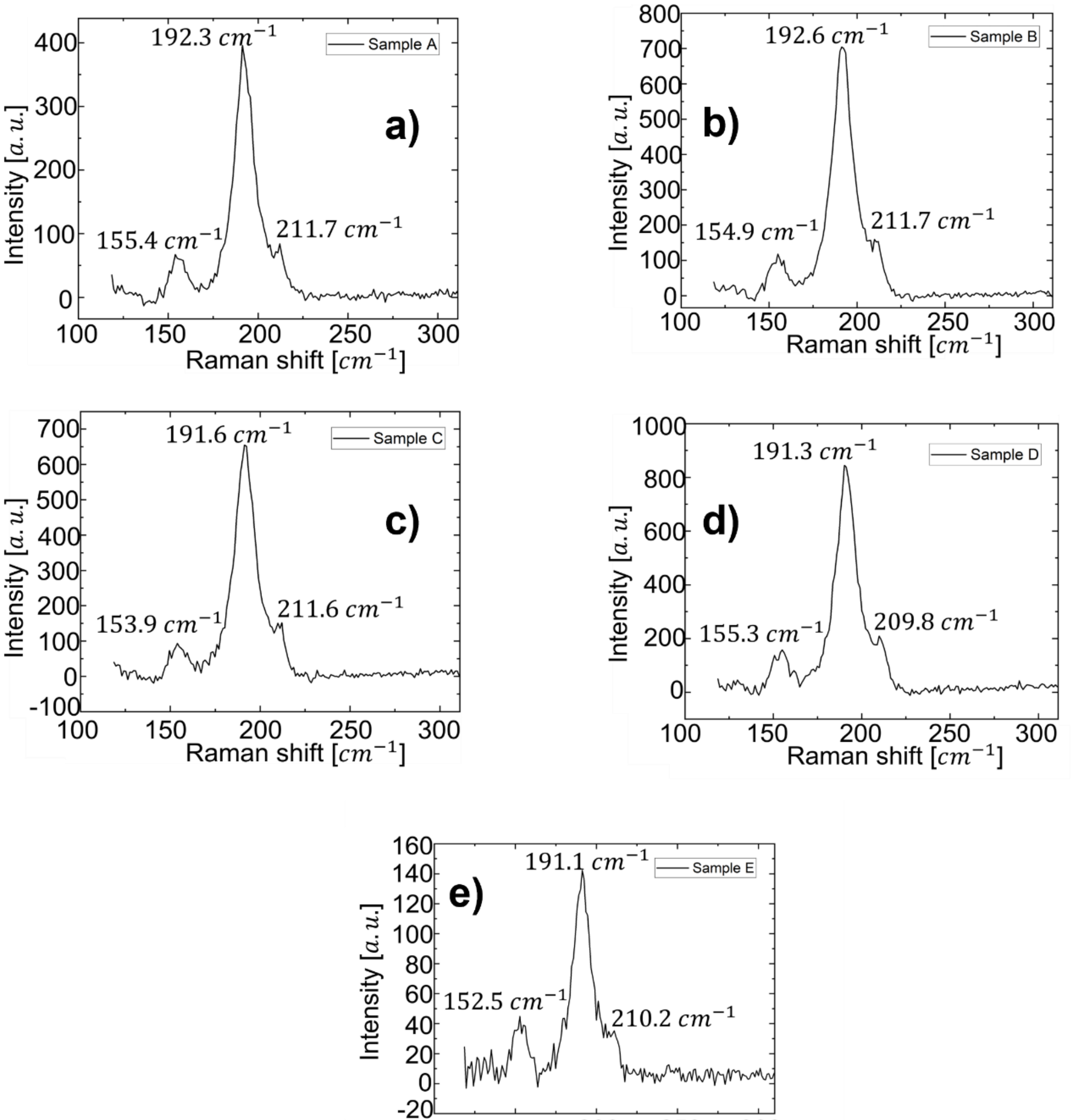

Figure 55. *Raman spectra of Sb_2Se_3 grown on (a) CdS, (b) CdS:F, (c) CdSe, (d) As_2S_3, and (e) ZnCdS [91].*

We established a threshold of 10% to ensure that the texture coefficient value significant. All XRD spectra exhibit the same peaks, albeit with varying intensities. Specifically, the TC analysis in figure 56 a) reveals a preferred orientation along the (301) plane for samples A

(WL: CdS) and C (WL: CdSe), while the (002) plane is favoured for samples B (CdS:F) and E (ZnCdS).

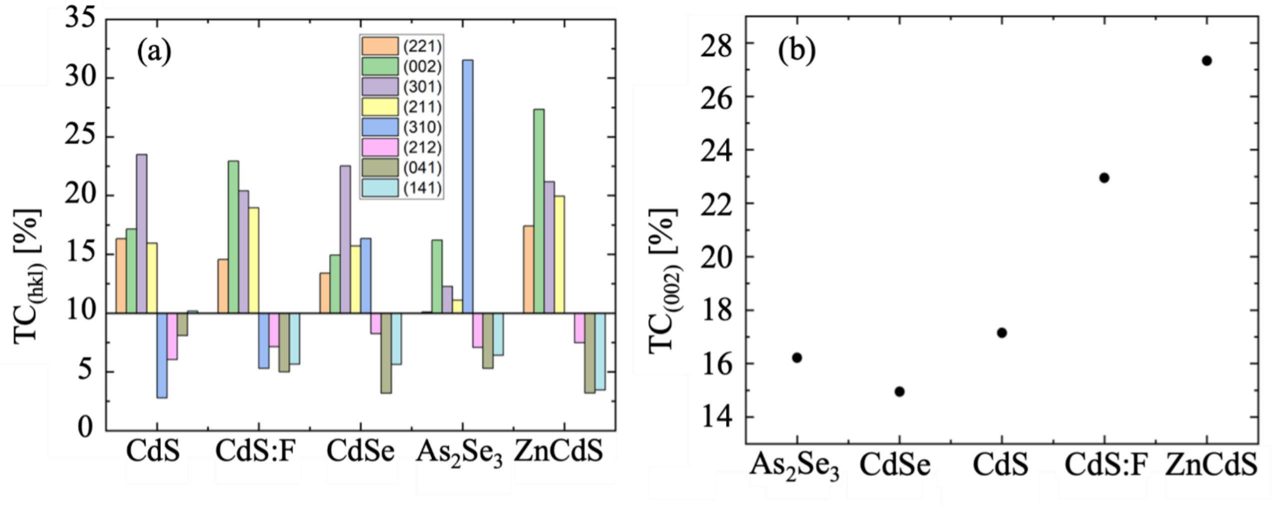

Figure 56. *(a) Texture coefficient for various crystalline planes; histograms below the 10% threshold should be considered as negative values relative to 10%; (b) Trend of the texture coefficient for the (002) plane across different window layers [91].*

Since this material crystallizes in the orthorhombic phase, with $(Sb_4Se_6)_n$ ribbons stacked parallel in the [001] direction, this orientation is believed to facilitate charge transport. Sample D (As_2S_3), where Sb_2Se_3 was grown utilizing the quasi-rheotaxia phenomenon, shows a very high TC_{310}, which is nearly negligible in other samples except for sample C. As illustrated in Figure 56b, growth along the [001] direction is highly dependent on the window layer and appears to be favoured by window layers containing zinc, reaching a maximum texture coefficient of 27% in sample E.

5.1 *ANTIMONY SELENIDE ELECTRICAL PROPERTIES*

Antimony selenide thin film was grown on an insulating ZnO layer to obtain an order of magnitude of the Sb_2Se_3 resistivity at room temperature (RT). The four-probes method was employed which is designed to measure only the resistance of the sample by utilizing four separate contacts for voltage and current measurements.

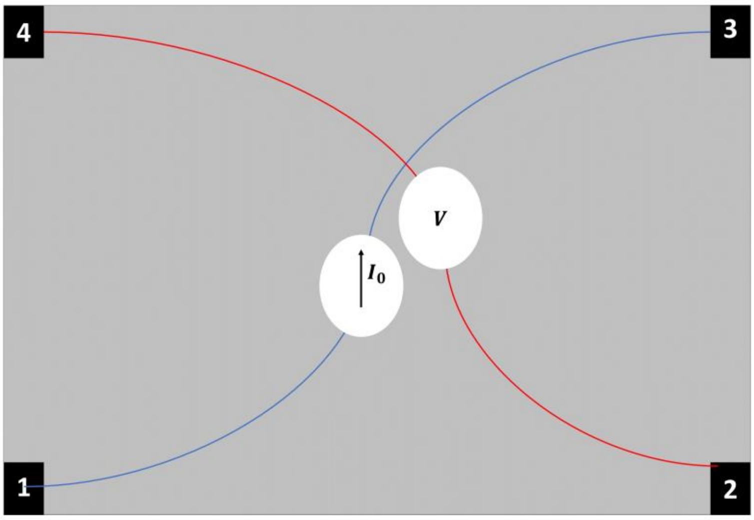

Figure 57. *Contact numbering scheme.*

Referring to figure 57, terminals 1 and 3 are used to inject a current, while contacts 2 and 4 measure the voltage drop directly across the section of the sample where the current flows. This configuration eliminates the resistive contribution from the wires and contacts, which would otherwise distort the measurement. The van der Pauw method [155], used to measure the resistivity of the material, extends the validity of the four-point technique to samples with non-standard geometries and is based on the following assumptions:

- A planar sample with uniform thickness;
- Electrical contacts on the edge of the sample;
- Point-like contacts;
- Compact film without macroscopic holes.

Experimentally, by permuting the two pairs of contacts, the following is obtained:

$$R_{12,34} = \frac{V_{34}}{I_{12}} \qquad R_{23,41} = \frac{V_{41}}{I_{23}} \tag{5-1}$$

By applying the van der Pauw method to determine the resistivity of the material, the following equation is obtained:

$$\exp\left(-\pi d \frac{R_{12,34}}{\rho}\right) + \exp\left(-\pi d \frac{R_{23,41}}{\rho}\right) = 1 \tag{5-2}$$

Where d is the thickness of the sample.

Experimentally, a van der Pauw measurement was performed at zero magnetic field and room temperature to determine the material's resistivity. The protocol involved calculating $R_{12,34}$ as the average of all possible contact combinations: $R_{12,34}$, $R_{21,34}$, $R_{34,12}$, and $R_{43,12}$. The same method was applied to calculate $R_{23,41}$. By numerically solving the previous equation, a dark resistivity value of $5 \cdot 10^3$ Ωcm was obtained for antimony selenide thin film, with an experimental error about 10%.

The current-voltage density characteristic of the complete Sb_2Se_3-based solar cells are shown in figure in figure 58.

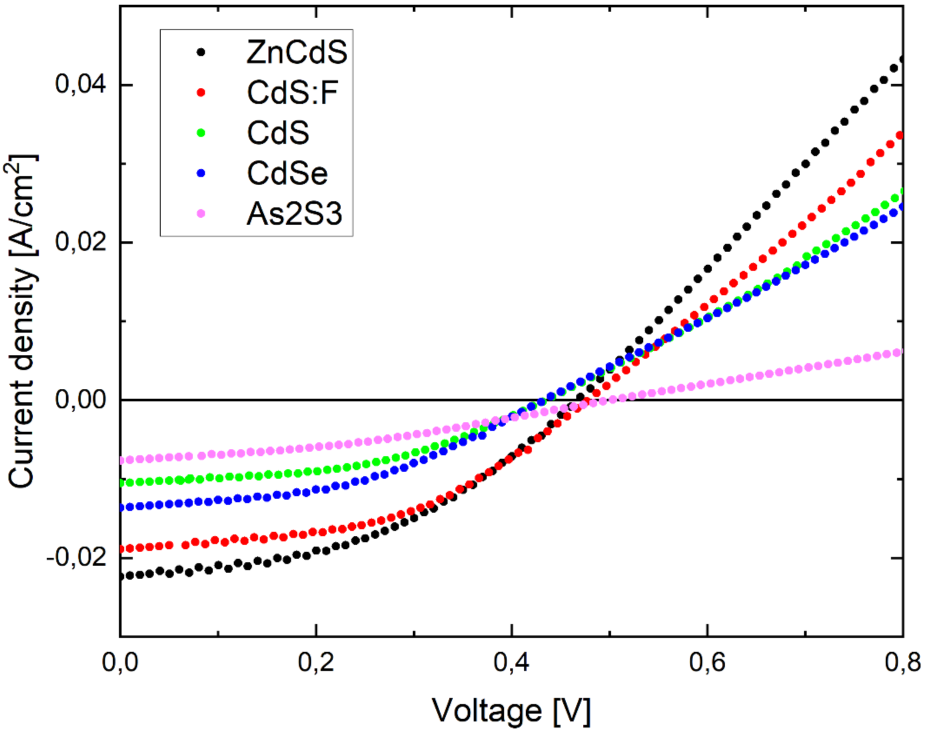

Figure 58. *J-V characteristics of the antimony selenide-based solar cells grown on different WL [91].*

From that curves are possible to extract the main photovoltaic parameters, that are reported in table 5.

Table 5. *Main photovoltaic parameters related to the solar cells shown in figure 58.*

-	Sample A (CdS)	Sample B (CdS:F)	Sample C (CdSe)	Sample D (As_2S_3)	Sample E ($Zn_{0.15}Cd_{0.85}S$)
Voc [mV]	435	478	433	593	469
Jsc [mA/cm²]	10.5	18.9	13.6	5.2	22.4
Rsh [Ωcm²]	139	107	98	124	378
Rs [Ωcm²]	15	9	16	49	8
FF [%]	45	46	43	34	43
PCE [%]	2.1	4.2	2.6	1.3	4.5

A correlation between the texture coefficient (TC) and the photovoltaic parameters is established by plotting J_{sc} against $TC_{(002)}$ corresponding to the [001] growth direction (Figure 59a). For samples B and E, which exhibit preferential growth along the [001] direction, the current increases with the texture coefficient for the (002) plane. In contrast, other samples exhibit lower J_{sc} due to a more random grain arrangement. Despite the $TC_{(002)}$ for the CdS window is higher than for CdSe, the photocurrent J_{sc} is lower because it also depends on other planes, particularly (301) (preferential for both) and (221). This indicates that achieving a high J_{sc}, requires more than just predominant growth of the Sb_2Se_3 film with the (002) plane parallel to the substrate (with [001] as the growth direction); it is also crucial to minimize the occurrence of other growth directions in favour of [001].

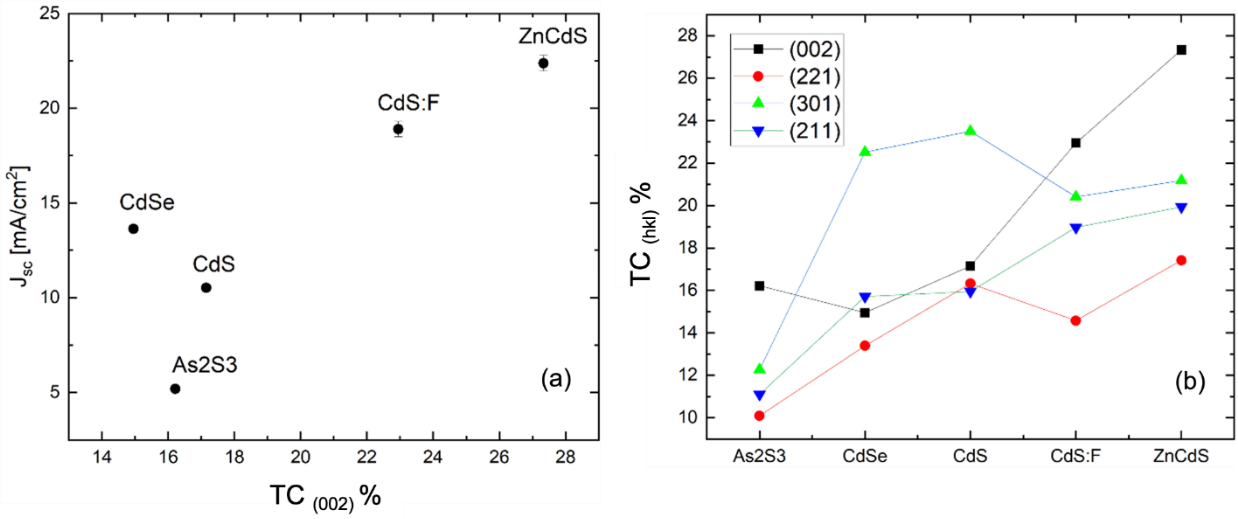

Figure 59. *(a) J_{sc} as a function of the $TC_{(002)}$ for different WLs; (b) The behaviour of texture coefficients for the main diffraction peaks across different window layers [91].*

The other photovoltaic parameters such as V_{oc} and FF, which are strongly influenced by the number of defects within the Sb_2Se_3, do not show a dependence on the TC values. To quantify the number of defects (trap density) inside the Sb_2Se_3 layer, the Space-Charge-Limited Current (SCLC) method can be used. By studying the J-V curve, on log-log scale, under dark conditions three different behaviours can be observed [156–159]:

- Ohmic region when $J \propto V$
- Trap-filling-limit (TFL) region, when $J \propto V^{n>2}$
- Child region, when $J \propto V^2$

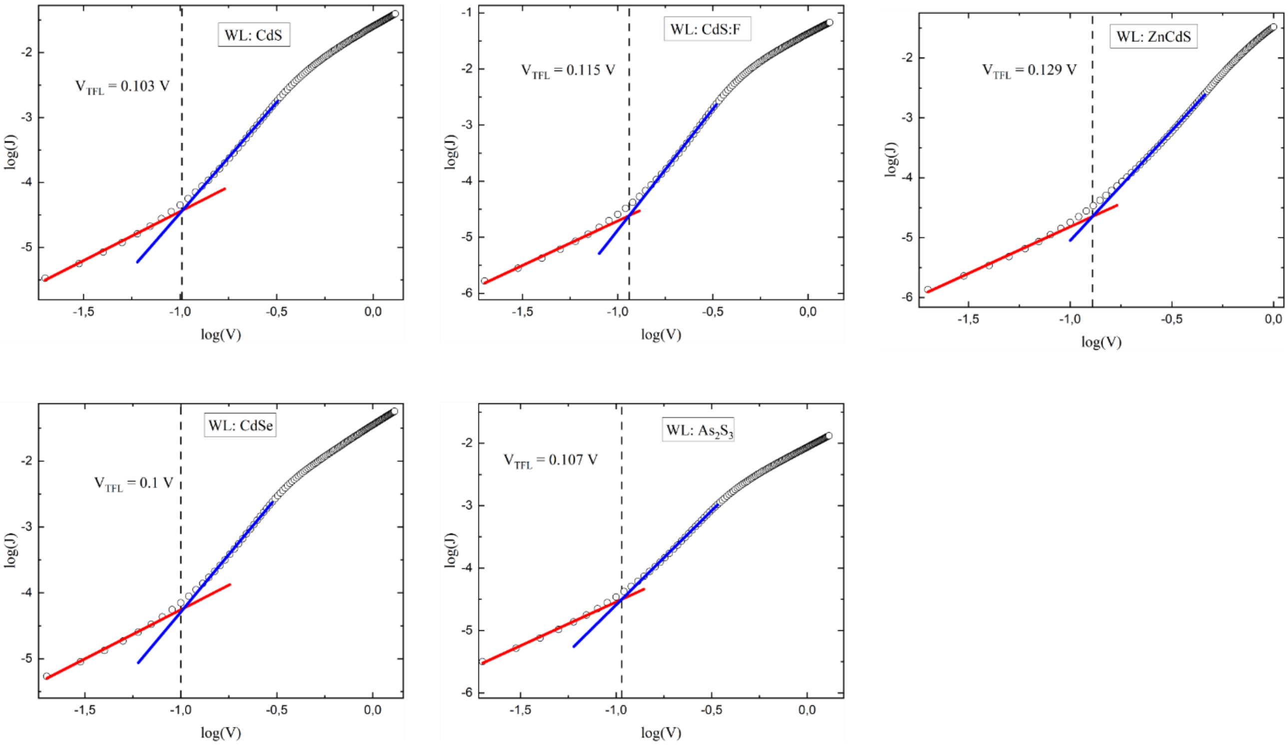

Figure 60. *Graphs of log(J) (expressed in A/cm²) vs log(V) (expressed in V) under dark conditions. The red line represents the ohmic region, while the blue corresponds to the TFL region.*

In a material containing traps, applying a higher voltage increases the injected current, which gradually fills the empty traps. The trap density (N_t) can be calculated from the trap-filling-limit voltage (V_{tfl}), identified as the point where the ohmic and trap-filling-limit linear fits intersect (as shown in Figure 60). This calculation is based on the following equation [160,161]:

$$N_t = \frac{2\epsilon\epsilon_0 V_{tfl}}{qL^2} \tag{5-3}$$

Where ε is the relative dielectric constant (assumed equal to 15.1 [162,163]), ε_0 is the vacuum dielectric constant, q is the electron charge and L is the thickness of the Sb_2Se_3 layer [164].

In all five samples, a high trap density, approximately $10^{13}\ cm^{-3}$ was observed within the antimony selenide layer. This value should be compared with the density of free holes inside Sb_2Se_3, which can be estimated using the following the relation:

$$\sigma = \frac{1}{\rho} = qp\mu \tag{5-4}$$

The resistivity is known from the previous measurement in the van der Pauw configuration, while the hole mobility can be measured through the intersection point between the Child and TFL regions. In the Child region, all traps are assumed to be filled, and thus the relationship between current and voltage follows the Mott-Gurney law [157]:

$$J_c = \frac{9}{8}\epsilon\epsilon_0\mu\frac{V_c - \Phi_{BI}}{L^3} \tag{5-5}$$

Where Jc and Vc are the values at the cross point between the trap-filling-limit and the Child regions. The built-in potential Φ_{BI} must be estimated exploiting the capacitance-voltage measurements in dark conditions. In general, the diode capacitance relative to the p-n junction is expressed with the equation [165]:

$$C = constant \cdot \left(1 + \frac{V}{\Phi_{BI}}\right)^{-\beta} \tag{5-6}$$

The quantity C refers to the junction capacitance, V is the applied reverse bias and β is a coefficient that takes into account the relationship between C and V. This coefficient can be determined as the slope of the linear fit by plotting the ln(C) vs ln(V) and, for an ideal abrupt p-n junction with a stepped charge density profile, β = ½.

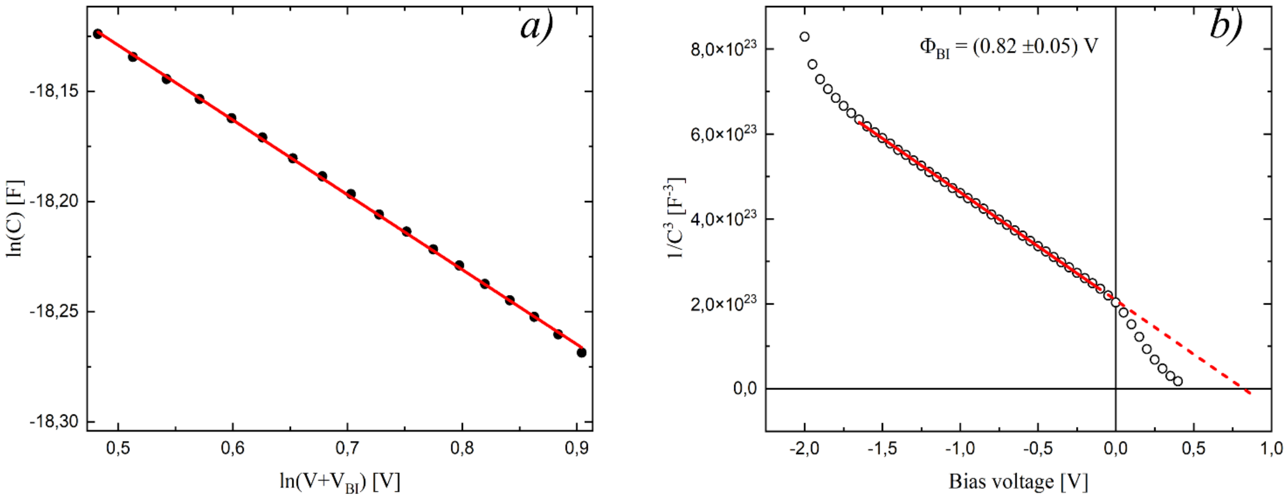

Figure 61. *a) graph and linear interpolation (red line) of ln(C) vs ln(V) in the region of reverse bias when V >> Φ_{BI}; b) Plot of 1/C^3 as a function of the applied reverse bias.*

From the linear fit shown in figure 61a, the β value is found to be 1/2.94, which is very close to 1/3. This result suggests a linear dependence of the space charge density within the space charge region, and it is called linearly graded junction. The theory of the linearly graded junction is derived from the solution of the Poisson equation considering the charge density distribution inside the depletion region as reported in figure 62.

$$\rho = N_D - N_A = e\alpha x \tag{5-7}$$

With $-\frac{W}{2} \leq x \leq \frac{W}{2}$, where W is the depletion region and α is the impurity gradient, expressed in cm^{-4}.

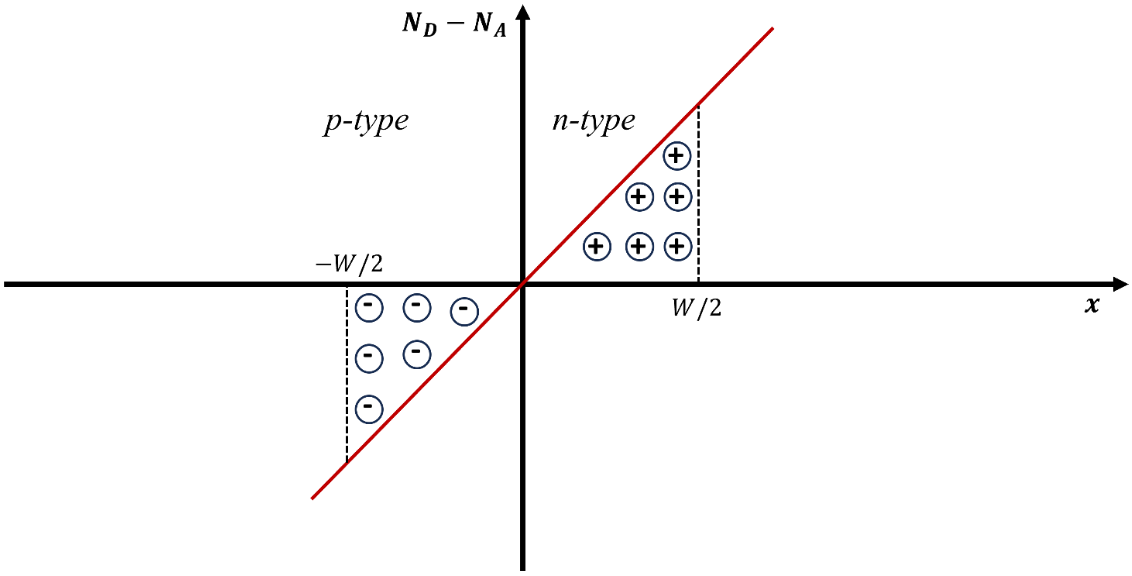

Figure 62. *Sketch of the charge density distribution in a linearly graded junction.*

By solving the Poisson equation with these constrains, the relationship between the junction capacitance and the applied voltage is found [166,167]:

$$\frac{1}{C^3} = \frac{12(\Phi_{BI} - V)}{q(\alpha)A^3(\epsilon_0\epsilon)^2} \tag{5-8}$$

Where A is the active area of the solar cell.

The relationship between 1/C^3 and the applied bias is shown in figure 61b, and the linear fit in the negative bias region was used to determine the built-in potential from its intercept with the V-axis, which measured (0.82 ± 0.05) V. This measurement was carried out only on the cell with the CdS+ZnCdS window layer system, since this structure will be mentioned later in this PhD thesis, as it shows the best PCE and the highest TC value related to the (002) growth plane of Sb_2Se_3 grains.

In this way, the hole mobility can be determined through the Mott-Gurney law, once the intersection point between the TFL region and the Child region is known, as shown in the figure 63.

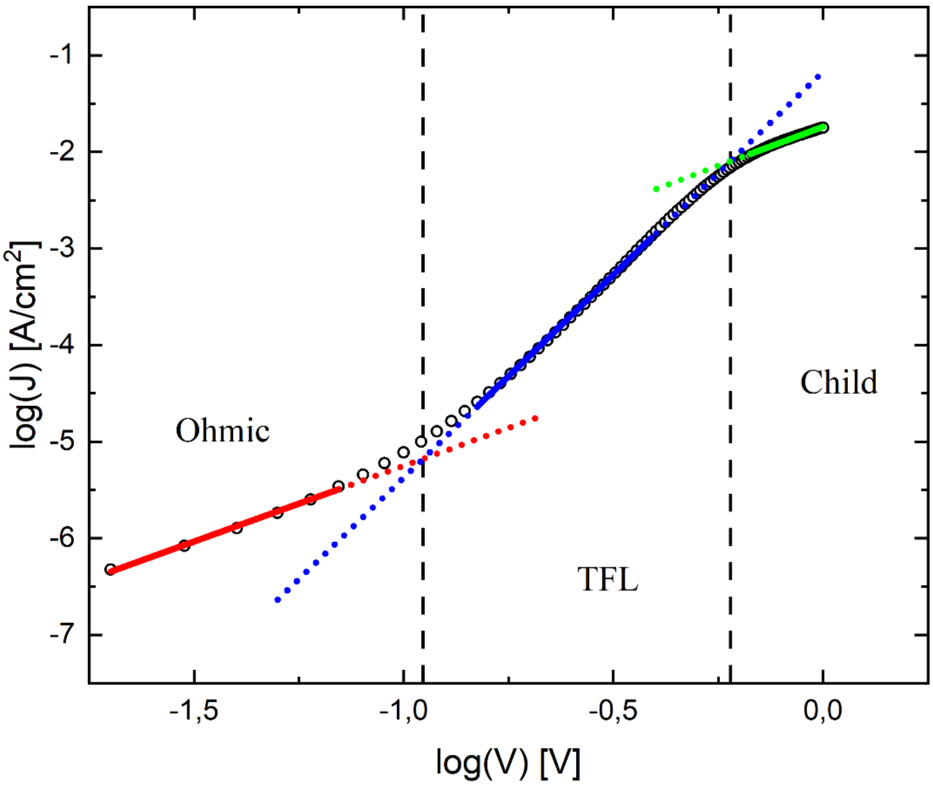

Figure 63. *By graphing log(J) (in A/cm²) against log(V) (in V) under dark conditions, three distinct regions can be observed, separated by dashed vertical lines.*

A hole mobility values of $\mu_h \approx 8.9$ cm² V⁻¹ s⁻¹ are revealed, which are consistent with the values reported in literature for Sb_2Se_3 grains oriented preferably along the [001] direction [47,97]. Finally, the hole density inside the absorbing material is found to be $p \approx 1.4 \cdot 10^{14}\ cm^{-3}$, only one order of magnitude greater than the density of defects present in the material. This fact strongly influences the V_{OC}, which is why no relationship with $TC_{(002)}$ was found. Summarizing the results of this chapter, it was observed that the preferential growth of Sb_2Se_3 grains is parallel to the ribbon axis when the CdS+ZnCdS system is used as the window layer, which is beneficial for the transport and extraction of photogenerated charges. Furthermore, a high density of defects within the absorber material and a low density of free holes were observed, which demonstrates the weak p-type conduction of antimony selenide. Furthermore, to improve the photovoltaic performance of Sb_2Se_3-based solar cells, it is necessary to further study and optimize the interaction between the absorber material and the window layer (WL) to further enhance the preferential growth of grains along the [001] direction. Additionally, it is advisable to investigate strategies for incorporating extrinsic atoms into the antimony selenide crystal lattice to dope p-type the material, thereby making the numerous traps present in the material less effective.

INTERPRETATION OF THE V_{OC} DEFICIT

In this chapter, a detailed analysis of the Sb_2Se_3-based solar cell in a superstrate configuration is presented, utilizing the J-V characteristic as a function of both temperature and wavelength, CV measurements, and admittance spectroscopy. The aim is to clarify the anomalies present in the J-V characteristic such as the kink point and the cross-over. As an explanation, a theoretical model is proposed that assumes the existence of a potential barrier at the interface between the window layer and the absorber material.

The structure of the solar cell (not to scale) under examination is shown in Figure 64a, together with the HR-TEM cross-section image of the device constituent layers. The main photovoltaic parameters of the J-V characteristic, depicted in figure 64b, are listed in Table 6.

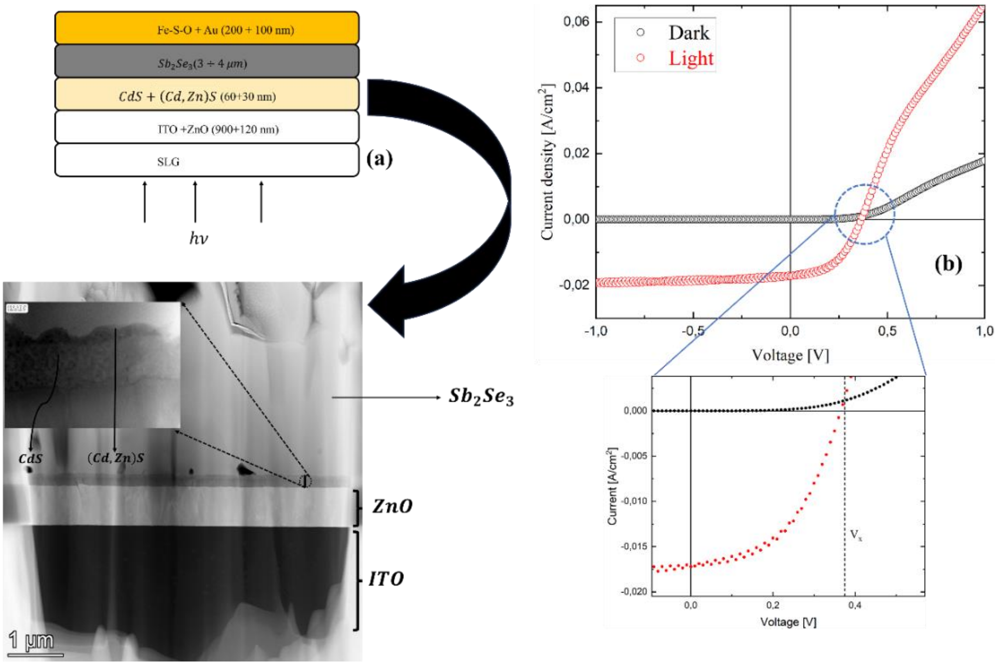

Figure 64. *(a) A schematic diagram of the Sb_2Se_3-based solar cell alongside a cross-sectional bright field (BF) TEM image of the device; (b) current density-voltage characteristics shown in the dark (black dot) and under solar simulator illumination with 700 W/m^2 AM1.5G filtered light (red dot). The inset highlights the crossover point V_X.*

Table 6. *Key photovoltaic parameters of the examined solar cell include: V_{oc} (open circuit voltage), V_X (crossover voltage), J_{sc} (short-circuit current density), FF (fill factor), PCE (power conversion efficiency), R_{sh} (shunt resistance), R_S (series resistance), and n (ideality factor).*

V_{oc} [mV]	365 ± 6.0	PCE [%]	4.36 ± 0.3
V_x [mV]	375 ± 6.0	R_{sh} [Ωcm^2]	378 ± 16
J_{sc} [mA/cm^2]	17.1 ± 0.3	R_S [Ωcm^2]	3.6 ± 0.1
FF [%]	49 ± 3.0	n	2.1 ± 0.1

The series resistance and the ideality factor are extracted manipulating the J-V expression:

$$\frac{dV}{dJ} = \frac{nKT}{q}\left(J + J_{ph}\right)^{-1} + R_S \tag{6-1}$$

Where J_{ph} is the current related to the photogenerated carries that can be approximated by J_{sc}, K is Boltzmann's constant, and T is the absolute temperature.

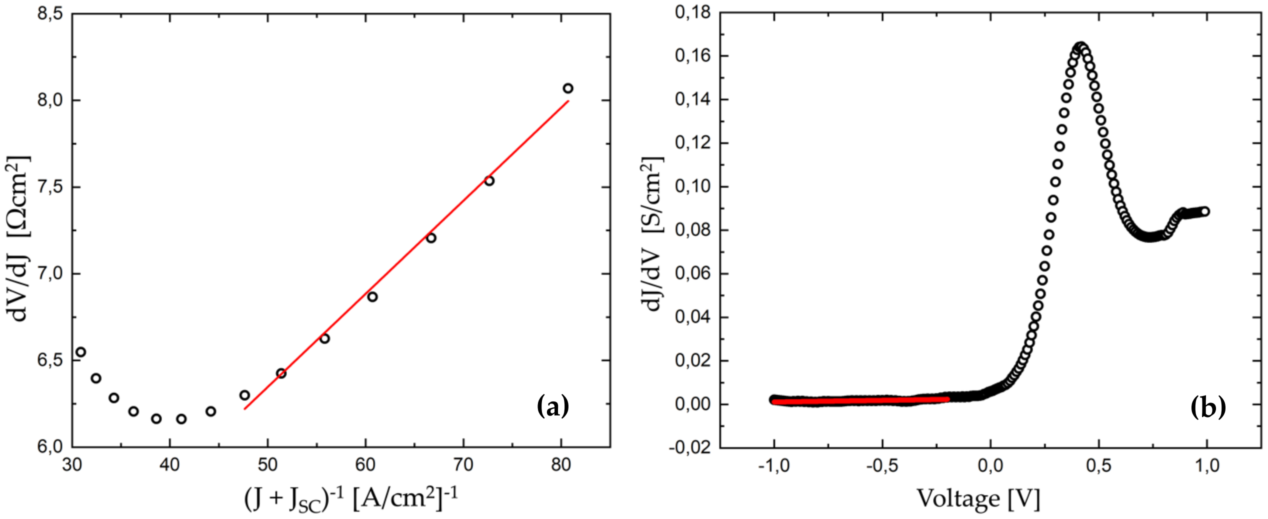

Figure 65. *(a) Linear fit of dV/dJ for determining R_S. (b) Linear fit of dJ/dV for determining R_{sh}. These curves were derived from J-V measurements taken under 700 W/m^2 AM1.5G solar simulator illumination at a temperature of 298 K.*

Referring to Figure 65a, by performing a linear fit around the points where $V \geq V_{oc}$, the diode ideality factor can be obtained from the slope of the regression line, while the series resistance can be determined from the y-intercept. Instead, referring to Figure 65b, by plotting dJ/dV vs V, the shunt resistance can be obtained through the intercept of the linear fit in the region of experimental points around J_{sc}.

$$\frac{dJ}{dV} = \frac{qJ_0}{nKT} e^{\left[\frac{q(V-JR_S)}{nKT}\right]} + \frac{1}{R_{sh}} \tag{6-2}$$

Furthermore, in the interpretation of subsequent measurements, it must be taken into account that the interface between the p-type and the n-type materials is not an abrupt junction because the device is a heterojunction. In fact, the lattice mismatch between Sb_2Se_3 and $Zn_{0.15}Cd_{0.85}S$ can be estimated to be around 2.63%.

The lattice parameter of ZnCdS is calculated using Vegard's law, with a_{CdS} = 4.14 Å and a_{ZnS} = 3.82 Å [168,169].

$$a_{Zn_{0.15}Cd_{0.85}S} = 0.15a_{ZnS} + 0.85a_{CdS} = 4.092 \text{ Å} \tag{6-3}$$

The lattice parameter of Sb_2Se_3 is $b_{Sb_2Se_3}$ = 3.9858 Å, as in our sample Sb_2Se_3 grains preferentially grows along the [001] direction, parallel to the growth axis [91].

A lattice mismatch greater than 1% creates numerous interface states at the junction, which act as recombination centers and can reduce the number of carriers reaching the device electrodes. This problem has been addressed in CdS/CdTe-based solar cells by forming an intermixing layer that gradually adjust the lattice mismatch [170]. Similarly, in antimony selenide-based solar cells, the incorporation of such an intermixing layer is crucial to overcome the lattice mismatch problem.

The hypothesis on the presence of an intermixing layer between ZnCdS and Sb_2Se_3, based on the experiences with the CdS/CdTe system, was experimentally confirmed by HRTEM and EDS cross-section measurements on the complete Sb_2Se_3-based cell. Figure 66b displays the EDS spectrum corresponding to the cross-section marked in green in Figure 66a.

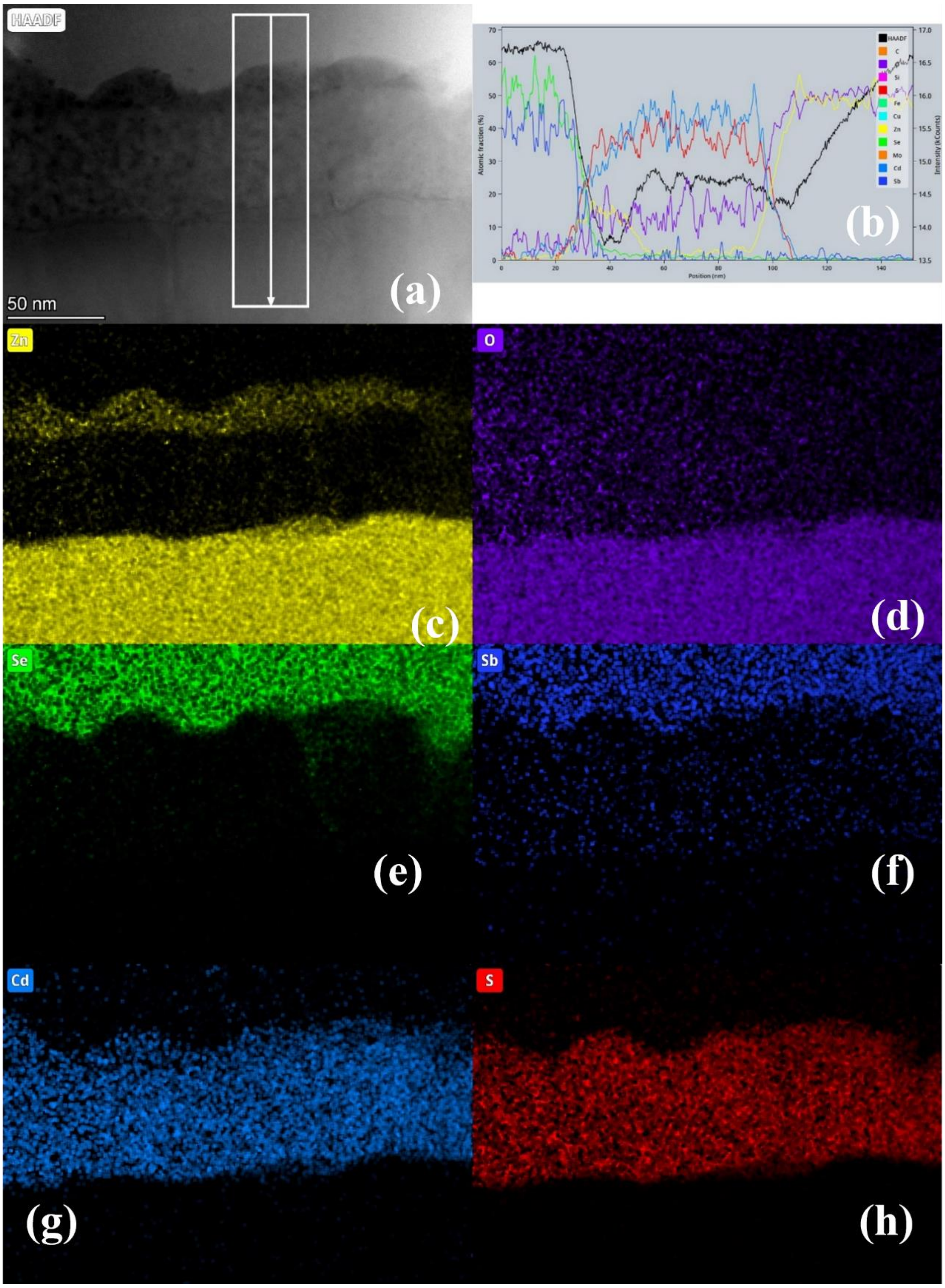

Figure 66. *Cross-sectional HAADF TEM image with elemental EDX maps from the ZnO/CdS/ZnCdS/Sb_2Se_3 interface. The white box on the HAADF image indicates the area from which the integrated intensity profile, with calculated atomic percentage, was taken. Diffusion of Se and Sb atoms into the sulfide layer is observed.*

In Figures 66c, 66d, 66e, and 66h, interdiffusion of selenium and antimony atoms into the sulfide layer is observed, forming an intermixing layer with an estimated thickness of about 20 nm, as indicated by the EDS profile spectrum shown in Figure 66b. Additionally, a significant amount of oxygen (10 to 20 at.%) appears outside the ZnO layer, including in the Sb_2Se_3 layer.

A plausible explanation for this anomalous result is that the thin TEM lamella of about 30 nm, with its large free surface, tends to oxidize during sample transfer. Therefore, the detected oxygen is probably not present in the original layers, especially not in the Sb_2Se_3. After TEM investigation, the samples were placed in a vacuum (10^{-6} mbar), but the measured oxygen content was 1.5 times higher on the second day, likely due to double transfer, which exposed the sample to air contamination.

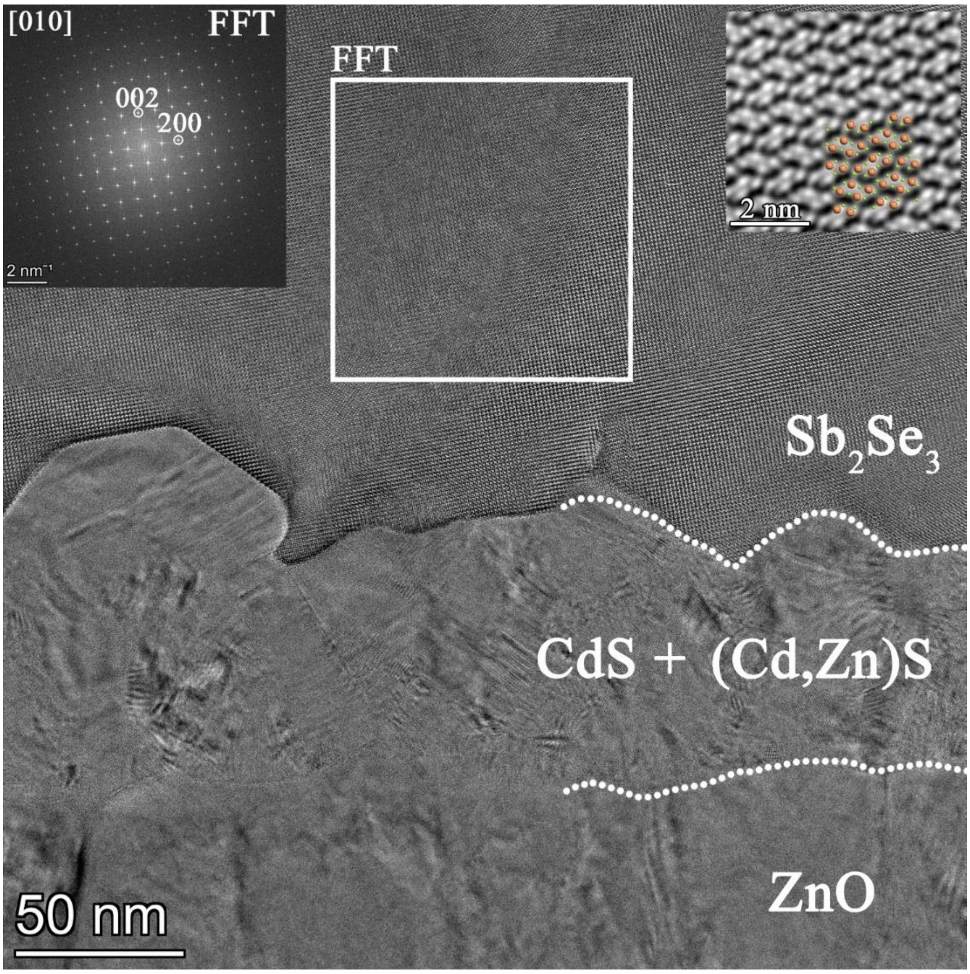

Figure 67. HRTEM image from the ZnO/CdS/ZnCdS/Sb_2Se_3 interfaces. The FFT from the marked area is indexed as orthorhombic (space group: Pnma) Sb_2Se_3 from the [010] projection. In the upper right corner, the HAADF image shows the projected atomic structure of Sb_2Se_3. The CdS and ZnCdS layers are polycrystalline.

TEM measurements on the Sb_2Se_3 do not show any spurious secondary phases of antimony oxides, consistent with the results obtained in Figure 67.

6.1 THE KINK EFFECT IN THE JV CURVE

The J-V characteristic of the solar cell, shown in Figure 64b, exhibits different behaviour under both dark and illumination conditions. Specifically, under illumination, a pronounced bend can be observed at high voltages in the first quadrant of the J-V curve. This behaviour can be explained by assuming the presence of an energy barrier within the absorber material, schematized using a two-diode-in-series model, as depicted in Figure 68a [172,173].

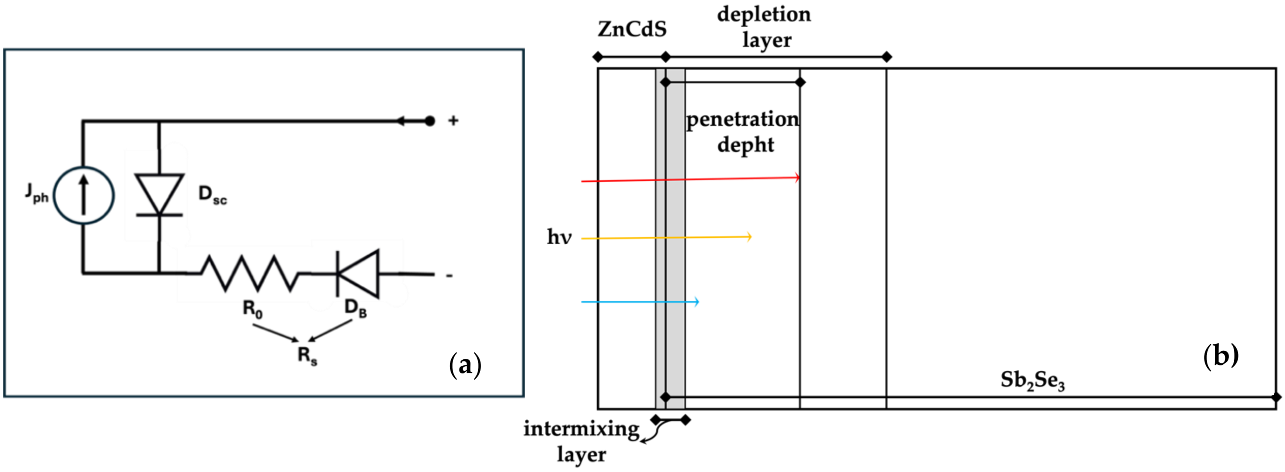

Figure 68. (a) The solar cell model illustrates a secondary barrier diode placed in anti-series with respect to the primary barrier diode. R_0 *and* D_B *represent the contact resistance and threshold barrier of the anti-series diode, respectively. (b) A non-scale diagram of the proposed ZnCdS/*Sb_2Se_3 *junction model highlights the intermixing layer between ZnCdS and* Sb_2Se_3*, the penetration depth where 63% of the incoming light is absorbed, and the depletion layer.*

As already explained in the paragraph 3.2, in the first quadrant of the voltage-current characteristic, the main junction is completely flattened by the power supply potential. In this scenario, holes are extracted from the negative terminal, while electrons are extracted from the positive terminal. The opposite occurs in the fourth quadrant, where the electric field generated by the junction pushes the photogenerated charges in the opposite direction. Specifically, considering the heterojunction between ZnCdS and Sb_2Se_3, this concept is certainly true for electrons, but not for holes. In fact, these two materials have different band gaps, and it has been calculated that there is a cliff-like discontinuity in the valence band (VB), as represented in figure 69. This causes the holes to tend to accumulate at the junction interface, on the p-side, forming a potential barrier due to the CBO between the VBs of ZnCdS and Sb_2Se_3. As a result, some of the photogenerated holes, together with those supplied by the generator, remain trapped in the Sb_2Se_3 layer near the ZnCdS interface. The photogenerated holes depend on the intensity and wavelength of the light illuminating the cell, while the holes supplied by the generator depend only on the applied bias. These trapped holes, unable to move freely, enhance recombination with electrons, leading to a noticeable reduction in current and causing a kink in the JV characteristic curve [174]. In the dark, this phenomenon is only slightly visible because the resistance of the materials permits only a weaker current to flow, resulting in a lower number of trapped holes.

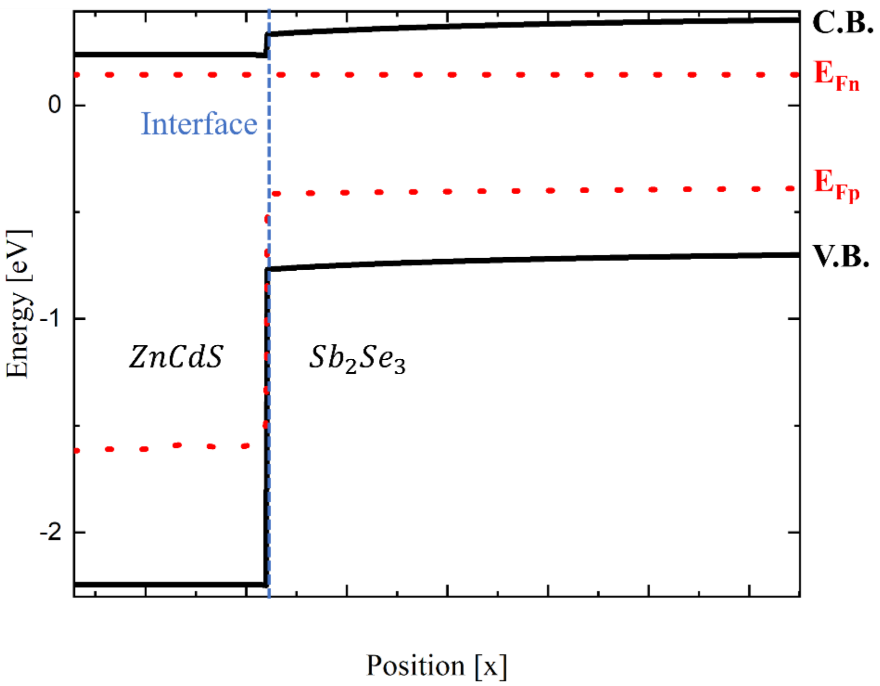

Figure 69. *A visual depiction of the band structure profiling at the ZnCdS/Sb_2Se_3 interface.*

To determine the height of the energy barrier, assuming that the variation of the barrier height as a function of temperature follows a thermally activated behaviour like [175]:

$$R_S T = C\, e^{\frac{\Phi_B}{KT}} \tag{6-4}$$

We have performed the J-V characteristics (under light conditions) as a function of temperature.

In the above equation, R_s represents the total resistance, which includes the resistance of the materials forming the solar cell, the contact resistances R_0, and the resistance of the additional barrier D_B (see figure 68a). C is a constant that is independent of the temperature (T), while Φ_B is the barrier height. Assuming that R_0 is sufficiently small compared to the barrier resistance and therefore negligible, we consider that the temperature dependence of R_s is mainly due to D_B, which is the circuit representation of the barrier created by the trapped charge.

The barrier height was estimated to be (306 ± 9) meV from the slope of the linear fit of plot of the ln(R_sT) vs 1/T, reported in figure 70a [176–178].

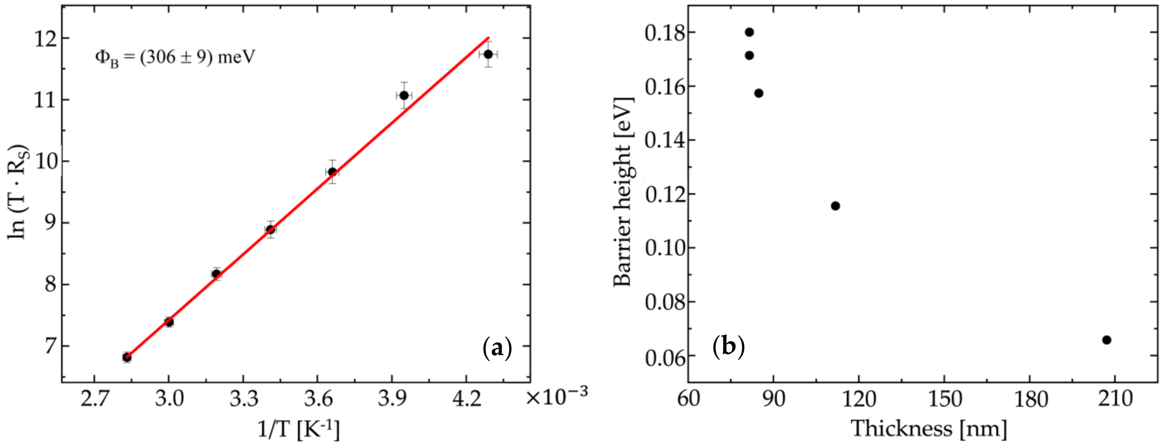

Figure 70. *Each data point in both graphs was generated by illuminating the sample with an LQX 1000 lamp. (a) The Arrhenius plot shows* $ln(TR_s)$ *(in* $K\cdot\Omega\cdot cm^2$*) plotted against (1/T). Each experimental value was obtained by measuring the J-V characteristic over temperatures ranging from 196K to 353K. (b) The height of the additional barrier to the junction is plotted against distance. Each data point was obtained using band-pass filters centered at 650 nm, 750 nm, 850 nm, and 950 nm, and all measurements were normalized to the same light intensity in both graphs (a) and (b).*

In Figure 70b, the variation of the energy barrier as a function of incident wavelength is reported. According to the Lambert-Beer law, the light penetration depth within the material depends on its wavelength and therefore also on the thickness of the material where holes accumulate [94]. The barrier height as a function of wavelength was measured using optical band-pass filters centered at 650 nm, 750 nm, 850 nm, and 950 nm, and the J-V curves were normalized to the same number of photons absorbed by antimony selenide. Figure 70b illustrates the variation of Φ_B as a function of the thickness of the illuminated layer, i.e., the penetration depth, where 82% of the light is absorbed in a thickness equal to two penetration depths. This result excludes the possibility that the energy barrier could be due to the back-contact, as its value would remain constant with respect to wavelength, hence independent, since all the light has been previously absorbed by the antimony selenide. Secondly, the barrier due to trapped holes is maximum in the junction region near the interface and decreases inside the absorbing material.

6.2 CROSSOVER EFFECT IN THE JV CURVE

In an ideal solar cell, the current voltage characteristic is just a translation of the dark J-V characteristic. In our case this is not true, as can be seen from the inset in figure 64b, due to a crossover, that indicates a potential-dependent photocurrent [179–181].

In general, the photocurrent has a negligible dependence on the voltage V and mainly depends strongly on the intensity of the incident light. The current flowing in the solar cell can be described using the superposition principle [174], but considering that in our case the photocurrent heavily depends on the applied voltage:

$$J_L(V,g) = J_{D_{sc}}(V,g) + J_{ph}(V,g) \tag{6-5}$$

With g the rate of generation of photogenerated charges, V is the applied bias, $J_L(V, g)$ is the total current flowing, $J_{Dsc}(V, g)$ is the current that flows in the p-n junction, and $J_{ph}(V, g)$ is the photogenerated current.

The net current flowing in the diode without the contribution of the light-induced generation, considering the dark current, can be expressed as:

$$J_{D_{sc}}(V,g) = J_j(V,g) - J_{dark} \tag{6-6}$$

Where $J_j(V,g)$ is the current injected by the p-n junction and J_{dark} is the current relative to the diode in dark condition and can be considered a constant because depends minimally on the potential.

Some information about the crossover can be found from the difference Δ between the current that flows in the solar cell and the dark current of the diode:

$$\Delta = J_L(V,g) - J_{dark} = \left[J_j(V,g) - J_{dark}\right] + \left\{J_{ph}(V,g) - J_{dark}\right\} \tag{6-7}$$

From the first term indicated by square bracket, we can deduce that if the current injected by the junction also depends on illumination, then this term dominates in Δ, making the crossover primarily dependent on it. Conversely, if photogeneration depends also on the potential, then the second term (curly brackets) becomes prevailing. The difference Δ reaches an equilibrium at the point V_x. In our Sb_2Se_3-based cell, the p-n junction acts as a hole-blocking heterojunction due to the electron affinity of the n-type layer (ZnCdS) and the doping level of the p-type layer (Sb_2Se_3). As mentioned above, this results in an accumulation of positive charge in the p-type region of the junction, making $[J_j(V,g) - J_{dark}] > 0$. This is also true when considering the intermixing layer, which reduces lattice mismatch but does not completely resolve the valence band offset between ZnCdS and Sb_2Se_3. Now the question is whether these sentences are sufficient to explain the presence of the crossover. First, it should be noted that the potential observed at the contacts is not the built-in potential Φ_{BI}, but rather the potential that drops across the material and contact resistances. We can denote this potential as $V_{bi,c}$ to indicate that it is the potential observed at the contacts. Second, as mentioned above, in the ZnCdS/Sb_2Se_3 cell under moderate forward bias, only electrons can flow through the p-type contact, while holes are partially blocked by the barrier between the valence bands of ZnCdS and Sb_2Se_3. Therefore, the photocurrent is voltage-dependent but cannot drop to zero until all electrons and holes have reached their respective contacts. Nonetheless, the accumulation of positive charge in the junction region under illumination implies a change in the internal electric fields. This, in turn, causes the diode current to depend on the light-induced charge carriers generation, affecting the point at which the photocurrent and dark current intersect. Two scenarios can be distinguished:

1. If the doping density within the CdS + ZnCdS layer is quite low, around 10^{13} cm^{-3}, the electric field drops mainly in the n-type region, leaving the p-type region only slightly depleted. This results in a relatively small accumulation of photogenerated positive charges, thus requiring a higher potential to reach the crossover voltage, which is typically greater than $V_{bi,c}$.
2. On the other hand, if the n-type region of the junction is more heavily doped than the p-type region, the p-type region experiences greater depletion. This causes more pronounced band bending in this region, leading to an increase in positive charge accumulation, resulting in a crossover point lower than $V_{bi,c}$.

To determine which situation applies, we need to evaluate how much $V_{bi,c}$ depends on the series resistances of the device. Considering the series resistance values of our solar cell ($R_s \approx 3.6\ \Omega\cdot cm^2$), the relative voltage drop ($J\cdot R_s$) across the materials is not significant, especially when the current density is very low, i.e., when the voltage is close to V_{oc} and/or the crossover point V_x. Therefore, $V_{bi,c}$ is approximately equal to Φ_{BI}. In summary, the condition where $V_x < \Phi_{BI}$ occurs due to the higher doping level in Sb_2Se_3 compared to ZnCdS.

Figure 71a shows the variation of V_{oc} and V_x as a function of the incident wavelength. Measurements were conducted using bandpass filters centered at 650 nm, 750 nm, 850 nm, and 950 nm, and the curves were then normalized to the same number of photons absorbed by the Sb_2Se_3. According to the definition of V_x, its dependence on light (g-generation) always shows slightly higher values than V_{oc}, and their difference seems to increase with decreasing incident wavelength, as shown in Figure 71b. The decrease in photovoltage at longer wavelengths can be explained by the fact that carriers generated deeper in the absorber material have to travel a longer distance to reach the electrodes, resulting in an amplification of recombination effects. This effect causes a reduction in V_{oc}. Additionally, the graph in Figure 71a shows a non-uniform dependence of Vx on light generation.

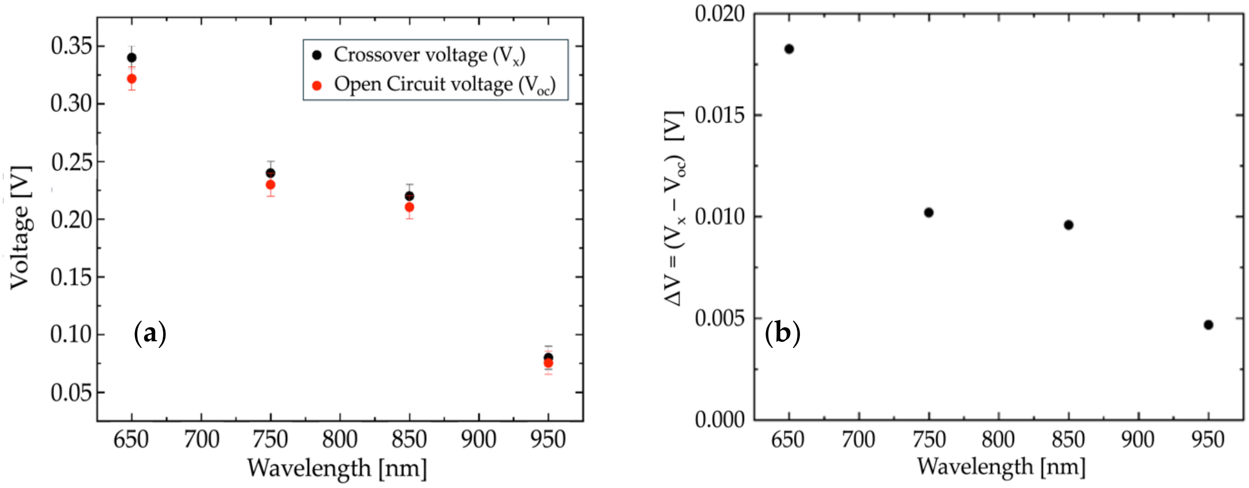

Figure 71. *(a) Measurements of V_x and V_{oc} were taken at different wavelengths, with all voltage values normalized to an equal number of absorbed photons. Bandpass filters centered at 650 nm, 750 nm, 850 nm, and 950 nm were used to select the various wavelengths. (b) $\Delta V = V_x - V_{oc}$ as a function of the wavelength of absorbed light.*

As previously demonstrated, holes generated by short-wavelength light are created close to the junction, which promotes effective charge accumulation compared to holes generated by longer-wavelength light. This trend is consistent with the data shown in Figures 71a and 71b. In any case, the hypothesis $V_{oc} \leq V_x \leq \Phi_{BI}$ is confirmed since the values of V_x tend to deviate more from V_{oc} in the hole generation region close to the interface.

.

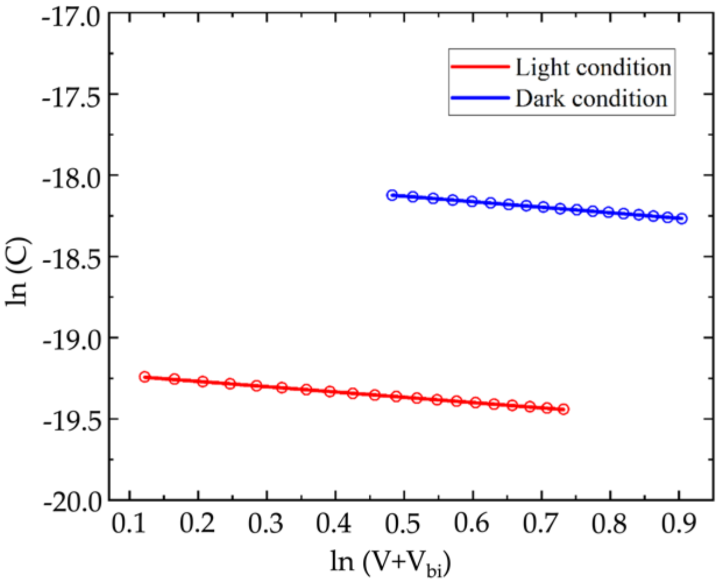

Figure 72. *A plot of ln(C) (where C is in units of F) against ln(V +*Φ_{BI}*) (where V +* Φ_{BI} *is in units of V) is generated under both light and dark conditions. The experimental data is linearly fitted in the reverse bias region where V >>*Φ_{BI}*.*

Another important analysis supporting the crossover hypothesis is the comparison of Φ_{BI} through CV measurements under light and dark conditions. As shown in Figure 72, even under illumination, the linearly graded junction must be considered, given the value of $\beta = \frac{1}{3.06}$. Linearly interpolating the data presented in Figure 73a/b in the negative bias region, a built-in potential of (0.53 ± 0.05) V and (0.82 ± 0.05) V is obtained under light and dark conditions respectively. Classical theory contradicts what we just observed, since these two values should coincide. This measurement also suggests the presence of an illumination-related potential. In fact, adding the value of approximately 0.3 V, related to the junction barrier due to hole accumulation, to Φ_{BI} under light, a value close to the built-in potential under dark conditions is obtained. This confirms that the term enclosed in square brackets on the left-hand side of the Δ relation is strongly influenced by the charge generation rate, g.

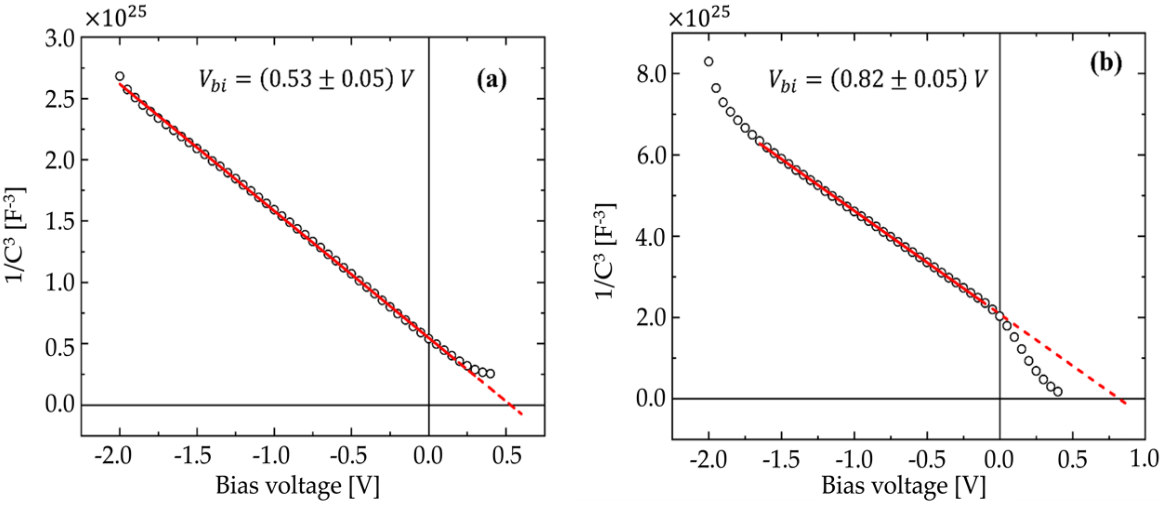

Figure 73. *Graph of $1/C^3$ as a function of bias voltage: (a) under illumination, (b) in dark conditions.*

To summarize, this chapter studied the anomalous behaviour of the solar cell with a heterojunction between ZnCdS and Sb_2Se_3. The kink phenomenon is attributable to an accumulation of holes (positive charges) in the junction region, which occurs due to an imperfect alignment of the energy bands between the two materials forming the junction. Conversely, the crossover could be due to a low built-in potential caused by a limited number of holes within Sb_2Se_3. Finally, the CV measurements show that the junction region is not sharp but presents a linear charge distribution.

FUTURE PERSPECTIVE AND PRELIMINARY RESULTS

From this work it is clear that, to achieve high efficiency Sb_2Se_3-based solar cells need to optimize the interactions between antimony selenide and the window layer on which it grows, from the perspective of CBO and intermixing layer. This could reduce the high defect density at the interface and also within the antimony selenide layer. Another issue affecting the device's performance is the limited density of free holes within Sb_2Se_3, which is only an order of magnitude higher than the defect density. This drawback can be overcome by exploring p-type doping methods, introducing extrinsic atoms into the crystalline matrix of antimony selenide, such as tin.

Preliminary doping studies using the diffusion of tin atoms have been performed. After growing Sb_2Se_3 by CSS, a thin layer of tin was deposited on it using the sputtering technique. Tests were performed by varying the thickness of the Sn layer deposited at different temperatures, with the aim of increasing the surface mobility of Sb_2Se_3 atoms, in order to facilitate the diffusion of Sn atoms inside its grains.

Table 7. *Photovoltaic parameters extracted from the J-V curves in figure 74.*

#	Thickness [Å]	T_{sub} [°C]	V_{oc} [mV]	J_{sc} [mA/cm^2]	R_s [Ωcm^2]	R_{sh} [Ωcm^2]	FF	PCE [%]
494	5	260	473	35.4	2.45	134.4	0.50	8.4
495	5	300	426	23.4	2.49	156.0	0.51	5.1
496	3	260	457	25.4	2.28	189.4	0.55	6.3
498	3	330	354	16.3	1.58	142.7	0.49	2.8

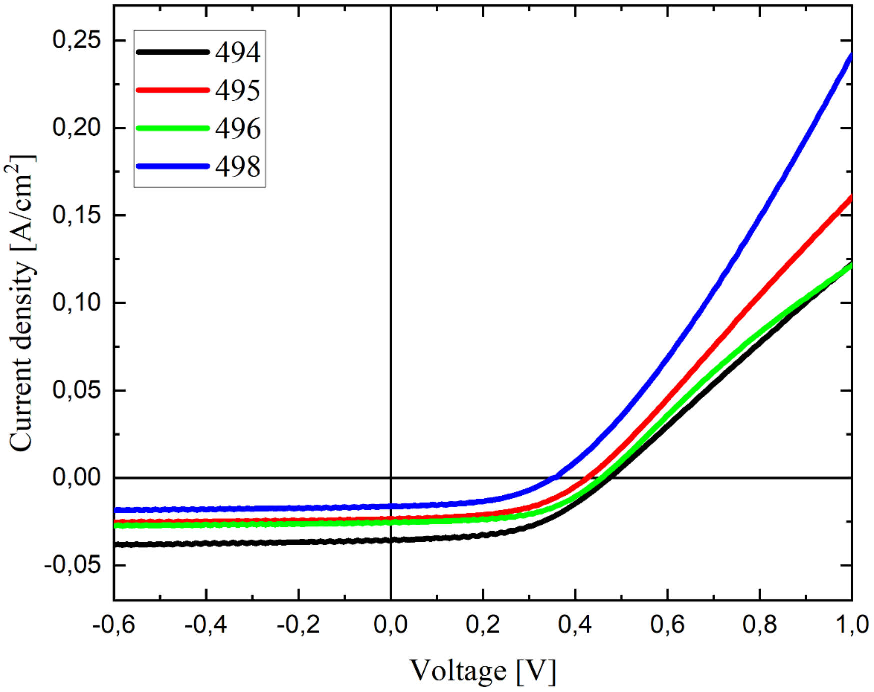

Figure 74. *J-V characteristics of* Sb_2Se_3*-based solar cell, varying the thickness of tin and substrate temperature. The incident power light was 1000 W/m*^{2} *. The area of the solar cells is 0.11 cm*^{2}*.*

Table 7 shows the photovoltaic parameters that refers to the J-V curves shown in figure 74. The table provide evidence that small variation in the Sn layer and temperature result in significant changes to the photovoltaic parameters. In particular, sample number 494 exhibit a higher PCE value compared to both other doping tests and the standard cell, as shown in the photovoltaic parameters reported in table 6.

A significant increase in J_{sc} is evident. In general, these tests show an increase in photocurrent, which could indicate effective p-type doping of the antimony selenide. However, there is also a significant reduction in shunt resistance. One hypothesis to explain the decrease in R_{sh} is that the metals potentially doping the antimony selenide exhibit a partition coefficient between what enters the grain (contributing to effective doping) and what remains at the grain boundary. Grain boundaries typically have very high diffusion coefficient, allowing metal atoms to migrate easily to the junction, partially short-circuiting it. This phenomenon is macroscopically observed as a decrease in shunt resistance.

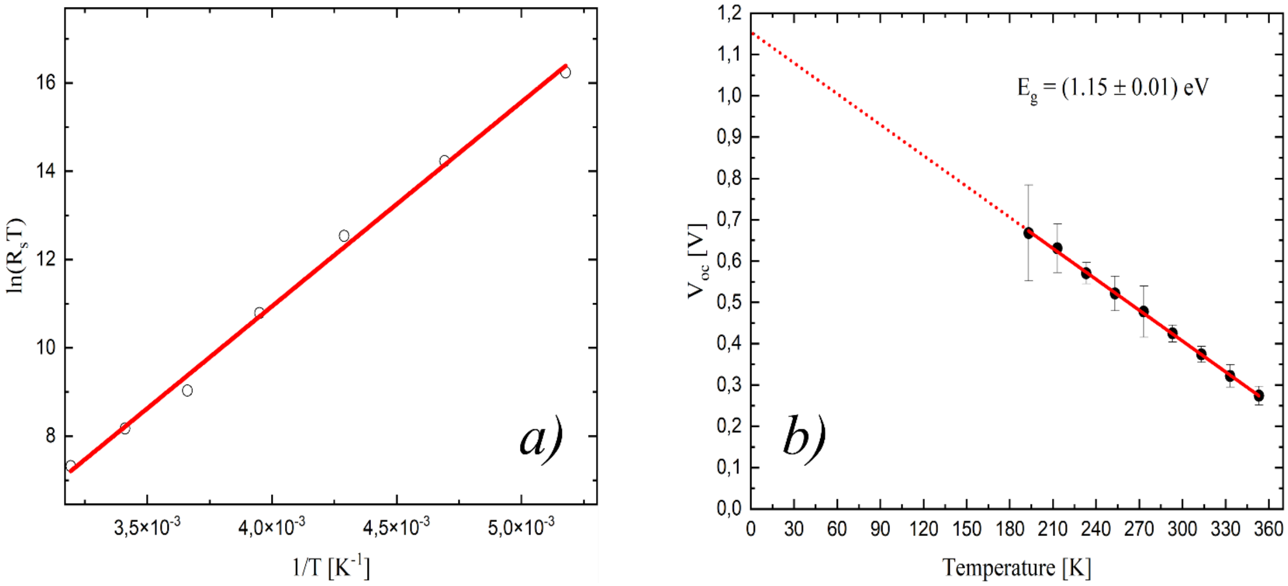

Figure 75. *a) Plot of ln(R_ST) [unit: Ωcm^2K]vs 1/T and in red line is reported the linear fit; b) is reported the V_{oc} dependence on the temperature.*

J-V measurements under light at different temperatures were conducted to assess whether there was any variation in the potential barrier compared to the case studied in Chapter 6.1. As in the previous case, the barrier height was determined from the linear fit of ln(R_ST) vs 1/T (figure 75a), yielding a value of (399 ± 10) meV. The barrier height increased for the Sb_2Se_3 solar cell nominally doped with tin. This result further suggests that, at least partially, the antimony selenide grains underwent effective p-type doping, as an increase in the energy barrier at the heterojunction interface indicates a rise in hole density within the antimony selenide. In fact, CBO, in this case between ZnCdS and Sb_2Se_3, is influenced by the doping level, which increased in antimony selenide thin film.

Observing the variation of V_{oc} as a function of temperature (figure 75b), no saturation of the open-circuit voltage is noticed at low temperatures. In the presence of an energy barrier, which acts as a reverse-biased junction relative to the main one, a decrease in V_{oc} would typically be expected. However, this decrease is not observed, despite the estimated increase in the energy barrier compared to the case described in Chapter 6. This suggests that the energy barrier has narrowed sufficiently to allow holes to pass through via tunnelling, without being trapped at the heterojunction interface. Notably, the J-V characteristic of cell 494 does not show any kink in the first quadrant, indicating that, at a macroscopic level, the barrier does not significantly affect the device operation.

Furthermore, from the relationship [182,183]:

$$V_{oc} \propto \frac{E_g}{q} - \frac{KT}{q} \ln{(const)} \tag{7-1}$$

it is also possible to determine the energy gap of antimony selenide, which is found to be (1.15 ± 0.01) eV.

To gain a deeper understanding of this phenomenon, further in-depth experiments are required.

Another crucial aspect for improving the device's performance is optimizing the preferential growth of Sb_2Se_3 grains along the (002) plane. This can be achieved by exploring alternative window layers (e.g. Zn(S,O), TiO_2, MgO_2, Cd_2SnO_4, and others) that are cadmium-free, environmentally friendly, and offer greater transparency in the solar spectrum region where antimony selenide effectively absorb photons.

CONCLUSIONS

In this PhD thesis, antimony selenide was explored as a groundbreaking material for thin-film solar cells that offers a promising alternative to conventional CdTe and CIGS technologies, which rely on toxic and scarce materials. Sb_2Se_3 stands out not only for its environmental benefits but also for its compatibility with scalable and cost-effective fabrication methods, such as sputtering and close-spaced sublimation. Unlike chemical-based techniques, these deposition processes eliminate the need for hazardous solutions and prevent chemical waste.

In recent years, the photovoltaic conversion efficiency of Sb_2Se_3 solar cells has exceeded the 10% efficiency threshold, sparking growing optimism for the future of chalcogenide-based solar technology. The unique sustainability and excellent physical-chemical properties of Sb_2Se_3 position it as a leading candidate for large-scale photovoltaic applications.

One of the most intriguing characteristics of Sb_2Se_3 is its highly asymmetric crystalline structure, defined by its quasi-1D ribbon-like configuration. This distinctive structure optimizes electrical conduction when Sb_2Se_3 grains align along the ribbons' growth axis (the c-axis). However, the material growth is highly dependent on the substrate, with stronger substrate interactions driving growth along the less favourable [100] direction. Our experiments revealed that substrates composed of CdS+ZnCdS promote preferential grain growth along the desirable (002) plane, corresponding to the [001] direction. Analysis of J-V characteristics showed a clear relationship between the short-circuit current density (J_{sc}) and the texture coefficient (TC) for the (002) plane, with J_{sc} increasing as the $TC_{(002)}$ value rises. Other window layers, however, exhibited a less favourable grain orientation, hence negatively impacting photovoltaic performance.

While V_{oc} and fill factor (FF) are influenced by trap density in the Sb_2Se_3 film, preventing a clear correlation with $TC_{(002)}$, our study highlights the importance of reducing defects to improve these parameters. Additionally, the role of a hole transport layer (HTL) between the absorber and metal contact was confirmed to be essential for long-term device stability. By preventing metal atom diffusion and enabling the use of cost-effective metals (e.g., Mo or Ni-V alloys) instead of gold, the HTL preserves the ohmic nature of the contact without sacrificing performance.

In the course of this thesis, a novel Fe-S-O layer was introduced and tested as an ohmic back contact for Sb_2Se_3 solar cells. This polycrystalline film, composed of cubic and orthorhombic Fe_3O_4 and hexagonal $Fe_{(1-x)}S$, was deposited by RF sputtering at high temperatures. Films deposited at room temperature were found to be amorphous. When incorporated as back contacts, these films demonstrated linear ohmic behaviour with a contact resistivity of about 0.8 $\Omega\cdot cm^2$, a promising result for this type of solar cell.

Furthermore, our study of the heterojunction properties revealed a kink in the J-V characteristic, explained by the presence of an energy barrier at the interface, caused by charge accumulation due to imperfect band alignment. Furthermore, the comparison between light and dark conditions revealed a crossover of the relevant J-V curves, indicative of differences in built-in potential. Finally, capacitance-voltage (CV) measurements suggested that the interface between ZnCdS and Sb_2Se_3 is not sharp but instead shows a linear charge distribution, possibly due to an intermixing layer that helps accommodate the lattice mismatch between the two materials.

Considering the obtained results, several avenues can be pursued in the future to further enhance the performance and scalability of Sb_2Se_3-based solar cells:

- Minimize defects and trap densities: A key challenge observed was the influence of trap densities on photovoltaic parameters such as V_{oc} and fill factor (FF). Future research could focus on defect passivation strategies, such as optimizing the deposition conditions, introducing passivating layers, or doping with elements that reduce the density of traps in the Sb_2Se_3 film.

- Develop advanced Window Layers: While CdS+ZnCdS proved effective in promoting favourable grain orientation, future studies could explore new cadmium-free, environmentally friendly window layers that provide better band alignment and transparency. Materials like Zn(S,O), ZnMgO, TiO_2, or other oxides could be optimized to further enhance device efficiency and sustainability.

- Explore alternative back contacts: The Fe-S-O layer demonstrated promising ohmic behaviour, but additional materials could be investigated to improve contact resistivity and stability further. Developing back contact materials that are more cost-effective and offer better performance could significantly enhance the viability of Sb_2Se_3 solar cells for large-scale production.

- Improve band alignment at the heterojunction: The energy barrier observed at the ZnCdS/ Sb_2Se_3 interface highlights the importance of achieving proper band alignment. Future work could explore different window layer/absorber combinations, interface engineering techniques, or interfacial treatments to reduce this barrier and prevent charge accumulation.

- Scale Up Production Methods: While this research utilized scalable fabrication techniques like sputtering and CSS, further refinement of these processes is necessary to improve the uniformity, reproducibility, and cost-efficiency of Sb_2Se_3 solar cells. Exploring alternative deposition methods that maintain high quality while being faster and more economical would be crucial for industrial adoption.

- Investigate Stability and Durability: Long-term stability is essential for the commercialization of any solar technology. Future work could focus on studying the environmental stability of Sb_2Se_3 cells, including their resistance to moisture, oxygen, and temperature fluctuations, as well as exploring encapsulation methods to protect the device over time.

- Enhance Efficiency Beyond 10%: Although the efficiency of Sb_2Se_3 cells has surpassed 10%, there is significant potential for further improvement. This can be achieved through more precise control over film thickness, grain size, and orientation, as well as the incorporation of light-trapping structures to enhance photon absorption.

By addressing these areas, Sb_2Se_3 could become a leading material in the next generation of thin-film solar cells, thus offering a sustainable, efficient, and scalable solution to meet global energy demands.

REFERENCES

[1] World Energy Outlook 2022, n.d. www.iea.org/t&c/.

[2] J. Ramanujam, A. Verma, B. González-Díaz, R. Guerrero-Lemus, C. Del Cañizo, E. García-Tabarés, I. Rey-Stolle, F. Granek, L. Korte, M. Tucci, J. Rath, U.P. Singh, T. Todorov, O. Gunawan, S. Rubio, J.L. Plaza, E. Diéguez, B. Hoffmann, S. Christiansen, G.E. Cirlin, Inorganic photovoltaics - Planar and nanostructured devices, Prog Mater Sci 82 (2016) 294–404. https://doi.org/10.1016/j.pmatsci.2016.03.005.

[3] M. Grätzel, Solar Energy Conversion by Dye-Sensitized Photovoltaic Cells, Inorg Chem 44 (2005) 6841–6851. https://doi.org/10.1021/ic0508371.

[4] W. Shockley, H.J. Queisser, Detailed Balance Limit of Efficiency of p-n Junction Solar Cells, J Appl Phys 32 (1961) 510. https://doi.org/10.1063/1.1736034.

[5] https://www.nrel.gov/pv/assets/pdfs/cell-pv-eff-crysi.pdf, NREL Transforming Energy, 23/12/2022 (n.d.).

[6] B.R. Bathey, M.C. Cretella, Solar-grade silicon, J Mater Sci 17 (1982) 3077–3096. https://doi.org/10.1007/BF01203469.

[7] C.-W. Lan, C.-K. Hsieh, W.-C. Hsu, Czochralski Silicon Crystal Growth for Photovoltaic Applications, in: N. Nakajima Kazuo and Usami (Ed.), Crystal Growth of Si for Solar Cells, Springer Berlin Heidelberg, Berlin, Heidelberg, 2009: pp. 25–39. https://doi.org/10.1007/978-3-642-02044-5_2.

[8] M. Li, Y. Dai, W. Ma, B. Yang, Q. Chu, Review of New Technology for Preparing Crystalline Silicon Solar Cell Materials by Metallurgical Method, IOP Conf Ser Earth Environ Sci 94 (2017) 012016. https://doi.org/10.1088/1755-1315/94/1/012016.

[9] Robert Hull, Properties of Crystalline Silicon, IET, 1999.

[10] M. Stuckelberger, R. Biron, N. Wyrsch, F.-J. Haug, C. Ballif, Review: Progress in solar cells from hydrogenated amorphous silicon, Renewable and Sustainable Energy Reviews 76 (2017) 1497–1523. https://doi.org/https://doi.org/10.1016/j.rser.2016.11.190.

[11] B. Rech, H. Wagner, Potential of amorphous silicon for solar cells, Applied Physics A 69 (1999) 155–167. https://doi.org/10.1007/s003390050986.

[12] D.E. Carlson, C.R. Wronski, Amorphous silicon solar cell, Appl Phys Lett 28 (2008) 671–673. https://doi.org/10.1063/1.88617.

[13] W.D. Gill, R.H. Bube, Photovoltaic Properties of Cu_2S-CdS Heterojunctions, J Appl Phys 41 (1970) 3731–3738. https://doi.org/10.1063/1.1659500.

[14] W.E. Devaney, A.M. Barnett, G.M. Storti, J.D. Meakin, The design and fabrication of CdS/Cu_2S cells of 8.5-percent conversion efficiency, IEEE Trans Electron Devices 26 (1979) 205–210. https://doi.org/10.1109/T-ED.1979.19405.

[15] A. Bosio, S. Pasini, N. Romeo, The History of Photovoltaics with Emphasis on CdTe Solar Cells and Modules, Coatings 10 (2020) 344. https://doi.org/10.3390/coatings10040344.

[16] M.A. Green, E.D. Dunlop, J. Hohl-Ebinger, M. Yoshita, N. Kopidakis, K. Bothe, D. Hinken, M. Rauer, X. Hao, Solar cell efficiency tables (Version 60), (2022). https://doi.org/10.1002/pip.3595.

[17] V.M. Fthenakis, A.O. Bulawka, Photovoltaics, Environmental Impact of, Encyclopedia of Energy (2004) 61–69. https://doi.org/10.1016/B0-12-176480-X/00421-6.

[18] N. Selmane, A. Cheknane, F. Khemloul, M.H.S. Helal, H.S. Hilal, Cost-saving and performance-enhancement of CuInGaSe solar cells by adding CuZnSnSe as a second absorber, Solar Energy 234 (2022) 64–80. https://doi.org/https://doi.org/10.1016/j.solener.2022.01.072.

[19] X. Zhang, W. Xu, S. Wang, D. Liu, P. Deng, J. Deng, W. Jiang, Research Status of Recovery of Tellurium from Cadmium Telluride Photovoltaic Modules, IOP Conf Ser Mater Sci Eng 782 (2020) 022024. https://doi.org/10.1088/1757-899X/782/2/022024.

[20] IT IT COMMISSIONE EUROPEA Bruxelles, 3.9.2020 COM(2020) 474 final COMUNICAZIONE DELLA COMMISSIONE AL PARLAMENTO EUROPEO, AL CONSIGLIO, AL COMITATO ECONOMICO E SOCIALE EUROPEO E AL COMITATO DELLE REGIONI Resilienza delle materie prime critiche: tracciare un percorso verso una maggiore sicurezza e sostenibilità, n.d.

[21] E. Commission, Written by Deloitte Sustainability British Geological Survey Bureau de Recherches Géologiques et Minières Netherlands Organisation for Applied Scientific Research Study on the review of the list of Critical Raw Materials Criticality Assessments, 2017.

[22] A. Le Donne, V. Trifiletti, S. Binetti, New earth-abundant thin film solar cells based on chalcogenides, Front Chem 7 (2019). https://doi.org/10.3389/fchem.2019.00297.

[23] S. Rampino, F. Pattini, M. Bronzoni, M. Mazzer, M. Sidoli, G. Spaggiari, E. Gilioli, CuSbSe2 thin film solar cells with ~4% conversion efficiency grown by low-temperature pulsed electron deposition, Solar Energy Materials and Solar Cells 185 (2018) 86–96. https://doi.org/10.1016/j.solmat.2018.05.024.

[24] S. Banu, S.J. Ahn, S.K. Ahn, K. Yoon, A. Cho, Fabrication and characterization of cost-efficient CuSbS2 thin film solar cells using hybrid inks, Solar Energy Materials and Solar Cells 151 (2016) 14–23. https://doi.org/10.1016/j.solmat.2016.02.013.

[25] Y.C. Choi, D.U. Lee, J.H. Noh, E.K. Kim, S. Il Seok, Highly Improved Sb_2S_3 Sensitized-Inorganic-Organic Heterojunction Solar Cells and Quantification of Traps by Deep-Level Transient Spectroscopy, Adv Funct Mater 24 (2014) 3587–3592. https://doi.org/10.1002/adfm.201304238.

[26] Y. Zhao, S. Wang, C. Jiang, C. Li, P. Xiao, R. Tang, J. Gong, G. Chen, T. Chen, J. Li, X. Xiao, Regulating Energy Band Alignment via Alkaline Metal Fluoride Assisted Solution Post-Treatment Enabling Sb2(S,Se)3 Solar Cells with 10.7% Efficiency, Adv Energy Mater 12 (2022). https://doi.org/10.1002/aenm.202103015.

[27] C. Chen, K. Li, J. Tang, Ten Years of Sb2Se3 Thin Film Solar Cells, Solar RRL 6 (2022) 2200094. https://doi.org/https://doi.org/10.1002/solr.202200094.

[28] S. Khalid, E. Ahmed, Y. Khan, K.N. Riaz, M.A. Malik, Nanocrystalline Pyrite for Photovoltaic Applications, ChemistrySelect 3 (2018) 6488–6524. https://doi.org/https://doi.org/10.1002/slct.201800405.

[29] U.S. Geological Survey, Mineral commodity summaries 2022, 2022. https://doi.org/10.3133/mcs2022.

[30] Y. Zhao, S. Wang, C. Li, B. Che, X. Chen, H. Chen, R. Tang, X. Wang, G. Chen, T. Wang, J. Gong, T. Chen, X. Xiao, J. Li, Regulating deposition kinetics via a novel additive-assisted chemical bath deposition technology enables fabrication of 10.57%-efficiency Sb2Se3 solar cells, Energy Environ Sci 15 (2022) 5118–5128. https://doi.org/10.1039/d2ee02261c.

[31] E. Barrios-Salgado, M.T.S. Nair, P.K. Nair, R.A. Zingaro, Chemically deposited thin films of PbSe as an absorber component in solar cell structures, Thin Solid Films 519 (2011) 7432–7437. https://doi.org/10.1016/j.tsf.2010.12.226.

[32] M. Leng, M. Luo, C. Chen, S. Qin, J. Chen, J. Zhong, J. Tang, Selenization of Sb_2Se_3 absorber layer: An efficient step to improve device performance of CdS/Sb $_2$ Se $_3$ solar cells, Appl Phys Lett 105 (2014) 083905. https://doi.org/10.1063/1.4894170.

[33] Y. Zhou, L. Wang, S. Chen, S. Qin, X. Liu, J. Chen, D.-J. Xue, M. Luo, Y. Cao, Y. Cheng, E.H. Sargent, J. Tang, Thin-film Sb_2Se_3 photovoltaics with oriented one-dimensional ribbons and benign grain boundaries, Nat Photonics 9 (2015) 409–415. https://doi.org/10.1038/nphoton.2015.78.

[34] C. Chen, L. Wang, L. Gao, D. Nam, D. Li, K. Li, Y. Zhao, C. Ge, H. Cheong, H. Liu, H. Song, J. Tang, 6.5% Certified Efficiency Sb2Se3 Solar Cells Using PbS Colloidal Quantum Dot Film as Hole-Transporting Layer, ACS Energy Lett 2 (2017) 2125–2132. https://doi.org/10.1021/acsenergylett.7b00648.

[35] Z. Li, X. Liang, G. Li, H. Liu, H. Zhang, J. Guo, J. Chen, K. Shen, X. San, W. Yu, R.E.I. Schropp, Y. Mai, 9.2%-efficient core-shell structured antimony selenide nanorod array solar cells, Nat Commun 10 (2019). https://doi.org/10.1038/s41467-018-07903-6.

[36] Z. Duan, X. Liang, Y. Feng, H. Ma, B. Liang, Y. Wang, S. Luo, S. Wang, R.E.I. Schropp, Y. Mai, Z. Li, Sb_2Se_3 Thin-Film Solar Cells Exceeding 10% Power Conversion Efficiency Enabled by Injection Vapor Deposition Technology, Advanced Materials 34 (2022). https://doi.org/10.1002/adma.202202969.

[37] K.-J. Hsiao, J.-D. Liu, H.-H. Hsieh, T.-S. Jiang, Electrical impact of $MoSe_2$ on CIGS thin-film solar cells, Physical Chemistry Chemical Physics 15 (2013) 18174. https://doi.org/10.1039/c3cp53310g.

[38] S. Ramírez-Velasco, J.R. González-Castillo, F. Ayala-Mató, V. Hernández-Calderón, D. Jiménez-Olarte, O. Vigil-Galán, Back contact modification in Sb2Se3 solar cells: The effect of a thin layer of MoSe2, Thin Solid Films 751 (2022) 139227. https://doi.org/https://doi.org/10.1016/j.tsf.2022.139227.

[39] Y. Luo, G. Chen, S. Chen, N. Ahmad, M. Azam, Z. Zheng, Z. Su, M. Cathelinaud, H. Ma, Z. Chen, P. Fan, X. Zhang, G. Liang, Carrier Transport Enhancement Mechanism in Highly Efficient Antimony Selenide Thin-Film Solar Cell, Adv Funct Mater (2023). https://doi.org/10.1002/adfm.202213941.

[40] S. Li, H. Shen, J. Chen, Y. Jiang, L. Sun, A. Raza, Y. Xu, Effect of selenization temperature on the properties of Sb_2Se_3 thin films and solar cells by two-step method, Journal of Materials Science: Materials in Electronics 30 (2019) 19871–19879. https://doi.org/10.1007/s10854-019-02354-1.

[41] R. Tang, S. Chen, Z.H. Zheng, Z.H. Su, J.T. Luo, P. Fan, X.H. Zhang, J. Tang, G.X. Liang, Heterojunction Annealing Enabling Record Open-Circuit Voltage in Antimony Triselenide Solar Cells, Advanced Materials 34 (2022). https://doi.org/10.1002/adma.202109078.

[42] A. Amin, D. Li, X. Duan, S.N. Vijayaraghavan, H.G. Menon, J. Wall, M. Weaver, M.M. Cheng, Y. Zheng, L. Li, F. Yan, Enhanced Efficiency and Stability in Sb_2S_3 Seed Layer Buffered Sb_2Se_3 Solar Cells, Adv Mater Interfaces 9 (2022) 2200547. https://doi.org/10.1002/admi.202200547.

[43] L.J. Phillips, O.S. Hutter, T. Baines, L. Bowen, L.J. Phillips, P. Yates, K. Durose, J.D. Major, Close-Spaced Sublimation for Sb2Se3 Solar Cells Close-Spaced Sublimation for Sb 2 Se 3 Solar Cells, 2017. https://www.researchgate.net/publication/318495290.

[44] S. Pasini, D. Spoltore, A. Parisini, S. Marchionna, L. Fornasini, D. Bersani, R. Fornari, A. Bosio, Innovative back-contact for Sb2Se3 -based thin film solar cells, Solar Energy 249 (2023) 414–423. https://doi.org/10.1016/j.solener.2022.11.049.

[45] J. Zhang, R. Kondrotas, S. Lu, C. Wang, C. Chen, J. Tang, Alternative back contacts for Sb2Se3 solar cells, Solar Energy 182 (2019) 96–101. https://doi.org/10.1016/J.SOLENER.2019.02.050.

[46] C. Liu, K. Shen, D. Lin, Y. Cao, S. Qiu, J. Zheng, F. Bao, Y. Gao, H. Zhu, Z. Li, Y. Mai, Back Contact Interfacial Modification in Highly-Efficient All-Inorganic Planar n-i-p Sb2Se3 Solar Cells, ACS Appl Mater Interfaces 12 (2020) 38397–38405. https://doi.org/10.1021/acsami.0c10629.

[47] L. Lin, L. Jiang, Y. Qiu, B. Fan, Analysis of Sb2Se3/CdS based photovoltaic cell: A numerical simulation approach, Journal of Physics and Chemistry of Solids 122 (2018) 19–24. https://doi.org/https://doi.org/10.1016/j.jpcs.2018.05.045.

[48] L. Zhang, Y. Li, C. Li, Q. Chen, Z. Zhen, X. Jiang, M. Zhong, F. Zhang, H. Zhu, Scalable Low-Band-Gap Sb2Se3 Thin-Film Photocathodes for Efficient Visible–Near-Infrared Solar Hydrogen Evolution, ACS Nano 11 (2017) 12753–12763. https://doi.org/10.1021/acsnano.7b07512.

[49] Y. Wang, S. Ji, B. Shin, Interface engineering of antimony selenide solar cells: a review on the optimization of energy band alignments, JPhys Energy 4 (2022). https://doi.org/10.1088/2515-7655/ac8578.

[50] G. Li, Z. Li, X. Liang, C. Guo, K. Shen, Y. Mai, Improvement in Sb2Se3 Solar Cell Efficiency through Band Alignment Engineering at the Buffer/Absorber Interface, ACS Appl Mater Interfaces 11 (2019) 828–834. https://doi.org/10.1021/acsami.8b17611.

[51] L. Wang, D.-B. Li, K. Li, C. Chen, H.-X. Deng, L. Gao, Y. Zhao, F. Jiang, L. Li, F. Huang, Y. He, H. Song, G. Niu, J. Tang, Stable 6%-efficient Sb2Se3 solar cells with a ZnO buffer layer, Nat Energy 2 (2017) 17046. https://doi.org/10.1038/nenergy.2017.46.

[52] K. Li, R. Kondrotas, C. Chen, S. Lu, X. Wen, D. Li, J. Luo, Y. Zhao, J. Tang, Improved efficiency by insertion of $Zn_{1-x}Mg_xO$ through sol-gel method in ZnO/Sb_2Se_3 solar cell, Solar Energy 167 (2018) 10–17. https://doi.org/10.1016/j.solener.2018.03.081.

[53] J. Zhou, X. Zhang, H. Chen, Z. Tang, D. Meng, K. Chi, Y. Cai, G. Song, Y. Cao, Z. Hu, Dual-function of $CdCl_2$ treated SnO_2 in Sb_2Se_3 solar cells, Appl Surf Sci 534 (2020) 147632. https://doi.org/10.1016/j.apsusc.2020.147632.

[54] K. Li, C. Chen, S. Lu, C. Wang, S. Wang, Y. Lu, J. Tang, Orientation Engineering in Low-Dimensional Crystal-Structural Materials via Seed Screening., Adv Mater 31 (2019) e1903914. https://doi.org/10.1002/adma.201903914.

[55] R. Jakomin, S. Rampino, G. Spaggiari, F. Pattini, Advances on Sb2Se3 Solar Cells Fabricated by Physical Vapor Deposition Techniques, Solar 3 (2023) 566–595. https://doi.org/10.3390/solar3040031.

[56] S. Lu, H. Ding, J. Hu, Y. Liu, J. Zhu, R. Kondrotas, C. Chen, J. Tang, In situ investigation of interfacial properties of Sb2Se3 heterojunctions, Appl Phys Lett 116 (2020) 241602. https://doi.org/10.1063/5.0008879.

[57] A. Bosio, G. Foti, S. Pasini, D. Spoltore, A Review on the Fundamental Properties of Sb2Se3-Based Thin Film Solar Cells, Energies (Basel) 16 (2023). https://doi.org/10.3390/en16196862.

[58] S. Chakrabarti, P. Banerjee, P. Mitra, A. Roy, Zinc oxide–based nanomaterials for environmental applications, Handbook of Smart Photocatalytic Materials: Environment, Energy, Emerging Applications and Sustainability (2020) 73–107. https://doi.org/10.1016/B978-0-12-819049-4.00009-X.

[59] K. Yang, B. Li, G. Zeng, Effects of substrate temperature and SnO_2 high resistive layer on Sb_2Se_3 thin film solar cells prepared by pulsed laser deposition, Solar Energy Materials and Solar Cells 208 (2020) 110381. https://doi.org/10.1016/j.solmat.2019.110381.

[60] F. Pattini, S. Rampino, F. Mezzadri, D. Calestani, G. Spaggiari, M. Sidoli, D. Delmonte, A. Sala, E. Gilioli, M. Mazzer, Role of the substrates in the ribbon orientation of Sb2Se3 films grown by Low-Temperature Pulsed Electron Deposition, Solar Energy Materials and Solar Cells 218 (2020) 110724. https://doi.org/https://doi.org/10.1016/j.solmat.2020.110724.

[61] R. Guerrero-Lemus, R. Vega, T. Kim, A. Kimm, L.E. Shephard, Bifacial solar photovoltaics – A technology review, Renewable and Sustainable Energy Reviews 60 (2016) 1533–1549. https://doi.org/https://doi.org/10.1016/j.rser.2016.03.041.

[62] K.J. Tiwari, M. Neuschitzer, M. Espíndola-Rodriguez, Y. Sánchez, Z. Jehl, P. Vidal-Fuentes, E. Saucedo, P. Malar, Efficient Sb_2Se_3/CdS planar heterojunction solar cells in substrate configuration with (hk0) oriented Sb_2Se_3 thin films, Solar Energy Materials and Solar Cells 215 (2020) 110603. https://doi.org/10.1016/j.solmat.2020.110603.

[63] Z. Li, X. Chen, H. Zhu, J. Chen, Y. Guo, C. Zhang, W. Zhang, X. Niu, Y. Mai, Sb_2Se_3 thin film solar cells in substrate configuration and the back contact selenization, Solar Energy Materials and Solar Cells 161 (2017) 190–196. https://doi.org/10.1016/j.solmat.2016.11.033.

[64] I. Caño, P. Vidal-Fuentes, L. Calvo-Barrio, X. Alcobé, J.M. Asensi, S. Giraldo, Y. Sánchez, Z. Jehl, M. Placidi, J. Puigdollers, V. Izquierdo-Roca, E. Saucedo, Does Sb2Se3 Admit Nonstoichiometric Conditions? How Modifying the Overall Se Content Affects the Structural, Optical, and Optoelectronic Properties of Sb2Se3 Thin Films, ACS Appl Mater Interfaces 14 (2022) 11222–11234. https://doi.org/10.1021/acsami.1c20764.

[65] X. Wen, C. Chen, S. Lu, K. Li, R. Kondrotas, Y. Zhao, W. Chen, L. Gao, C. Wang, J. Zhang, G. Niu, J. Tang, Vapor transport deposition of antimony selenide thin film solar cells with 7.6% efficiency, (n.d.). https://doi.org/10.1038/s41467-018-04634-6.

[66] C. Wu, L. Zhang, H. Ding, H. Ju, X. Jin, X. Wang, C. Zhu, T. Chen, Direct solution deposition of device quality $Sb_2S_{3-x}Se_x$ films for high efficiency solar cells, Solar Energy Materials and Solar Cells 183 (2018) 52–58. https://doi.org/10.1016/j.solmat.2018.04.009.

[67] R. Tang, X. Chen, Y. Luo, Z. Chen, Y. Liu, Y. Li, Z. Su, X. Zhang, P. Fan, G. Liang, Controlled Sputtering Pressure on High-Quality Sb_2Se_3 Thin Film for Substrate Configurated Solar Cells, Nanomaterials 10 (2020) 574. https://doi.org/10.3390/nano10030574.

[68] N.W. Tideswell, F.H. Kruse, J.D. McCullough, The crystal structure of antimony selenide, Sb_2Se_3, Acta Crystallogr 10 (1957) 99–102. https://doi.org/10.1107/S0365110X57000298.

[69] G.P. Voutsas, A.G. Papazoglou, P.J. Rentzeperis, D. Siapkas, The crystal structure of antimony selenide, Sb_2Se_3, Z Kristallogr Cryst Mater 171 (1985) 261–268. https://doi.org/10.1524/zkri.1985.171.14.261.

[70] T.D.C. Hobson, O.S. Hutter, M. Birkett, T.D. Veal, K. Durose, Growth and Characterization of Sb 2 Se 3 Single Crystals for Fundamental Studies, n.d.

[71] K. Momma, F. Izumi, VESTA3 for three-dimensional visualization of crystal, volumetric and morphology data, J Appl Crystallogr 44 (2011) 1272–1276. https://doi.org/10.1107/S0021889811038970.

[72] A. Mavlonov, T. Razykov, F. Raziq, J. Gan, J. Chantana, Y. Kawano, T. Nishimura, H. Wei, A. Zakutayev, T. Minemoto, X. Zu, S. Li, L. Qiao, A review of Sb2Se3 photovoltaic absorber materials and thin-film solar cells, Solar Energy 201 (2020) 227–246. https://doi.org/10.1016/j.solener.2020.03.009.

[73] G.P. Voutsas, A.G. Papazoglou, P.J. Rentzeperis, D. Siapkas, The crystal structure of antimony selenide, Sb_2Se_3, Z Kristallogr Cryst Mater 171 (1985) 261–268. https://doi.org/10.1524/zkri.1985.171.14.261.

[74] G. Liang, M. Chen, M. Ishaq, X. Li, R. Tang, Z. Zheng, Z. Su, P. Fan, X. Zhang, S. Chen, Crystal Growth Promotion and Defects Healing Enable Minimum Open-Circuit Voltage Deficit in Antimony Selenide Solar Cells, Advanced Science 9 (2022) 2105142. https://doi.org/10.1002/advs.202105142.

[75] R. Tang, Z.H. Zheng, Z.H. Su, X.J. Li, Y.D. Wei, X.H. Zhang, Y.Q. Fu, J.T. Luo, P. Fan, G.X. Liang, Highly efficient and stable planar heterojunction solar cell based on sputtered and post-selenized Sb2Se3 thin film, Nano Energy 64 (2019). https://doi.org/10.1016/j.nanoen.2019.103929.

[76] A. Stoliaroff, A. Lecomte, O. Rubel, S. Jobic, X. Zhang, C. Latouche, X. Rocquefelte, Deciphering the Role of Key Defects in Sb_2Se_3, a Promising Candidate for Chalcogenide-Based Solar Cells, ACS Appl Energy Mater 3 (2020) 2496–2509. https://doi.org/10.1021/acsaem.9b02192.

[77] B. Zhang, X. Qian, Competing Superior Electronic Structure and Complex Defect Chemistry in Quasi-One-Dimensional Antimony Chalcogenide Photovoltaic Absorbers, ACS Appl Energy Mater 5 (2022) 492–502. https://doi.org/10.1021/acsaem.1c03023.

[78] X. Wen, C. Chen, S. Lu, K. Li, R. Kondrotas, Y. Zhao, W. Chen, L. Gao, C. Wang, J. Zhang, G. Niu, J. Tang, Vapor transport deposition of antimony selenide thin film solar cells with 7.6% efficiency, Nat Commun 9 (2018). https://doi.org/10.1038/s41467-018-04634-6.

[79] H. Guo, X. Jia, J. Liu, Z. Feng, S. Zhang, Z. Chen, H. Tian, J. Qiu, N. Yuan, J. Ding, Classification of lattice defects and the microscopic origin of p-type conductivity of Sb2Se3 solar cell absorber with varying Al2O3-layer thicknesses, Physica B Condens Matter 648 (2023). https://doi.org/10.1016/j.physb.2022.414394.

[80] C.N. Savory, D.O. Scanlon, The complex defect chemistry of antimony selenide, J Mater Chem A Mater 7 (2019) 10739–10744. https://doi.org/10.1039/c9ta02022e.

[81] U. Wijesinghe, G. Longo, O.S. Hutter, Defect engineering in antimony selenide thin film solar cells, Energy Advances 2 (2023) 12–33. https://doi.org/10.1039/d2ya00232a.

[82] Y. Yan, W.-J. Yin, Y. Wu, T. Shi, N.R. Paudel, C. Li, J. Poplawsky, Z. Wang, J. Moseley, H. Guthrey, H. Moutinho, S.J. Pennycook, M.M. Al-Jassim, Physics of grain boundaries in polycrystalline photovoltaic semiconductors, J Appl Phys 117 (2015) 112807. https://doi.org/10.1063/1.4913833.

[83] D.P. Joshi, D.P. Bhatt, Theory of grain boundary recombination and carrier transport in polycrystalline silicon under optical illumination, IEEE Trans Electron Devices 37 (1990) 237–249. https://doi.org/10.1109/16.43821.

[84] H. Koc, A.M. Mamedov, E. Deligoz, H. Ozisik, First principles prediction of the elastic, electronic, and optical properties of Sb 2S 3 and Sb 2Se 3 compounds, Solid State Sci 14 (2012) 1211–1220. https://doi.org/10.1016/j.solidstatesciences.2012.06.003.

[85] R. Vadapoo, S. Krishnan, H. Yilmaz, C. Marin, Electronic structure of antimony selenide (Sb_2Se_3) from GW calculations, Physica Status Solidi (b) 248 (2011) 700–705. https://doi.org/10.1002/pssb.201046225.

[86] C. Chen, W. Li, Y. Zhou, C. Chen, M. Luo, X. Liu, K. Zeng, B. Yang, C. Zhang, J. Han, J. Tang, Optical properties of amorphous and polycrystalline Sb_2Se_3 thin films prepared by thermal evaporation, Appl Phys Lett 107 (2015) 043905. https://doi.org/10.1063/1.4927741.

[87] Mamta, Y. Singh, K.K. Maurya, V.N. Singh, A review on properties, applications, and deposition techniques of antimony selenide, Solar Energy Materials and Solar Cells 230 (2021) 111223. https://doi.org/https://doi.org/10.1016/j.solmat.2021.111223.

[88] R. Vadapoo, S. Krishnan, H. Yilmaz, C. Marin, Electronic structure of antimony selenide (Sb2Se3) from GW calculations, Physica Status Solidi (b) 248 (2011) 700–705. https://doi.org/https://doi.org/10.1002/pssb.201046225.

[89] P. Fan, G.-J. Chen, S. Chen, Z.-H. Zheng, M. Azam, N. Ahmad, Z.-H. Su, G.-X. Liang, X.-H. Zhang, Z.-G. Chen, Quasi-Vertically Oriented Sb2Se3 Thin-Film Solar Cells with Open-Circuit Voltage Exceeding 500 mV Prepared via Close-Space Sublimation and Selenization, ACS Appl Mater Interfaces 13 (2021) 46671–46680. https://doi.org/10.1021/acsami.1c13223.

[90] J. Dong, Y. Liu, Z. Wang, Y. Zhang, Boosting VOC of antimony chalcogenide solar cells: A review on interfaces and defects, Nano Select 2 (2021) 1818–1848. https://doi.org/https://doi.org/10.1002/nano.202000288.

[91] S. Pasini, D. Spoltore, A. Parisini, G. Foti, S. Marchionna, S. Vantaggio, R. Fornari, A. Bosio, Sb2Se3 Polycrystalline Thin Films Grown on Different Window Layers, Coatings 13 (2023). https://doi.org/10.3390/coatings13020338.

[92] H. Guo, X. Jia, J. Liu, Z. Feng, S. Zhang, Z. Chen, H. Tian, J. Qiu, N. Yuan, J. Ding, Classification of lattice defects and the microscopic origin of p-type conductivity of Sb2Se3 solar cell absorber with varying Al2O3-layer thicknesses, Physica B Condens Matter 648 (2023). https://doi.org/10.1016/j.physb.2022.414394.

[93] X. Wen, Z. Lu, G.-C. Wang, M.A. Washington, T.-M. Lu, Efficient and stable flexible Sb2Se3 thin film solar cells enabled by an epitaxial CdS buffer layer, Nano Energy 85 (2021) 106019. https://doi.org/https://doi.org/10.1016/j.nanoen.2021.106019.

[94] C. Chen, D.C. Bobela, Y. Yang, S. Lu, K. Zeng, C. Ge, B. Yang, L. Gao, Y. Zhao, M.C. Beard, J. Tang, Characterization of basic physical properties of Sb2Se3 and its relevance for photovoltaics, Frontiers of Optoelectronics 10 (2017) 18–30. https://doi.org/10.1007/s12200-017-0702-z.

[95] Y. Zhou, L. Wang, S. Chen, S. Qin, X. Liu, J. Chen, D.-J. Xue, M. Luo, Y. Cao, Y. Cheng, E.H. Sargent, J. Tang, Thin-film Sb2Se3 photovoltaics with oriented one-dimensional ribbons and benign grain boundaries, Nat Photonics 9 (2015) 409–415. https://doi.org/10.1038/nphoton.2015.78.

[96] S.M. Govindharajulu, A.K. Jain, M. Piraviperumal, Tuning the crystalline orientation of quasi 1D anisotropic Sb2Se3 as a function of growth temperature for thin film photovoltaic applications, J Alloys Compd 980 (2024) 173588. https://doi.org/https://doi.org/10.1016/j.jallcom.2024.173588.

[97] Y. Li, Y. Zhou, Y. Zhu, C. Chen, J. Luo, J. Ma, B. Yang, X. Wang, Z. Xia, J. Tang, Characterization of Mg and Fe doped Sb2Se3 thin films for photovoltaic application, Appl Phys Lett 109 (2016) 232104. https://doi.org/10.1063/1.4971388.

[98] Y.H. Kwon, Y.B. Kim, M. Jeong, H.W. Do, H.K. Cho, J.Y. Lee, Crystal growth direction-controlled antimony selenide thin film absorbers produced using an electrochemical approach and intermediate thermal treatment, Solar Energy Materials and Solar Cells 172 (2017) 11–17. https://doi.org/https://doi.org/10.1016/j.solmat.2017.07.004.

[99] D.K. Schroder, Contact Resistance and Schottky Barriers, in: Semiconductor Material and Device Characterization, 2005. https://doi.org/10.1002/0471749095.ch3.

[100] S. Pasini, D. Spoltore, A. Parisini, S. Marchionna, L. Fornasini, D. Bersani, R. Fornari, A. Bosio, Innovative back-contact for Sb2Se3 -based thin film solar cells, Solar Energy 249 (2023) 414–423. https://doi.org/10.1016/j.solener.2022.11.049.

[101] T.D.C. Hobson, H. Shiel, C.N. Savory, J.E.N. Swallow, L.A.H. Jones, T.J. Featherstone, M.J. Smiles, P.K. Thakur, T.-L. Lee, B. Das, C. Leighton, G. Zoppi, V.R. Dhanak, D.O. Scanlon, T.D. Veal, K. Durose, J.D. Major, P-type conductivity in Sn-doped Sb_2Se_3, Journal of Physics: Energy 4 (2022) 045006. https://doi.org/10.1088/2515-7655/ac91a6.

[102] M. Huang, S. Lu, K. Li, Y. Lu, C. Chen, J. Tang, S. Chen, p-Type Antimony Selenide via Lead Doping, Solar RRL 6 (2022). https://doi.org/10.1002/solr.202100730.

[103] Krishna Seshan, Handbook of Thin Film Deposition Techniques, Processes, and Technologies, n.d.

[104] D. Depla, S. Mahieu, J.E. Greene, Sputter deposition processes, n.d.

[105] J.L. Vossen, W. Kern, Thin film processes, Academic Press, 1978.

[106] Alessio Bosio, Daniele Menossi, Greta Rosa, Il_fotovoltaico_di_seconda_generazione_d, (n.d.).

[107] A. Bosio, A. Parisini, A. Lamperti, C. Borelli, L. Fornasini, M. Bosi, I. Cora, Z. Fogarassy, B. Pécz, Z. Zolnai, A. Németh, S. Vantaggio, R. Fornari, n-Type doping of ε-Ga 2 O 3 epilayers by high-temperature tin diffusion, Acta Mater 210 (2021) 84–92. https://doi.org/10.1016/j.actamat.2021.116.

[108] A.G. Milnes, D.L. Feucht, Chapter 1 - Introduction to Semiconductor Heterojunctions, in: A.G. Milnes, D.L. Feucht (Eds.), Heterojunctions and Metal Semiconductor Junctions, Academic Press, 1972: pp. 1–33. https://doi.org/https://doi.org/10.1016/B978-0-12-498050-1.50007-6.

[109] K.L. Chopra, S.R. Das, Thin Film Solar Cells, Springer US, Boston, MA, 1983. https://doi.org/10.1007/978-1-4899-0418-8.

[110] J.E. Moore, S. Dongaonkar, R.V.K. Chavali, M.A. Alam, M.S. Lundstrom, Correlation of Built-In Potential and I–V Crossover in Thin-Film Solar Cells, IEEE J Photovolt 4 (2014) 1138–1148. https://doi.org/10.1109/JPHOTOV.2014.2316364.

[111] D. Menossi, A. Bosio, N. Romeo, Key Developments In CuInGaSe2 Thin Film Solar Cell, LAP Lambert Academic Publishing, 2014.

[112] A. Bosio, N. Romeo, V. Canevari, Chapter 23 - Doped transparent conducting oxides suitable for the fabrication of high efficiency thin film solar cells, in: T. Nakajima, H. Groult (Eds.), Fluorinated Materials for Energy Conversion, Elsevier Science, Amsterdam, 2005: pp. 535–548. https://doi.org/https://doi.org/10.1016/B978-008044472-7/50051-5.

[113] S. Ray, R. Banerjee, N. Basu, A.K. Batabyal, A.K. Barua, Properties of tin doped indium oxide thin films prepared by magnetron sputtering, J Appl Phys 54 (1983) 3497–3501. https://doi.org/10.1063/1.332415.

[114] A. Bosio, G. Rosa, N. Romeo, Past, present and future of the thin film CdTe/CdS solar cells, Solar Energy (2018) 31–43. https://doi.org/10.1016/j.solener.2018.01.018.

[115] D. Menossi, A. Bosio, N. Romeo, Key Developments In CuInGaSe2 Thin Film Solar Cell, LAP Lambert Academic Publishing, 2014.

[116] B.S. Moon, J.H. Lee, H. Jung, Comparative studies of the properties of CdS films deposited on different substrates by R.F. sputtering, Thin Solid Films 511–512 (2006) 299–303. https://doi.org/10.1016/J.TSF.2005.11.080.

[117] A.J.N. Oliveira, J.P. Teixeira, D. Ramos, P.A. Fernandes, P.M.P. Salomé, Exploiting the Optical Limits of Thin-Film Solar Cells: A Review on Light Management Strategies in Cu(In,Ga)Se2, Adv Photonics Res 3 (2022) 2100190. https://doi.org/https://doi.org/10.1002/adpr.202100190.

[118] C.-É. Boukaré, N.B. Cowan, J. Badro, Phase Diagram of the CdS-CdTe Pseudobinary System You may also like Deep Two-phase, Hemispherical Magma Oceans on Lava Planets, n.d.

[119] Q. Cang, H. Guo, X. Jia, H. Ning, C. Ma, J. Zhang, N. Yuan, J. Ding, Enhancement in the efficiency of Sb2Se3 solar cells by adding low lattice mismatch CuSbSe2 hole transport layer, Solar Energy 199 (2020) 19–25. https://doi.org/10.1016/j.solener.2020.02.008.

[120] Mamta, K.K. Maurya, V.N. Singh, Enhancing the Performance of an Sb2Se3-Based Solar Cell by Dual Buffer Layer, Sustainability 13 (2021). https://doi.org/10.3390/su132112320.

[121] N. Romeo, A. Bosio, D. Menossi, C. Catellani, R. Dharmadasa, A. Romeo, High efficiency Cu(In,Ga)Se2/CdS thin film solar cells obtained with precursors sputtered from InSe, GaSe and Cu targets, Thin Solid Films 535 (2013) 88–91. https://doi.org/10.1016/J.TSF.2012.11.060.

[122] N. Romeo, A. Bosio, V. Canevari, The role of CdS preparation method in the performance of CdTe/CdS thin film solar cell, n.d.

[123] S. Ninomiya, S. Adachi, Optical properties of cubic and hexagonal CdSe, J Appl Phys 78 (1995) 4681–4689. https://doi.org/10.1063/1.359815.

[124] N. Romeo, Quasi-Rheotaxy: Growth of large crystalline grain thin films on quasi-liquid substrates, J Cryst Growth 52 (1981) 692–698. https://doi.org/10.1016/0022-0248(81)90364-X.

[125] N. Romeo, S. Cozzi, R. Tedeschi, A. Bosio, V. Canevari, M.A. Tagliente, M. Penza, High quality ZnS:Mn thin films grown by quasi-rheotaxy for electroluminescent devices, Thin Solid Films 348 (1999) 49–55. https://doi.org/10.1016/S0040-6090(99)00009-7.

[126] N. Romeo, V. Canevari, G. Sberveglieri, A. Tosi, A. Camanzi, Quasi-Rheotaxy a new technique to grow large grain thin films on low cost amorphous substrates, Revue de Physique Appliquée 16 (1981) 11–14. https://doi.org/10.1051/rphysap:0198100160101100.

[127] N. Romeo, Quasi-Rheotaxial growth of large crystalline grain thin films on low cost substrates for photovoltaic applications, Progress in Crystal Growth and Characterization 9 (1984) 169–183. https://doi.org/https://doi.org/10.1016/0146-3535(84)90100-X.

[128] Z.U. Borisova, Glassy Semiconductors, Springer US, 1981. https://doi.org/10.1007/978-1-4757-0851-6.

[129] W.C. Tan, M.E. Solmaz, J. Gardner, R. Atkins, C. Madsen, Optical characterization of a-As2S3 thin films prepared by magnetron sputtering, J Appl Phys 107 (2010) 033524. https://doi.org/10.1063/1.3295908.

[130] A.R. Denton, N.W. Ashcroft, Vegard's law, 1991.

[131] L. Vegard, Die Konstitution der Mischkristalle und die Raumfüllung der Atome, Zeitschrift Für Physik 5 (1921) 17–26. https://doi.org/10.1007/BF01349680.

[132] P. Makuła, M. Pacia, W. Macyk, How To Correctly Determine the Band Gap Energy of Modified Semiconductor Photocatalysts Based on UV-Vis Spectra, Journal of Physical Chemistry Letters 9 (2018) 6814–6817. https://doi.org/10.1021/acs.jpclett.8b02892.

[133] M.M. Khan, Semiconductors as photocatalysts: UV light active materials, Theoretical Concepts of Photocatalysis (2023) 33–51. https://doi.org/10.1016/B978-0-323-95191-3.00004-3.

[134] M.H. Dalhat, A. Ahmad, Chapter 19 - Removal of pesticides from water and wastewater by solar-driven photocatalysis, in: M. Shah, S. Rodriguez-Couto, J. Biswas (Eds.), Development in Wastewater Treatment Research and Processes, Elsevier, 2022: pp. 435–458. https://doi.org/https://doi.org/10.1016/B978-0-323-85583-9.00012-0.

[135] P. Vidal-Fuentes, M. Guc, X. Alcobe, T. Jawhari, M. Placidi, A. Pérez-Rodríguez, E. Saucedo, V.I. Roca, Multiwavelength excitation Raman scattering study of Sb $_2$ Se $_3$ compound: fundamental vibrational properties and secondary phases detection, 2d Mater 6 (2019) 045054. https://doi.org/10.1088/2053-1583/ab4029.

[136] V.P. Pham, G.Y. Yeom, Recent Advances in Doping of Molybdenum Disulfide: Industrial Applications and Future Prospects, Advanced Materials 28 (2016) 9024–9059. https://doi.org/https://doi.org/10.1002/adma.201506402.

[137] G. Ghosh, The sb-se (antimony-selenium) system, Journal of Phase Equilibria 14 (1993) 753–763. https://doi.org/10.1007/BF02667889.

[138] N. Spalatu, R. Krautmann, A. Katerski, E. Karber, R. Josepson, J. Hiie, I.O. Acik, M. Krunks, Screening and optimization of processing temperature for Sb2Se3 thin film growth protocol: Interrelation between grain structure, interface intermixing and solar cell performance, Solar Energy Materials and Solar Cells 225 (2021). https://doi.org/10.1016/j.solmat.2021.111045.

[139] R. Krautmann, N. Spalatu, R. Gunder, D. Abou-Ras, T. Unold, S. Schorr, M. Krunks, I. Oja Acik, Analysis of grain orientation and defects in Sb2Se3 solar cells fabricated by close-spaced sublimation, Solar Energy 225 (2021) 494–500. https://doi.org/10.1016/J.SOLENER.2021.07.022.

[140] G.B. Harris, X. Quantitative measurement of preferred orientation in rolled uranium bars, The London, Edinburgh, and Dublin Philosophical Magazine and Journal of Science 43 (1952) 113–123. https://doi.org/10.1080/14786440108520972.

[141] G. Carlo, Fisica dei semiconduttori, Monte Università Parma, 2013.

[142] T. Walter, R. Herberholz,) C Mü Ller, H.W. Schock, Determination of defect distributions from admittance measurements and application to Cu(In,Ga)Se 2 based heterojunctions, 1996. http://jap.aip.org/jap/copyright.jsp.

[143] X. Pan, Y. Pan, L. Shen, L. Wang, R. Wang, G. Weng, J. Jiang, X. Hu, S. Chen, P. Yang, J. Chu, J. Tao, All-Vacuum-Processed $Sb_2(S,Se)_3$ Thin Film Photovoltaic Devices via Controllable Tuning Seed Orientation, Adv Funct Mater 33 (2023). https://doi.org/10.1002/adfm.202214511.

[144] M. Huang, P. Xu, D. Han, J. Tang, S. Chen, Complicated and Unconventional Defect Properties of the Quasi-One-Dimensional Photovoltaic Semiconductor Sb_2Se_3, ACS Appl Mater Interfaces 11 (2019) 15564–15572. https://doi.org/10.1021/acsami.9b01220.

[145] M.T. De Faria, V. Ncio Silva2 De Oliveira1, Microspectroscopy of Some Iron Oxides Raman and Oxyhydroxides, 1997.

[146] D. Bersani, P.P. Lottici, A. Montenero, Micro-Raman Investigation of Iron Oxide Films and Powders Produced by Sol-Gel Syntheses, 1999.

[147] I. Weber, U. Böttger, S.G. Pavlov, H.-W. Hübers, H. Hiesinger, E.K. Jessberger, Laser alteration on iron sulfides under various environmental conditions, (2017). https://doi.org/10.1002/jrs.5083.

[148] C. Avril, V. Erie Malavergne, R. Caracas, B. Zanda, B. Reynard, E. Charon, E. Bobocioiu, F. Brunet, S. Borensztajn, S. Pont, M. Tarrida, F. ßois Guyot, Raman spectroscopic properties and Raman identification of CaS-MgS-MnS-FeS-Cr 2 FeS 4 sulfides in meteorites and reduced sulfur-rich systems, (n.d.). https://doi.org/10.1111/maps.12145.

[149] A. Theodossiou, Measurements of the Hall Effect and Resistivity in Pyrrhotite, Physical Review 137 (1965) A1321–A1326. https://doi.org/10.1103/PhysRev.137.A1321.

[150] D.K. Schroder, Contact Resistance and Schottky Barriers, in: Semiconductor Material and Device Characterization, 2005. https://doi.org/10.1002/0471749095.ch3.

[151] J. Chern, W. Oldham, Determining specific contact resistivity from contact end resistance measurements, 1984. https://doi.org/10.1109/EDL.1984.25875.

[152] M. Ahmad, A.P. Shah, D.K. Sharma, N.R. Roy, B.M. Arora, Determination of semiconductor resistance under a contact, Solid State Electron 46 (2002) 505–512. https://doi.org/10.1016/S0038-1101(01)00286-6.

[153] K. Zeng, D.J. Xue, J. Tang, Antimony selenide thin-film solar cells, Semicond Sci Technol 31 (2016). https://doi.org/10.1088/0268-1242/31/6/063001.

[154] A.L. Dawar, P.K. Shishodia, G. Chauhan, A. Kumar, P.C. Mathur, Growth of high-mobility CdS thin films, J Mater Sci Lett 9 (1990) 547–548. https://doi.org/10.1007/BF00725872.

[155] L.J. van der PAUW, A METHOD OF MEASURING SPECIFIC RESISTIVITY AND HALL EFFECT OF DISCS OF ARBITRARY SHAPE, in: Semiconductor Devices: Pioneering Papers, n.d.: pp. 174–182. https://doi.org/10.1142/9789814503464_0017.

[156] R.H. Bube, Trap Density Determination by Space-Charge-Limited Currents, J Appl Phys 33 (1962) 1733–1737. https://doi.org/10.1063/1.1728818.

[157] V.M. Le Corre, E.A. Duijnstee, O. El Tambouli, J.M. Ball, H.J. Snaith, J. Lim, L.J.A. Koster, Revealing Charge Carrier Mobility and Defect Densities in Metal Halide Perovskites via Space-Charge-Limited Current Measurements, ACS Energy Lett 6 (2021) 1087–1094. https://doi.org/10.1021/acsenergylett.0c02599.

[158] J.A. Röhr, D. Moia, S.A. Haque, T. Kirchartz, J. Nelson, Exploring the validity and limitations of the Mott-Gurney law for charge-carrier mobility determination of semiconducting thin-films, Journal of Physics Condensed Matter 30 (2018). https://doi.org/10.1088/1361-648X/aaabad.

[159] E.A. Duijnstee, J.M. Ball, V.M. Le Corre, L.J.A. Koster, H.J. Snaith, J. Lim, Toward Understanding Space-Charge Limited Current Measurements on Metal Halide Perovskites, ACS Energy Lett (2020) 376–384. https://doi.org/10.1021/acsenergylett.9b02720.

[160] K. Chen, P. Wu, W. Yang, R. Su, D. Luo, X. Yang, Y. Tu, R. Zhu, Q. Gong, Low-dimensional perovskite interlayer for highly efficient lead-free formamidinium tin iodide perovskite solar cells, Nano Energy 49 (2018) 411–418. https://doi.org/10.1016/J.NANOEN.2018.05.006.

[161] G.X. Liang, Y. Di Luo, S. Chen, R. Tang, Z.H. Zheng, X.J. Li, X.S. Liu, Y.K. Liu, Y.F. Li, X.Y. Chen, Z.H. Su, X.H. Zhang, H.L. Ma, P. Fan, Sputtered and selenized Sb2Se3 thin-film solar cells with open-circuit voltage exceeding 500 mV, Nano Energy 73 (2020) 104806. https://doi.org/10.1016/J.NANOEN.2020.104806.

[162] S. Chen, M. Ishaq, W. Xiong, U. Ali Shah, U. Farooq, J. Luo, Z. Zheng, Z. Su, P. Fan, X. Zhang, G. Liang, Improved Open-Circuit Voltage of Sb2Se3 Thin-Film Solar Cells Via Interfacial Sulfur Diffusion-Induced Gradient Bandgap Engineering, Solar RRL 5 (2021). https://doi.org/10.1002/solr.202100419.

[163] S. Sun, S. Zhang, Y. Han, H. Tan, J. Wen, X. Liu, Y. Sun, H. Liu, Improved performances in Sb2Se3 solar cells based on CdS buffered TiO2 electron transport layer, J Solgel Sci Technol (2023). https://doi.org/10.1007/s10971-023-06252-1.

[164] A. Jain, P. Kumar, S.C. Jain, V. Kumar, R. Kaur, R.M. Mehra, Trap filled limit voltage (VTFL) and V2 law in space charge limited currents, J Appl Phys 102 (2007). https://doi.org/10.1063/1.2802553.

[165] M.M. El-Nahass, H.M. Zeyada, M.S. Aziz, M.M. Makhlouf, Current transport mechanisms and photovoltaic properties of tetraphenylporphyrin/n-type silicon heterojunction solar cell, Thin Solid Films 492 (2005) 290–297. https://doi.org/10.1016/j.tsf.2005.06.050.

[166] p-n Junctions, in: Physics of Semiconductor Devices, 2006: pp. 77–133. https://doi.org/https://doi.org/10.1002/9780470068328.ch2.

[167] D. ~R. Green, T. ~E. Michaels, L. ~C. Olsen, L. ~S. Price, Current solar cell measurement methods review and evaluation, (1980) 11469.

[168] K. Ohata, J. Saraie, T. Tanaka, Phase Diagram of the CdS-CdTe Pseudobinary System, Jpn J Appl Phys 12 (1973) 1198–1204. https://doi.org/10.1143/JJAP.12.1198.

[169] X. Fang, T. Zhai, U.K. Gautam, L. Li, L. Wu, Y. Bando, D. Golberg, ZnS nanostructures: From synthesis to applications, Prog Mater Sci 56 (2011) 175–287. https://doi.org/10.1016/j.pmatsci.2010.10.001.

[170] H.C. Chou, A. Rohatgi, N.M. Jokerst, S. Kamra, S.R. Stock, S.L. Lowrie, R.K. Ahrenkiel, D.H. Levi, Approach toward high efficiency CdTe/CdS heterojunction solar cells, Mater Chem Phys 43 (1996) 178–182. https://doi.org/10.1016/0254-0584(95)01626-6.

[171] X. Liu, C. Chen, L. Wang, J. Zhong, M. Luo, J. Chen, D. Xue, D. Li, Y. Zhou, J. Tang, Improving the performance of Sb_2Se_3 thin film solar cells over 4% by controlled addition of oxygen during film deposition, Progress in Photovoltaics: Research and Applications 23 (2015) 1828–1836. https://doi.org/10.1002/pip.2627.

[172] T. Wei, C. Xu, W. Lin, G. Huang, F. Yu, A Lumped-Parameter Equivalent Circuit Modeling for S-Shaped I–V Kinks of Organic Solar Cells, Crystals (Basel) 9 (2019) 80. https://doi.org/10.3390/cryst9020080.

[173] F.J. Garcia-Sanchez, B. Romero, Equivalent Circuit Models for Next Generation Photovoltaic Devices with S-shaped I-V Curves, in: 2019 8th International Symposium on Next Generation Electronics (ISNE), IEEE, 2019: pp. 1–4. https://doi.org/10.1109/ISNE.2019.8896544.

[174] J.E. Moore, S. Dongaonkar, R.V.K. Chavali, M.A. Alam, M.S. Lundstrom, Correlation of Built-In Potential and I–V Crossover in Thin-Film Solar Cells, IEEE J Photovolt 4 (2014) 1138–1148. https://doi.org/10.1109/JPHOTOV.2014.2316364.

[175] B.L. SHARMA, R.K. PUROHIT, Semiconductor Heterojunctions, Elsevier, 1974. https://doi.org/10.1016/C2013-0-10076-1.

[176] A. Mavlonov, T. Nishimura, J. Chantana, Y. Kawano, T. Masuda, T. Minemoto, Back-contact barrier analysis to develop flexible and bifacial Cu(In,Ga)Se_2 solar cells using transparent conductive In_2O_3: SnO_2 thin films, Solar Energy 211 (2020) 1311–1317. https://doi.org/10.1016/j.solener.2020.10.077.

[177] K. Wang, O. Gunawan, T. Todorov, B. Shin, S.J. Chey, N.A. Bojarczuk, D. Mitzi, S. Guha, Thermally evaporated Cu_2ZnSnS_4 solar cells, Appl Phys Lett 97 (2010) 143508. https://doi.org/10.1063/1.3499284.

[178] O. Gunawan, T.K. Todorov, D.B. Mitzi, Loss mechanisms in hydrazine-processed Cu2ZnSn(Se,S)4 solar cells, Appl Phys Lett 97 (2010) 233506. https://doi.org/10.1063/1.3522884.

[179] M. Gloeckler, C.R. Jenkins, J.R. Sites, Explanation of Light/Dark Superposition Failure in CIGS Solar Cells, MRS Online Proceedings Library 763 (2002) 522. https://doi.org/10.1557/PROC-763-B5.20.

[180] C.-H. Chung, B. Bob, T.-B. Song, Y. Yang, Current–voltage characteristics of fully solution processed high performance CuIn(S,Se)2 solar cells: Crossover and red kink, Solar Energy Materials and Solar Cells 120 (2014) 642–646. https://doi.org/https://doi.org/10.1016/j.solmat.2013.10.013.

[181] Thomas Dittrich, Basic Characteristics and Characterization of Solar Cells, in: Materials Concepts for Solar Cells, WORLD SCIENTIFIC (EUROPE), 2018: pp. 3–43. https://doi.org/10.1142/9781786344496_0001.

[182] T. Ott, F. Schönberger, T. Walter, D. Hariskos, O. Kiowski, O. Salomon, R. Schäffler, Verification of phototransistor model for Cu(In,Ga)Se2solar cells, in: Thin Solid Films, Elsevier B.V., 2015: pp. 392–396. https://doi.org/10.1016/j.tsf.2014.09.025.

[183] A. Kumar, P. Ranjan, Defects signature in VOC characterization of thin-film solar cells, Solar Energy 220 (2021) 35–42. https://doi.org/10.1016/j.solener.2021.03.017.

LIST OF PAPERS PUBLISHED IN INTERNATIONAL JOURNALS

1. Pasini, S., Spoltore, D., Parisini, A., Marchionna, S., Fornasini, L., Bersani, D., Fornari, R., & Bosio, A. (2023). Innovative back-contact for Sb2Se3 -based thin film solar cells. *Solar Energy*, *249*, 414–423. https://doi.org/10.1016/j.solener.2022.11.049

2. Pasini, S., Spoltore, D., Parisini, A., Foti, G., Marchionna, S., Vantaggio, S., Fornari, R., & Bosio, A. (2023). Sb2Se3 Polycrystalline Thin Films Grown on Different Window Layers. Coatings, 13(2). https://doi.org/10.3390/coatings13020338

3. Bosio, A., Pasini, S., & Romeo, N. (2020). The history of photovoltaics with emphasis on CdTe solar cells and modules. *Coatings*, *10*(4). https://doi.org/10.3390/coatings10040344

4. A. Bosio, G. Foti, S. Pasini, D. Spoltore, A Review on the Fundamental Properties of Sb2Se3-Based Thin Film Solar Cells, Energies (Basel) 16 (2023) 6862. https://doi.org/10.3390/en16196862.

5. Stefano Pasini et al., "Innovative and sustainable solar cells based on abundant elements on the Earth crust", in Lecture Notes joint EPS-SIF International School on Energy, Course 7 "Global Challenges for Energy Sustainability", edited by L. Cifarelli, F. Romanelli (SIF, 2024).

6. S. Pasini, D. Spoltore, G. Foti, A. Parisini, M. Pavesi, S. Shapouri, I. Cora, Z. Fogarassy, R. Fornari, A. Bosio. Effect of heterojunction characteristics and deep electronic levels on the performance of (Cd,Zn)S/Sb2Se3 solar cell. Under review.

LIST OF CONFERENCE AND SUMMER SCHOOL ATTENDANCES

1. XLIX Meeting of the Italian Association of Crystallography, 6-9 September 2021, Parma.
2. Emerging Inorganic Materials in Thin-Film Photovoltaics Conference, Royal Society of Chemistry, 4-6 July 2022, Bath, UK and Online.
3. 3rd European School on Crystal Growth, 20-23 July 2022, Paris, Fr.
4. 8th World Conference on Photovoltaic Energy Conversion (WCPEC-8), 26-30 September 2022, Milano, Italy.
5. joint EPS-SIF International School on Energy, Course 7 "Global Challenges for Energy Sustainability", 17-22 July 2023, Varenna, Italy.
6. Seconda Conferenza Rete Italiana del Fotovoltaico, 11-12 June 2024, Bolzano, Italy.
7. 14th European Kesterite and ReNew-PV Workshop, 26-28 June 2024, Verona, Italy.